Martin Fonnum Jakobsen

Transport in Magnetic and Superconducting Heterostructures

NTNU
Norwegian University of
Science and Technology

Martin Fonnum Jakobsen

Transport in Magnetic and Superconducting Heterostructures

Thesis for the Degree of Philosophiae Doctor

Trondheim, November 2021

Norwegian University of Science and Technology
Faculty of Natural Sciences
Department of Physics

NTNU
Norwegian University of
Science and Technology

Abstract

In essence, spintronics aims to utilize the spins of electrons to store and process information, either as a supplement to or as a replacement for electron charges. Electron spins are particularly suitable for use in information technology because they are binary in nature. Some spintronics applications are already commercially available and have led to a revolution in magnetic storage technology, for instance, with the invention of the hard disk drive. Several other spintronics applications are either close to commercialization or still in the idea phase. An ambitious long-term goal of spintronics research is to trigger a revolution in low-power information and communication technologies to facilitate a more energy-efficient society.

The research in this thesis concerns two spintronic subfields: spin insulatronics and superconducting spintronics. In spin insulatronics, information is sent through magnetic insulators via spin waves. Information is sent without accompanying charge transport and thereby has the potential to significantly reduce Joule heating, the major source of energy waste in conventional electronics. Junctions consisting of superconducting and magnetic materials are of significant importance in superconducting spintronics. Close to the interfaces of such junctions, the superconductor and magnet influence each other, which can lead to the emergence of new physical phenomena. In these superconducting heterostructures, the electron spin, charge, and superconducting phase coherence can work together to increase the energy efficiency, performance, and durability of novel state-of-the-art technologies.

This thesis represents my humble contribution to spintronics and perhaps provides a modest step towards a better understanding of spin and superconducting transport via magnetic materials. Three [1–3] research papers form the backbone of this thesis and investigate different aspects of spin insulatronics and superconducting spintronics. Concretely, [1] elucidates the role of disorder on spin-wave transport, while [2] and [3] investigate local and nonlocal transport in antiferromagnet-superconductor junctions. The main text in this thesis introduces the necessary physics for understanding the papers and attempts to set the research in a scientific perspective.

List of publications

Paper [1]

"Scattering theory of transport through disordered magnets"
Martin F. Jakobsen, Alireza Qaiumzadeh, and Arne Brataas
Physical Review B **100**, 134431 (2019)

Paper [2]

"Electrical and thermal transport in antiferromagnet-superconductor junctions"
Martin F. Jakobsen, Kristian B. Naess, Paramita Dutta, Arne Brataas, and Alireza Qaiumzadeh
Physical Review B **102**, 140504(R) (2020)

Paper [3]

"Electrically controlled crossed Andreev reflection in two-dimensional antiferromagnets"
Martin F. Jakobsen, Arne Brataas, and Alireza Qaiumzadeh
Physical Review Letters **127**, 017701 (2021)

My contributions to the publications

I am the first author of all publications [1–3] in this thesis. My contributions include performing all analytical and numerical calculations, creating all figures, and writing most of the manuscripts. In the third paper, I also conceived the underlying idea of the project. My coauthors provided useful feedback on the manuscripts and participated in numerous discussions.

Preface

This thesis is submitted to the Norwegian University of Science and Technology (NTNU) as a partial fulfillment of the requirements for the degree of Philosophiae Doctor. The research was performed at the Department of Physics from August 2017 until November 2021. The candidate supervisor and cosupervisor were Professor Arne Brataas and Professor John Ove Fjærestad, respectively. Senior researcher Dr. Alireza Qaiumzadeh was an important collaborator. The candidate was funded by The Research Council of Norway through its Centres of Excellence funding scheme Project No. 262633 "QuSpin", the European Research Council via Advanced Grant No. 669442 "Insulatronics", and NTNU through RSO 8177 1073.

In addition to the thesis, the graduate program includes 30 European Credit Transfer and Accumulation System (ECTS) credits of coursework and a 1.25-year extension under obligation of teaching duties at the Department of Physics. The candidate was the lecturer in "TFY4165-Thermodynamics" and made the final exams for two semesters. The candidate was also a lab assistant in "TFY4104-Physics" and "FY1003-Electricity and magnetism".

<div align="right">

Martin F. Jakobsen
Trondheim, Norway
August 2021

</div>

Acknowledgments

First, I would like to thank my supervisor, Arne Brataas. Thank you for providing me with some of your valuable time, guidance, and insight. Your broad overview and genuine interest in fundamental physics is impressive and acts as an invaluable source of ambitious research projects.

I am also grateful to Alireza Qaiumzadeh, who has been a coauthor on all my research papers and acted as an additional mentor figure. One of the best parts of my PhD has been our collaborations, meetings, and unrelenting physics discussions. Thank you for your continuous encouragement, patience, and genuine friendliness. I am also grateful and want to thank the additional coauthors on my second paper, Paramita Dutta and Kristian Naess.

I am thankful to Jon Andreas Støvneng for trusting me with teaching "TFY4165–Thermodynamics" and our conversations about pedagogical and nonpedagogical matters. I also thank the students in MTFYMA, BFY, and LUR for being pleasant, easy going, and eager to learn about the Carnot engine. Lecturing for you has been one of the personal highlights of my PhD.

I have also had the great pleasure of sharing an office with Haakon, Øyvind, and Therese. Their optimism, drive, and friendly nature remain unparalleled. I feel incredibly lucky and thankful to have shared this time with you and will miss our (frequent) breaks whenever anyone needed motivation. In addition, I have had the pleasure of meeting new friends and colleagues in the majority of QuSpin's members. There are simply too many down to earth and genuinely positive people to list every meaningful interaction while simultaneously keeping this thesis concise. I would like to thank all of you for always contributing positively to my years at our small research center on the 5th floor of Realfagbygget.

In addition, I want to express my gratitude to the people whose collective efforts have had an important positive impact on forming my interest in mathematics, physics, and general science. Some of those people are: Inger Norunn Nergaard, Michael Wakeford, Elisaveta Malamova, Jens O. Andersen, Tomáš Brauner, and Frode Fonnum.

Furthermore, I highly appreciate my friends outside of QuSpin, both those who live in Trondheim and those who live elsewhere. Thank you for being a part of my life, contributing to fun spare-time activities, and helping me focus on life outside of physics.

I highly value and appreciate my family for their unwavering moral support, encouragement, and belief in me. I'm particularly thankful for my sister (Katrine), parents (Bjørnar & Jannicke), grandaunt (Turid) and grandparents (Frode & Marit and Per & Sol), who regularly called me to chat and check in during my PhD. I also acknowledge and thank the little rascals Birger & Birgitte for being avid providers of optimism and somewhat dubious food. Last, but certainly not least, I thank Stine for providing me with companionship, love, and support.

Contents

1

Introduction

1.1 Electronics - fundamental limitations

Information and communication technology has become one of the cornerstones of modern society. In most modern households, businesses, and industries, we are surrounded by technology powered either entirely or mainly by electronics. An essential building block in modern technologies is semiconductor-based integrated circuits. In a simplistic sense, an integrated circuit is a large number of electronic components, such as resistors, diodes, transistors, and capacitors, stacked together on a single chip. The first integrated circuit was made in 1958, and its development was awarded the Nobel prize in 2000 [4]. The usefulness of the integrated circuit lies in that it can be programmed to act as a broad spectrum of different devices such as microprocessors, oscillators, amplifiers, or random access memory (RAM). It is not an understatement to say that the integrated circuit is the heart and brain of modern electronic technology.

The processing and temporary storage of information in integrated circuits utilizes only the electric charge of the electrons. The information is encoded in a binary system of 0 or 1 bits. Typically, the low-current state and high-current state represent 0 and 1 bits, respectively. To store a single bit, one memory cell is

required, which means that a large number of memory cells are needed to meet our technological demands. As a concrete example, consider a dynamic random access memory (DRAM) cell consisting of a transistor and capacitor. Consider the storage of the letter "A". In ASCII, "A" can be written as 01000001. Consequently, 8 bits (or 1 byte) is required to store "A", which means that 8 DRAM cells, in total containing 8 transistors and 8 capacitors, must be embedded on the integrated circuit. To store more complicated and useful information, the number of elements that need to be included in the integrated circuit increases exponentially. This is encapsulated in Moore's law, which states that the number of transistors embedded on an integrated circuit doubles every two years [5, 6]. An increase in transistor density typically results in improvement in other aspects of technology, such as computer processing speed. In essence, Moore's law is an empirical observation and is used as a guiding reference for technological development in the industry. Rather surprisingly, Moore's law has been accurate to date, and transistor counts as high as 10^{10} in CPUs have been recorded [7]. Continuing to increase the number of transistors on sufficiently small chips requires the transistor size to eventually reach the atomic scale, where quantum effects dominate. At the atomic scale, conventional electronics, which are based on classical physics, would no longer function as intended, facilitating the need for an alternative.

In addition, since conventional electronics rely on the transport of electron charges through systems of finite resistance, the heat loss known as Joule heating is unavoidable. Joule heating represents a portion of the input energy that is lost to the environment without producing any useful output. In blunt terms, it is an unavoidable waste of energy in electronics-based technology. Joule heating is also incompatible with the sought after miniaturization of technology. When a large number of technological components are stacked on a chip, Joule heating creates a significant local temperature increase, resulting in the corresponding technology malfunctioning. The increasing importance of obtaining an energy-efficient, clean, and sustainable society makes it worthwhile to pursue technologies fundamentally different from electronics. One possible candidate for such a technology is spintronics.

1.2   Spintronics - new spin on modern technology

Most of the inherent problems of electronics stem from the fact that information is only transported or stored by moving electron charges through regions of finite

resistance. The fundamental idea behind spintronics [8, 9] is to also utilize the intrinsic electron spin. Each electron spin produces a tiny magnetic field, similar to a bar magnet, and is responsible for the magnetic properties of a material. In contrast to electric charge, electron spin is a pure quantum property with no classical counterpart. The electron spin is binary in the sense that its direction can only be parallel (spin up) or antiparallel (spin down) to the direction of measurement specified by, e.g., a magnetic field. The binary and quantum nature of the electron spin makes it compatible with use in high-density information technology, where information is transported and stored using 0 and 1 bits over continuously decreasing length scales.

Perhaps the most prominent commercial application of spintronics is the modern hard disk drive (HDD). The original HDD design is based on an effect known as giant magnetoresistance (GMR) [10, 11], and its discovery was awarded the Nobel prize in 2007. The Nobel committee justified the prize by saying that "*This year's physics prize is awarded for the technology that is used to read data on hard disks. It is thanks to this technology that it has been possible to miniaturize hard disks so radically in recent years. Sensitive read-out heads are needed to be able to read data from the compact hard disks used in laptops and some music players, for instance.*" [12]. The development and commercialisation of HDDs also resulted in a tremendous increase in disk storage density [13]. The experimental GMR design is illustrated in Fig. 1.1. A nonmagnetic conductor is sandwiched between two
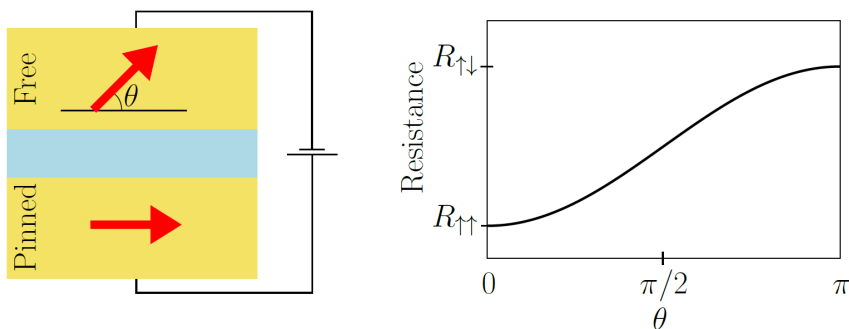
Figure 1.1. A conductor (GMR) or insulator (TMR) is sandwiched between two magnets, and a bias voltage is applied to the junction. One of the magnetizations is pinned [14], and the other is free to rotate. The angle of misalignment between the magnetizations is denoted by θ. The total junction resistance depends on the angle of misalignment and takes its minimum value $R_{\uparrow\uparrow}$ when $\theta = 0$ and its maximum value $R_{\uparrow\downarrow}$ when $\theta = \pi$.

metallic magnets, and a voltage bias induces a current. If the magnetic fields of
the magnets are parallel or antiparallel, the junction exhibits a low-resistance (0)
or high-resistance (1) state, respectively. Quantitatively, this is encapsulated by
the magnetoresistance ratio (MRR), which is the percentage difference between the
resistances of the parallel and antiparallel configurations. A read head with a large
MRR is desirable because it enables higher storage density. Despite that it was the
discovery of GMR that commercialized spintronics; another effect with larger MRRs
has taken over its technological applications. The effect in question is called tunnel
magnetoresistance (TMR) [15]. The experimental design is identical except that the
conductor is replaced by a sufficiently thin insulator so that an electric current can
still pass through via quantum tunneling. Continuous experimental development of
TMR has enabled MRRs as large as 10^2–10^6% [16–20].

Another promising application of GMR or TMR is magnetic random access
memory (MRAM). It is advantageous over transistor-based RAM in the sense that
it is nonvolatile; MRAM does not require a continuous power supply to store infor-
mation and exhibits near zero leakage power. In contrast to flash memory, MRAM
can be written to without applying voltage pulses that degrade its writing capabili-
ties. This leads to MRAM exhibiting faster operation times, lower power consump-
tion, and, in principle, indefinite lifetimes. In MRAM, the information is stored via
small magnetic elements whose magnetic fields are either parallel or antiparallel to
a reference magnetic field used to read the memory by GMR or TMR; see Fig. 1.2.
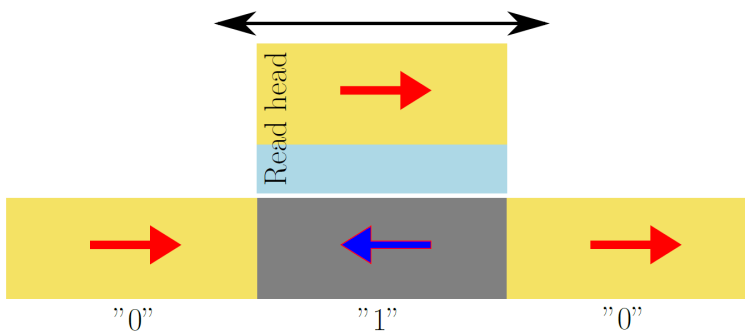In its early development phase, one of the main disadvantages of MRAM was that

Figure 1.2. A simplified sketch of the MRAM read out principle. A movable
read head detects whether the magnetization of a given magnetic element is parallel
or antiparallel to the intrinsic reference magnetization by measuring the resistance
through GMR or TMR. A low- or high-resistance state is interpreted as a 0 or 1 bit,
respectively.

it required large amounts of power, making it unfeasible in low-power applications. This problem has been greatly reduced by utilizing spin transfer torques (STTs) [21, 22] to create so-called STT-MRAM [23, 24]. Currently, several companies have manufactured commercially available STT-MRAM technologies varying from 256 MB to 1 GB [25–28].

A closely related spintronics memory technology is racetrack memory (RTM) [29–31]. The setup is similar to that of MRAM, except that the magnetic elements are moving, like cars on a racetrack, and detected by a stationary read head. The motion of the magnetic elements is controlled by applying a current, as shown in Fig. 1.3. RTM combines the endurance of magnetic HDDs, the high density of flash, and
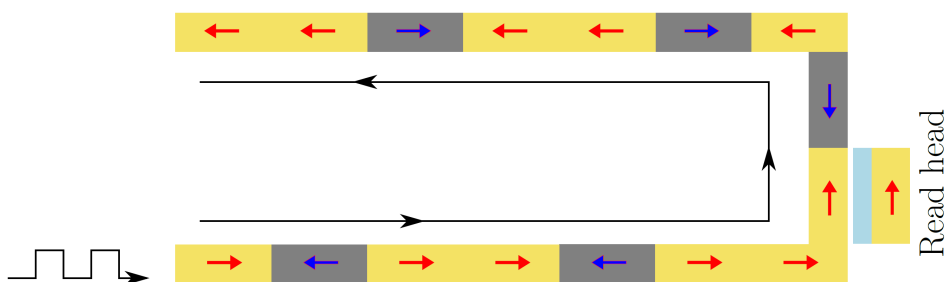
Figure 1.3. A simplified sketch of the RTM read out principle. The magnetic elements, more specifically the domain walls, embedded on the U-shape can be moved by applying a current. A stationary read head with a reference magnetization is used to detect the relative magnetization orientations of the magnetic elements using GMR or TMR. A U-shape is convenient because it enables high packing density, but a linear shape is also possible.

the high latency rates of static random access memory (SRAM) and DRAM. In Tab. 1.1, we compare different memory technologies with respect to various parameters, such as size, power leakage, retention cycles, and write endurance.

Table 1.1. Comparison of electronics and spintronics memory technologies [32–37].

	Electronics			Spintronics		
	SRAM	**DRAM**	**V-NAND**	**HDD**	**STT-MRAM**	**RTM**
Cell size (F^2)	$120 - 200$	$4 - 8$	$1 - 5$	0.5	$6 - 50$	≤ 2
Write endurance (P/E cycles)	10^{16}	10^{16}	$10^3 - 10^5$	10^6	10^{12}	10^{16}
Read time (ns)	$1 - 100$	30	10^3	10^6	$3 - 15$	$3 - 250$
Write/Erase time (ns)	$1 - 100$	50	$10^5 - 10^6$	10^6	$3 - 15$	$3 - 250$
Read energy	low	medium	medium	medium	low	low
Write energy	low	medium	high	medium	high	low
Leakage power	high	medium	low	low	low	low
Retention period	power supply	$64 - 512$ ms	years	years	years	years

A spintronics technology, currently in development, is the spin field-effect transistor [38]. The conventional electronic transistor functions as a switch and can be used to represent bits in memory applications or to control logic operations in processors. The electron spin is permanent and can be detected without applying electrical currents. Consequently, the spin field-effect transistor may present a more sensitive, scalable, and nonvolatile alternative to the conventional transistor. To the best of our knowledge, there are experimental realizations of the spin field-effect transistor [39–41], but it has not yet reached the stage of commercial development.

The previous examples illustrate that spintronics is a viable candidate as a potential successor or complementary technology to electronics. However, all of the aforementioned spintronics applications involve charge transport in some capacity. Therefore, the Joule heating problem remains unsolved in today's commercially available technology. However, spintronics has already provided technologies previously thought impossible, and there is still significant untapped potential [42]. For spintronics to commercially outperform electronics, a balance between technological performance, consumer demand, and market supply must be struck. Nevertheless, the future of spintronics looks exciting not only with respect to commercial applications but also from the viewpoint of fundamental physics.

1.3   Spintronics - magnets and superconductors

As hopefully is apparent, spintronics is a field with significant variety and various directions, making it impossible to concisely cover all aspects. The research performed in this thesis focuses on two spintronic subfields: spin insulatronics and superconducting spintronics. Here, we briefly introduce both subfields but emphasize that there are many more.

One possibility for eliminating Joule heating is by eliminating the charge degree of freedom altogether as an information carrier. This is the subject of spin insulatronics [43] where magnetic conductors are replaced by magnetic insulators. In a magnetic insulator, charges cannot propagate; therefore, any charge transport and accompanying Joule heating are suppressed. However, since magnetic insulators contain coupled localized spins, information can still be transferred through the material in fundamentally new ways. In a magnetic insulator, the spins are coupled so that a disturbance of one spin leads to a perturbation that propagates through the insulator. This wave-like perturbation is referred to as a spin wave. Experimentally, it has been shown that spin waves can be both excited and detected [44–51] as well

as propagate on the micrometer scale [52–54] with characteristic frequencies from GHz to THz [55]. Devices based on spin insulatronics can often be controlled by using an external magnetic field to change the magnetic configuration. Consequently, it is possible to use spin excitations to perform logic operations that are critical in information technology. Examples include spin-wave transistors [56] and majority gates [57].

The fusion of spintronics with superconductivity, known as superconducting spintronics [58, 59], is considered a promising candidate for enabling high-density and low-dissipation information technology. By placing a superconductor in contact with a (magnetic) material, we obtain an interface that inherits properties from both materials, which is known as the proximity effect [60–64]. The proximity effect enables the design of structures in which spin, charge, and superconducting phase coherence work together to produce a whole new spectrum of technological and experimental applications. Particularly famous commercial applications include the superconducting quantum interference device (SQUID). At the time of writing, SQUIDs are the most sensitive detectors of magnetic flux. In essence, a SQUID operates as a flux-to-voltage transducer and can detect fields much lower than the fundamental magnetic flux $\Phi_0 = h/2e \approx 2 \cdot 10^{-15}$ Wb. SQUIDs are also incredibly versatile, as they can be used to measure any physical quantity that can be converted to a flux. Consequently, SQUID applications are plentiful. Concrete SQUID applications include but are not limited to the detection of tiny magnetic fields in the human brain, MRI in the microtesla range, oil and mineral exploration, and detection of gravity waves [65–67]. Recently, the role of superconductivity in quantum computers has gained momentum in media through several tech giants that are currently pursuing quantum supremacy by using superconducting quantum bits [68–71].

While applications are certainly useful and important to our society, the research conducted in this thesis has primarily been driven by personal curiosity and the desire to make a small contribution to science. Specifically, the research consists of three research papers. In paper [1], we consider the effects of disorder on spin-wave transport through magnetic insulators. In papers [2] and [3], we consider the interplay between magnetism and superconductivity to control local and nonlocal electrical signals. Structurally, this thesis is written such that Chapters 2 and 3 introduce the basic theory of magnetism and superconductivity. Chapter 4 introduces the general framework for combining and studying the transport properties of magnetic and superconducting hybrid structures. Chapters 5, 6, and 7 briefly dis-

cuss research highlights from papers [1], [2], and [3]. Finally, Chapter 8 concludes, reflects on, and summarizes the journey.

2

Magnetism and spin waves

Every substance is made up of atoms. Each atom contains electrons that, for our purposes, have three important intrinsic properties: mass, electrical charge, and spin. Spin is a quantum mechanical property that makes electrons behave like tiny magnetic dipole moments, effectively producing magnetic fields. In nonmagnetic (diamagnetic) atoms, the electrons are grouped into pairs of opposite spins according to the Pauli principle, such that their net magnetic dipole moment is zero. Atoms with unpaired electrons have a finite magnetic dipole moment, as shown in Fig. 2.1. In a magnetic material, the interactions between its magnetic dipole moments
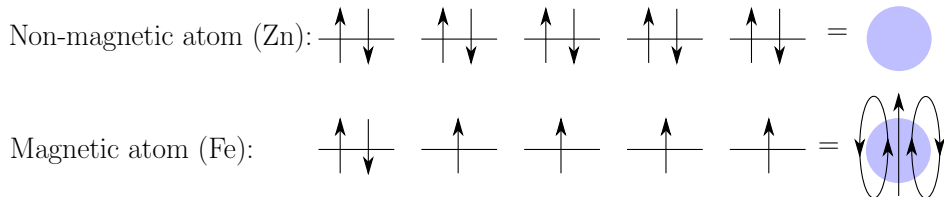

Figure 2.1. Electronic filling of the $3d$-orbitals of a nonmagnetic atom (Zn) and a magnetic (Fe) atom. The four unpaired electrons in iron result in the atom having a total spin-angular momentum of $S = 2\hbar$ and consequently producing a magnetic field.

determine the type of magnetism that occurs. There are several different types of magnetism. Some examples are paramagnetism, ferromagnetism, ferrimagnetism, and antiferromagnetism. Our research has primarily focused on ferromagnetism and antiferromagnetism, which is what we focus on in the following.

Before we proceed, we make a distinction between magnetic insulators and magnetic metals. In a magnetic insulator, the electrons are localized close to their parent atom, and no electricity can flow through the system. On the other hand, a magnetic metal consists of both localized and itinerant electrons that can carry electricity. Whether a magnetic material is insulating or metallic depends on the position of the Fermi energy. If the Fermi energy is outside (inside) a gap in the band structure, the material is metallic (insulating). For simplicity, in the following, we focus on magnetic insulators.

2.1   Magnetic ordering

In ferromagnets and antiferromagnets, the localized magnetic dipole moments inside the same domain are aligned either parallel or antiparallel, respectively, as shown in Fig. 2.2. Consequently, ferromagnets produce large external fields, while antiferro-
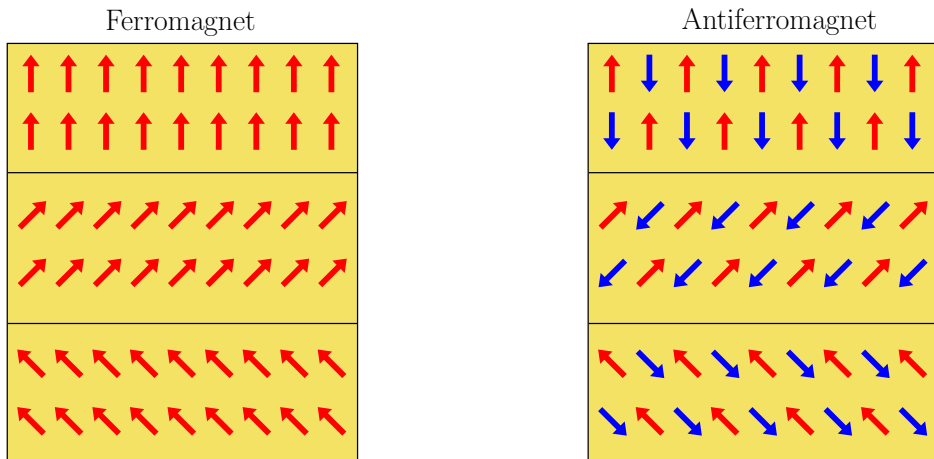

Figure 2.2. Within a magnetic domain, the localized magnetic dipole moments are parallel and antiparallel in ferromagnets and antiferromagnets, respectively.

magnets produce zero or small external fields. Since magnetic fields couple with each other, there are both advantages and disadvantages in spintronics applications. On

the one hand, ferromagnetic spintronics applications are easily controllable through the application of external fields. However, in high-density applications, the intrinsic magnetic field produced by ferromagnets can easily disturb surrounding components or couple to unwanted stray fields. By instead utilizing antiferromagnets, we can avoid both of the aforementioned problems since they produce negligible fields. In addition, antiferromagnetic insulators typically exhibit spin dynamics on the GHz-THz scale [72, 73], making them potentially faster than ferromagnets, which typically operate on the GHz scale. However, the lack of magnetic field production is also the Achilles heel of antiferromagnet-based spintronics because it makes antiferromagnets harder to control. That being said, it is hard to say whether the previous statement will stand the test of time given that controlling antiferromagnetic spintronics devices, e.g., through electrical switching, is certainly not impossible and is currently a rapidly paced and active field of research [73–77].

On a fundamental level, ferromagnetic or antiferromagnetic ordering occurs due to the exchange interaction between two magnetic dipole moments [78, 79]. The exchange interaction is usually short ranged, and a typical approximation accounts only for coupling between nearest neighbor (n.n.) or next-nearest neighbor (n.n.n) atoms. In a simple picture, the exchange interaction between electron spins arises from the interplay of the Coulomb interaction and the Pauli principle [80]. The value of the exchange interaction between two spins is determined by the overlap of the two corresponding electron wavefunctions. Each wavefunction usually decays exponentially for large distances, which leads to short-range behaviour. More rigorously, the exchange interaction can be derived from the Hubbard model [81–83].

At finite temperatures, the exchange interaction competes with thermal fluctuations. If the thermal fluctuations dominate, the magnetic dipole moments point in random directions, and the system exhibits paramagnetic behaviour. The magnetic phase is therefore temperature dependent. Generically, a magnetic material exhibits ferromagnetic (antiferromagnetic) behaviour if its temperature is below the Curie temperature (Néel temperature). At higher temperatures, the system exhibits paramagnetic behaviour. The paramagnetic phase is characterized by Curie's law.

Physically, we often model magnetic materials as a system of spins embedded on a lattice. In its simplest form, the lattice sites are labelled by i and have a spin operator $\mathbf{S}_i$ associated with them. The simplest description of a ferromagnet or antiferromagnet is encapsulated by the isotropic Heisenberg Hamiltonian

$$H = -\sum_{ij} J_{ij}\mathbf{S}_i \cdot \mathbf{S}_j, \tag{2.1}$$

where J_{ij} is the exchange interaction between the spins $\mathbf{S}_i$ and $\mathbf{S}_j$. For simplicity, in the following, we assume that the exchange interaction couples only the nearest neighbor (n.n.) spins and that its strength is position independent

$$J_{ij} = \begin{cases} J, & i \text{ and } j \text{ n.n.}, \\ 0, & \text{otherwise.} \end{cases} \tag{2.2}$$

Next, we demonstrate that in the quantum mechanical description, the system exhibits ferromagnetism if $J > 0$ and antiferromagnetism if $J < 0$. The quantum mechanical relationship between the sign of the exchange interaction and the type of magnetic ordering is in agreement with the classical picture.

2.2   Holstein-Primakoff transformation

The spin operators in Eq. (2.1) are quite complicated objects that satisfy both commutation relations

$$\left[S_i^\alpha, S_j^\beta \right] = i\hbar \delta_{ij} \sum_\gamma \epsilon_{\alpha\beta\gamma} S_i^\gamma, \tag{2.3}$$

and the coupled nonlinear differential equations of the form

$$\frac{\mathrm{d}}{\mathrm{d}t} \mathbf{S}_j = \frac{i}{\hbar} [H, \mathbf{S}_j] = -\mathbf{S}_j \times \mathcal{H}_j. \tag{2.4}$$

The Latin and Greek indices denote the site number and the (x, y, z)-components of the spin operator, respectively. Here, we utilize both the Kronecker delta δ_{ij} and the Levi-Civita symbol $\epsilon_{\alpha\beta\gamma}$. In the classical picture, the nonlinear differential equations describe spins precessing around an effective magnetic field denoted by $\mathcal{H}_j = \delta H / \delta \mathbf{S}_j$. In the following, we set Planck's reduced constant to unity; $\hbar = 1$.

To understand the ordering of magnetic systems in a quantum mechanical picture, it is often useful to utilize spin-wave theory. In general, spin-wave theory is an expansion in terms of excitations close to the classical ground state. To study excitations, it is useful to map the complicated spin operators to simpler boson operators. The choice of the mapping depends on whether we want to study weak or strong deviations from the classical ground state. Our research focuses on weak deviations from the ground state, and hence, we choose the Holstein-Primakoff representation [84].

For a general spin system, each spin operator can be decomposed into longitudinal and transverse components. The longitudinal direction coincides with the classical ordering of the spins, and the transverse components represent deviations.

Mathematically, we write

$$\mathbf{S}_i = \hat{e}_z(i)S_i^z + \hat{e}_x(i)S_i^x + \hat{e}_y(i)S_i^y, \tag{2.5}$$

where $\hat{e}_z(i)$ and $\{\hat{e}_x(i), \hat{e}_y(i)\}$ are site-dependent unit vectors describing the longitudinal and transverse directions, respectively. In the Holstein-Primakoff (HP) representation, we write

$$
\begin{aligned}
S_i^z &= S - n_i, \\
S_i^+ &= S_i^x + iS_i^y = \sqrt{2S}\sqrt{1 - \frac{n_i}{2S}}\,b_i, \\
S_i^- &= S_i^x - iS_i^y = \sqrt{2S}\,b_i^\dagger\sqrt{1 - \frac{n_i}{2S}}.
\end{aligned}
\tag{2.6}
$$

Here, S is the dimensionless spin number, $S_i^\pm$ are spin raising and lowering operators, $b_i^{(\dagger)}$ is a bosonic annihilation (creation) operator on lattice site i, and $n_i = b_i^\dagger b_i$ is the corresponding number operator. Since the allowed eigenvalues of S_i^z are $-S, -S+1, \ldots, S$, the boson number must satisfy the constraint $\langle n_i \rangle / 2S \leq 1$. The HP representation satisfies the spin commutation relations $\left[S_i^\alpha, S_j^\beta\right] = i\delta_{ij}\sum_\gamma \epsilon_{\alpha\beta\gamma}S^\gamma$ if $b_i^{(\dagger)}$ satisfies the bosonic commutation relations where $\left[b_i, b_j^\dagger\right] = \delta_{ij}$ and all other commutators are zero. The quasiparticle excitations associated with the bosonic $b_i^{(\dagger)}$ operators are called magnons.

The square roots in Eq. (2.6) should be interpreted as a series expansion. The HP representation is most useful if the parameter $\langle n_i \rangle / 2S$ is small. In this case, we can perform the low-order expansion

$$
\begin{aligned}
S_i^+ &\approx \sqrt{2S}\left(b_i - \frac{n_i b_i}{4S} + \ldots\right), \\
S_i^- &\approx \sqrt{2S}\left(b_i^\dagger - \frac{b_i^\dagger n_i}{4S} + \ldots\right),
\end{aligned}
\tag{2.7}
$$

which allows us to perturbatively study the spin-wave excitations and interactions of Eq. (2.1). To determine the magnetic ordering and to study the low-order excitations of a system, it is usually sufficient to keep only the lowest-order terms in Eq. (2.7). Higher-order terms are interpreted as magnon interactions.

2.3 Ferromagnets

The simplest ferromagnetic insulator with isotropic nearest neighbor exchange couplings is modeled by the Hamiltonian

$$H = -J\sum_{\langle ij \rangle} \mathbf{S}_i \cdot \mathbf{S}_j, \tag{2.8}$$

with $J > 0$. The angular brackets $\langle\cdot\rangle$ denote summation over only nearest neighbors, and we assume that the spins are embedded on a d-dimensional hypercubic lattice with unit lattice spacing. We assume periodic boundary conditions in all directions and that in total, there are N sites. To determine the quantum mechanical ground state, we rewrite the Hamiltonian as

$$H = -J \sum_{i\boldsymbol{\delta}} \left[\frac{1}{2} \left(S_i^+ S_{i+\boldsymbol{\delta}}^- + S_i^- S_{i+\boldsymbol{\delta}}^+ \right) + S_i^z S_{i+\boldsymbol{\delta}}^z \right]. \tag{2.9}$$

Here, $\boldsymbol{\delta}$ is a vector used to sum over all the nearest neighbors of lattice site i. As a trial ground state, we use the state with maximal spin projection at each site,

$$|\text{FM}\rangle = |\uparrow, \uparrow, \ldots, \uparrow\rangle = |\uparrow\rangle_1 \otimes |\uparrow\rangle_2 \otimes \ldots |\uparrow\rangle_N. \tag{2.10}$$

All the spins are pointing in the same direction, similar to a classical ferromagnet. Here, we introduce the short-hand notation

$$|\uparrow\rangle_i = |S, S_i^z = S\rangle. \tag{2.11}$$

The terms containing the raising operators annihilate the state because every spin projection is already maximal. Thus, by letting H act on $|\text{FM}\rangle$, we obtain

$$H|\text{FM}\rangle = E_0|\text{FM}\rangle, \tag{2.12}$$

where $E_0 = -cNJS^2/2$ is the classical ground state and $c = 2d$ is the number of nearest neighbors for a d-dimensional hypercubic lattice. Thus, $|\text{FM}\rangle$ is an eigenstate of H. It is possible to show that E_0 is the lowest possible energy, proving that it is the ground state.

To study the spin-wave excitations around the ground state, we substitute the lowest-order HP representation in Eq. (2.7) into Eq. (2.9). To diagonalize the resulting Hamiltonian, we introduce the Fourier transformation

$$b_i = \frac{1}{\sqrt{N}} \sum_{\mathbf{k}} e^{i\mathbf{k}\cdot\mathbf{r}_i} b_{\mathbf{k}}, \tag{2.13}$$

where $\mathbf{k}$ are the wavevectors within the first Brillouin zone and $\mathbf{r}_i$ is the real-space position of a lattice site. Simplifying the Hamiltonian, we obtain

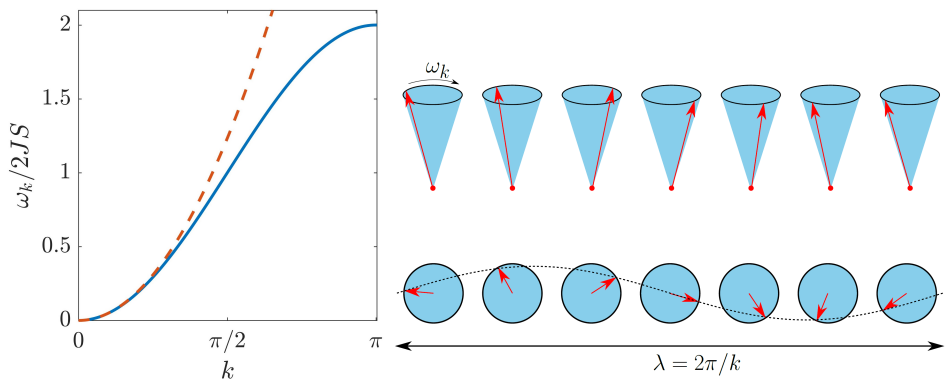$$H = E_0 + \sum_{\mathbf{k}} \omega_{\mathbf{k}} b_{\mathbf{k}}^\dagger b_{\mathbf{k}}, \tag{2.14}$$

where

$$\omega_{\mathbf{k}} = cJS \left(1 - \gamma_{\mathbf{k}} \right), \tag{2.15}$$

and

$$\gamma_{\mathbf{k}} = \frac{2}{c} \sum_{\boldsymbol{\delta}} \cos \left(\mathbf{k} \cdot \boldsymbol{\delta} \right). \tag{2.16}$$

Eq. (2.14) describes a set of independent harmonic oscillators with frequency $\omega_{\mathbf{k}}$. The quanta of the harmonic oscillators are magnons: they are quantized spin-wave excitations. In Fig. 2.3, we plot the spin wave and its dispersion relation in one dimension.

(a) The exact (solid) and long-wavelength (dashed) dispersion relation.

(b) Each spin precesses around the same axis with a frequency ω_k, resulting in a spin-wave with wavelength λ.

Figure 2.3. The dispersion relation (left) and spin wave (right) in a 1D ferromagnetic spin chain.

Finally, we comment on the validity of the low-order expansion of the HP representation for the isotropic Heisenberg ferromagnet. We show that whether ferromagnetic order exists depends on the dimensionality and temperature of the system. The ferromagnetic order parameter is the magnetization and is defined as $M = S - \Delta M$, where

$$\Delta M = -\frac{1}{N} \sum_{\mathbf{k}} \langle b_{\mathbf{k}}^{\dagger} b_{\mathbf{k}} \rangle. \tag{2.17}$$

Since magnons are bosonic particles, their distribution function is given by the Bose-Einstein distribution $\langle b_{\mathbf{k}}^{\dagger} b_{\mathbf{k}} \rangle = \left(e^{\beta \omega_{\mathbf{k}}} - 1 \right)^{-1}$, where β denotes the thermodynamic beta. At zero temperature $\Delta M = 0$, ferromagnetic order exists in all dimensions. In the long-wavelength limit, the magnon dispersion is quadratic $\omega_{\mathbf{k}} = JS\mathbf{k}^2$, and for finite temperatures, the inequality $JS\mathbf{k}^2 \ll k_{\mathrm{B}}T$ holds. The exact and leading order fluctuations of the d-dimensional magnetization then take the form

$$\Delta M = \frac{1}{N} \left(\frac{L}{2\pi} \right)^d \int \frac{\mathrm{d}\mathbf{k}}{e^{\beta JS\mathbf{k}^2} - 1}, \quad \text{and} \quad \Delta M \sim \frac{1}{N} \left(\frac{L}{2\pi} \right)^d \int \frac{\mathrm{d}\mathbf{k}}{\beta JS\mathbf{k}^2}, \tag{2.18}$$

respectively. Consequently, for finite temperatures, the isotropic Heisenberg ferro-
magnet is not ordered in one and two dimensions since the magnetization diverges
in the long-wavelength limit $|\mathbf{k}| \to 0$. In three dimensions the magnetization con-
verges, and the isotropic Heisenberg Hamiltonian allows for ferromagnetic order to
exist, also for finite temperatures.

2.4   Antiferromagnets

We next introduce the antiferromagnet where, in the classical picture, the spins pre-
fer to align antiparallel to those of their neighbors. The antiferromagnetic Heisenberg
Hamiltonian reads

$$H = J \sum_{\langle ij \rangle} \mathbf{S}_i \cdot \mathbf{S}_j, \tag{2.19}$$

with $J > 0$. We introduce two sublattices A and B. The spins associated with A
point in the opposite direction of the spins associated with B.

Based on the ferromagnetic case, we might naively expect for the quantum
ground state of the antiferromagnet to coincide with the classical Néel state

$$|\mathrm{N}\rangle = |\uparrow, \downarrow, \uparrow, \downarrow, \dots \rangle. \tag{2.20}$$

However, by acting with H on $|\mathrm{N}\rangle$, we find that the Néel state is not even an eigen-
state of the Hamiltonian. Consequently, quantum fluctuations are more important
in the antiferromagnetic case because they change the ground state from the classical
result. However, even though the exact ground state is not $|\mathrm{N}\rangle$, the spins may still
in some sense be antiparallel. For instance, the spins on the sublattice A may point
predominantly in the opposite direction of the spins on the sublattice B. In any
case, the HP representation has so far given predictions consistent with experiments.

Utilizing the spin decomposition and HP representation introduced in Eqs. (2.5)
and (2.6), respectively, we obtain

$$
\begin{aligned}
S^z_{i \in A} &= S - a^\dagger_i a_i, & S^z_{i \in B} &= -S + b^\dagger_i b_i, \\
S^+_{i \in A} &= \sqrt{2S}\sqrt{1 - \frac{a^\dagger_i a_i}{2S}}\, a_i, & S^+_{i \in B} &= \sqrt{2S}\, b^\dagger_i \sqrt{1 - \frac{b^\dagger_i b_i}{2S}}, \\
S^-_{i \in A} &= \sqrt{2S}\, a^\dagger_i \sqrt{1 - \frac{a^\dagger_i a_i}{2S}}, & S^-_{i \in A} &= \sqrt{2S}\sqrt{1 - \frac{b^\dagger_i b_i}{2S}}\, b_i.
\end{aligned}
\tag{2.21}
$$

Here, we introduce the bosonic operators a_i and b_i acting on the sublattices A and
B, respectively. As before, we introduce the Fourier transformations

$$a_{i \in A} = \frac{1}{\sqrt{N_A}} \sum_{\mathbf{k}} e^{\mathbf{k} \cdot \mathbf{r}_i} a_{\mathbf{k}}, \quad \text{and} \quad b_{i \in B} = \frac{1}{\sqrt{N_B}} \sum_{\mathbf{k}} e^{\mathbf{k} \cdot \mathbf{r}_i} b_{\mathbf{k}} \tag{2.22}$$

where the **k**-vectors are inside the first Brillouin zone. The numbers of spins present on sublattices A and B are denoted by N_A and N_B, respectively. The total number of lattice sites is denoted by $N = N_A + N_B$, and for simplicity we assume that $N_A = N_B$.

Utilizing the lowest-order HP representation and performing the Fourier transformation, we simplify the Hamiltonian to

$$H = E_0 + JSc \sum_{\mathbf{k}} \left[a_{\mathbf{k}}^{\dagger} a_{\mathbf{k}} + b_{\mathbf{k}}^{\dagger} b_{\mathbf{k}} + \gamma_{\mathbf{k}} \left(a_{\mathbf{k}} b_{-\mathbf{k}} + a_{\mathbf{k}}^{\dagger} b_{-\mathbf{k}}^{\dagger} \right) \right]. \tag{2.23}$$

To diagonalize the Hamiltonian, we perform a Bogoliubov transformation, which was historically first employed in the context of superconductivity [85, 86],

$$\begin{aligned} a_{\mathbf{k}} &= u_{\mathbf{k}} \alpha_{\mathbf{k}} + v_{\mathbf{k}} \beta_{-\mathbf{k}}^{\dagger}, \\ b_{\mathbf{k}} &= u_{\mathbf{k}} \beta_{\mathbf{k}} + v_{\mathbf{k}} \alpha_{-\mathbf{k}}^{\dagger}. \end{aligned} \tag{2.24}$$

Here, $\alpha(\beta)$ are bosonic operators, and $u(v)$ are scalars. The Bogoliubov transformation corresponds to a change of basis in the sublattice space. Since the bosonic commutation relations must be satisfied, we have the constraints $u_{\mathbf{k}}^2 - v_{\mathbf{k}}^2 = 1$, $u_{\mathbf{k}} = u_{-\mathbf{k}}$, and $v_{\mathbf{k}} = v_{-\mathbf{k}}$. Therefore, we choose the parameterization

$$u_{\mathbf{k}} = \cosh \theta_{\mathbf{k}}, \quad v_{\mathbf{k}} = \sinh \theta_{\mathbf{k}}, \tag{2.25}$$

introducing the hyperbolic rotation angle $\theta_{\mathbf{k}}$. The Hamiltonian is automatically diagonalized if we choose the rotation angle such that

$$\tanh 2\theta_{\mathbf{k}} = -\gamma_{\mathbf{k}}. \tag{2.26}$$

Utilizing the Bogoliubov transformation in Eq. (2.24), the parameterization in Eq. (2.25), and the choice of rotation angle in Eq. (2.26), the Hamiltonian in Eq. (2.23) simplifies to

$$H = E_0^{\mathrm{AF}} + \sum_{\mathbf{k}} \omega_{\mathbf{k}}^{\mathrm{AF}} \left(\alpha_{\mathbf{k}}^{\dagger} \alpha_{\mathbf{k}} + \beta_{\mathbf{k}}^{\dagger} \beta_{\mathbf{k}} \right). \tag{2.27}$$

Here, we introduce the antiferromagnetic ground state energy

$$E_0^{\mathrm{AF}} = -NJS^2 c/2 - NJSc/2 + \sum_{\mathbf{k}} \omega_{\mathbf{k}}^{\mathrm{AF}}, \tag{2.28}$$

and the magnon excitation energy

$$\omega_{\mathbf{k}}^{\mathrm{AF}} = JSc\sqrt{1 - \gamma_{\mathbf{k}}^2}. \tag{2.29}$$

The quantum ground state of the antiferromagnet is the state with zero α and β magnons. The ground state energy is E_0^{AF}, which consists of a classical contribution

$-NJS^2c/2$ and quantum corrections ΔE^{AF}. The quantum corrections ΔE^{AF} are always negative,

$$\Delta E^{\mathrm{AF}} = -NJSc/2 + \sum_{\mathbf{k}} \omega_{\mathbf{k}}^{\mathrm{AF}} = JSc \sum_{\mathbf{k}} \left(\sqrt{1 - \gamma_{\mathbf{k}}^2} - 1 \right) < 0. \tag{2.30}$$

The true antiferromagnetic quantum ground state can be viewed as the classical Néel state $|\mathrm{N}\rangle$, with prevalent quantum fluctuations that reduce its energy. In the ferromagnetic case, the quantum fluctuations are zero.

The excited states of the antiferromagnet can again be viewed as collective excitations of the magnons, i.e., spin waves. The excitation energy is given by $\omega_{\mathbf{k}}^{\mathrm{AF}}$. For each wavevector, there are two types of magnons corresponding to $\alpha_{\mathbf{k}}$ and $\beta_{\mathbf{k}}$. In the absence of magnetic fields and anisotropies, the sublattices are equivalent, and the magnons degenerate in energy. In the long-wavelength limit, we find a linear dispersion

$$\omega_{\mathbf{k}}^{\mathrm{AF}} \propto |\mathbf{k}|. \tag{2.31}$$

Finally, we consider the ordering of the antiferromagnetic ground state. Since the total magnetization is zero, we choose the magnetization of sublattice A as the order parameter; $M_A = S - \Delta M_A$. The quantum mechanical correction to the magnetization is

$$\Delta M_A = \frac{1}{N_A} \sum_{\mathbf{k}} \langle a_{\mathbf{k}}^{\dagger} a_{\mathbf{k}} \rangle. \tag{2.32}$$

The expectation value $\langle a_{\mathbf{k}}^{\dagger} a_{\mathbf{k}} \rangle$ is in this case not given by the Bose-Einstein distribution since the Hamiltonian is not diagonal in the $a_{\mathbf{k}}$-operator basis. We therefore need to utilize the Bogoliubov transformation in Eq. (2.24) to replace $\langle a_{\mathbf{k}}^{\dagger} a_{\mathbf{k}} \rangle$ with the $\alpha_{\mathbf{k}}$ and $\beta_{\mathbf{k}}$ operators, which satisfy the Bose-Einstein distribution. We find that the correction to the magnetization is the sum of temperature-independent and temperature-dependent parts

$$\Delta M_A = \Delta M_A \left(T = 0 \right) + \Delta M_A \left(T \neq 0 \right), \tag{2.33}$$

respectively. Explicitly, we have

$$\begin{aligned}
\Delta M_A \left(T = 0 \right) &= -\frac{1}{2} + \frac{1}{N_A} \sum_{\mathbf{k}} \frac{1}{\sqrt{1 - \gamma_{\mathbf{k}}^2}}, \\
\Delta M_A \left(T \neq 0 \right) &= \frac{2}{N_A} \sum_{\mathbf{k}} \frac{n_{\mathbf{k}}}{\sqrt{1 - \gamma_{\mathbf{k}}^2}}.
\end{aligned} \tag{2.34}$$

In three dimensions, both contributions are convergent. In two dimensions, the temperature-independent part is convergent, and the temperature-dependent part divergent. In one dimension, both contributions diverge.

2.5 Dimensional dependence of magnetic ordering and anisotropies

Thus far, we have established that the spin-wave theory predicts ferromagnetic or antiferromagnetic order in high dimensions. Our results are summarized in Tab. 2.1. The lack of order in one and two dimensions is a consequence of the Hohenberg-

Table 2.1. The effect of dimension and temperature on the magnetic order in isotropic Heisenberg ferromagnets and antiferromagnets.

Dimension	Temperature	Ferromagnet	Antiferromagnet
1	Zero	Order	No order
	Finite	No order	No order
2	Zero	Order	Order
	Finite	No order	No order
3	Zero	Order	Order
	Finite	Order	Order

Mermin-Wagner theorem: In one and two dimensions, continuous symmetries cannot be spontaneously broken at finite temperatures in systems with sufficiently short-range interactions [87–89]. The Hohenberg-Mermin-Wagner theorem can easily be circumvented by introducing anisotropic terms in the Hamiltonian. Anisotropic terms explicitly break a continuous symmetry such that the magnon dispersion becomes gapped, consequently removing the long-wavelength divergence in the order parameters. With the inclusion of anisotropic terms, magnetic ordering in low dimensions is possible.

One way to circumvent the Hohenberg-Mermin-Wagner theorem is to add the Zeeman interaction to the Heisenberg model:

$$H_Z = -\gamma \sum_i \mathbf{H} \cdot \mathbf{S}_i \qquad (2.35)$$

where the spins try to align parallel to an external magnetic field $\mathbf{H}$. The strength of the Zeeman coupling is given by the gyromagnetic ratio $\gamma > 0$. The interaction is quite general and may be generalized to position- and time-dependent magnetic fields. Nevertheless, it is not an intrinsic material property and therefore is not the main source for the existence of two-dimensional magnetic materials.

Anisotropy may be intrinsically linked with the material through the symmetry of the crystal axis and/or shape of electron orbitals. This may lead to specific

directions where spin ordering is energetically favorable. A simplified mathematical
description encapsulating the possibility of anisotropic directions is given by

$$H_A = \sum_\alpha K_\alpha \sum_i \left(\mathbf{S}_i \cdot \hat{\mathbf{e}}_\alpha\right)^2. \tag{2.36}$$

Here, K_α is the strength of the magnetic anisotropy along the anisotropy axis $\hat{\mathbf{e}}_\alpha$. If
$K_\alpha < 0 \, (K_\alpha > 0)$, then it is energetically (un)favorable for the spin to point parallel
or antiparallel to the anisotropy axis. To distinguish the two cases, we say that the
anisotropy axis $\hat{\mathbf{e}}_\alpha$ is either easy $(K_\alpha < 0)$ or hard $(K_\alpha > 0)$.

   The experimental search for two-dimensional magnetic materials has been long,
and these materials were discovered only recently [90–101]. To date, the list of exper-
imentally reported two-dimensional magnets is large and continues to grow larger,
giving generous flexibility in the choice of two-dimensional materials for specific
applications. In addition, one-dimensional spin chains can manifest as effectively
decoupled spin chains within two- or three-dimensional materials. A well known
example is tetramethyl ammonium manganese chloride (TMMC), where the one-
dimensional decoupled chains exhibit antiferromagnetism [102]. There are of course
other realizations of (quasi) one-dimensional magnets [103–106], but they are cur-
rently more rare and less experimentally investigated than their two- and three-
dimensional counterparts.

3
Superconductivity

In broad strokes, materials in their superconducting state are characterized by two properties: zero electrical resistance and the complete expulsion of magnetic fields from their interior. Only after Onnes managed to liquify helium did it become possible to reach sufficiently low temperatures to observe superconductivity in pure elements [107]. In 1911, he found that the electrical resistance of mercury vanished abruptly when its temperature T fell below its critical temperature T_c of approximately $4.1\,\mathrm{K}$ [108, 109]. On the other hand, the resistance of normal metals decreases with temperature, but saturates as the temperature approaches absolute zero. Bounds on the resistivity of superconductors are typically not found from direct measurements but from the decay of persistent currents. Experimentally, a current is set up by induction with a magnetic field in a superconducting ring and is found to persist without measurable decay after the magnetic field has been turned off [110].

Subsequently, in 1933, Meissner and Ochsenfeld observed that superconductors not only prevent a magnetic field from entering but also actively expel the magnetic field from its interior [111]. This is known as the Meissner or Meisner-Ochsenfeld effect and explicitly differentiates a superconductor from an ideal conductor. From classical electromagnetism, the general relation between the magnetic flux density

B, applied magnetic field **H**, and induced magnetization **M** is

$$\mathbf{B} = \mathbf{H} + 4\pi\mathbf{M}. \tag{3.1}$$

In addition, if the induced magnetization is parallel or antiparallel to the magnetic field, we have

$$\mathbf{M} = \chi\mathbf{H}, \tag{3.2}$$

with the magnetic susceptibility χ. Combining Eqs. (3.1) and (3.2), we obtain

$$\mathbf{B} = \mu\mathbf{H}, \tag{3.3}$$

where we introduce the magnetic permeability $\mu = 1 + 4\pi\chi$. The perfect expulsion of **B**, exhibited by superconductors, thus requires $\chi = -1/4\pi$. Since the magnetic susceptibility of a superconductor is negative and its magnetic susceptibility reaches the smallest value consistent with thermodynamic stability, superconductors exhibit perfect diamagnetism.

The Meissner effect causes an external, initially uniform, magnetic field to become nonuniform, with an associated energy cost. Thus, if the external field is larger than a material-dependent critical field H_c, the energy cost is so large that the superconducting state is not created; i.e., superconductivity breaks down for large external magnetic fields.

3.1   Classification of superconductors

Depending on the context, there are several useful ways of classifying different types of superconducting materials. Three common classification schemes are as follows:

- Low-temperature and high-temperature superconductivity, depending on whether the critical temperature T_c is lower or higher than $77\,\mathrm{K}$, the boiling point of liquid nitrogen, respectively.

- Type I and type II, according to the Meissner effect.

- Conventional and unconventional, depending on the underlying microscopic theory.

In the following, we briefly introduce type-I vs type-II and conventional vs unconventional superconductivity.

3.1.1 Type-I vs type-II

The difference between a type-I and a type-II superconductor can be understood by considering a superconducting material placed in a uniform external magnetic field $\mathbf{H}$. In this case, free charges in the superconductor induce magnetization $\mathbf{M}$, attempting to expel an external field from its interior [111].

In a type-I superconductor, the induced magnetization $\mathbf{M}$ precisely expels the external field $\mathbf{H}$ as long as the magnitude of the external field is smaller than some critical value H_c. For strong fields, where $|\mathbf{H}| > H_c$, superconductivity breaks down, and the material acts as a normal metal. The phase diagrams in the magnetization-magnetic field plane and the temperature-magnetic field plane are shown in Fig. 3.1a and 3.1c, respectively. Type-I superconductors are mainly composed of pure metals, e.g., mercury, aluminum, and lead, that show some conductivity at room temperature and exhibit low critical temperatures.

Type-II superconductors are characterized by two critical external magnetic fields H_{c1} and H_{c2}. Type-II superconductors exhibit an intermediate phase where the external field can penetrate the superconductor through magnetic field vortices when the external field satisfies $H_{c1} < |\mathbf{H}| < H_{c2}$. In the vortex state, a phenomenon known as flux pinning becomes possible, where the superconductor can "levitate" above a magnet and glide without friction. For strong fields, where $|\mathbf{H}| > H_{c2}$, superconductivity breaks down, and for weak fields, $|\mathbf{H}| < H_{c1}$ the external magnetic field is expelled. Fig. 3.1b and 3.1d shows these features. Metal alloys or com-
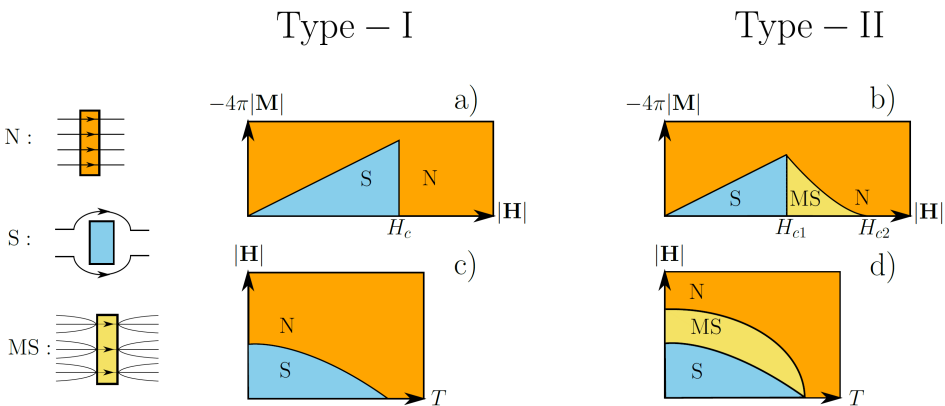

Figure 3.1. The phase diagrams in the $(|\mathbf{H}|, |\mathbf{M}|)$ and $(T, |\mathbf{H}|)$ planes, illustrating the qualitative difference between type-I and type-II superconductors. N, S, and MS represent the normal, superconducting, and mixed states, respectively.

plex oxide ceramics are typically type-II superconductors. Niobium, vanadium, and technetium are elemental type-II superconductors. Other famous examples of type-II superconductivity are found in cuprate-perovskite ceramic materials, typically achieving very high critical temperatures.

3.1.2   Conventional vs unconventional

The dissipationless currents (supercurrents) flowing through superconductors are carried by pairs of electrons known as Cooper pairs. The energy required for two electrons to form a Cooper pair is called the superconducting energy gap Δ. The electrons in the Cooper pair are bound together by an indirect attractive interaction. In the conventional theory of superconductivity, this attractive interaction is mediated by phonons, as described by the Bardeen-Cooper-Schrieffer (BCS) theory. If the superconductivity cannot be described by BCS theory, then the superconductor is unconventional. Most conventional superconductors are low-temperature superconductors or type-I superconductors, while unconventional superconductors are typically high-temperature or type-II superconductors. A complete understanding of unconventional superconductivity is considered by many to be the holy grail of condensed matter physics. While unconventional superconductivity is an interesting field of research, we only focus on conventional superconductors in our research papers. We therefore next briefly summarize the BCS theory of conventional superconductors.

3.2   BCS theory

In 1957, Bardeen, Cooper, and Schrieffer proposed the first successful microscopic theory of conventional superconductivity, aptly named BCS theory [112, 113]. At the time, the challenge was to come up with a microscopic theory that could explain the isotope effect, the mechanism behind supercurrents, and the Meissner effect, which all had been discovered experimentally [114]. The underlying idea is that electrons combine to form composite bosons called Cooper pairs, which exhibit superconducting properties. The superconducting ground state can be viewed as a Bose-Einstein condensate of a large number of Cooper pairs. For their discovery, they received the Nobel Prize in physics in 1972.

3.2.1 Attractive interactions between electrons

For two electrons to form a Cooper pair, an attractive electron-electron interaction must exist. Here, we briefly explain how such an attractive interaction may occur.

In a metal, the positively charged ions are localized, and the negatively charged electrons are itinerant. There is an attractive Couloumb interaction between electrons and ions. In a simple picture, this interaction may lead to a slight displacement of the ions that are in the vicinity of an electron. This displacement results in a weakly net positive charge density in the path left behind by the electron. Since the ion mass is much greater than the electron mass, it takes time before the ions are pulled back to their equilibrium positions. Thus, the positive charge density has a finite lifetime and can attract a second itinerant electron. The interpretation of this is that there exists a retarded and indirect attractive interaction between electrons mediated by phonons that may cause superconductivity. Electron-electron repulsion is minimized if the electrons travel in opposite directions with opposite spins. This classical explanation is schematically illustrated in Fig. 3.2. We emphasize that superconductivity is an intrinsic quantum mechanical phenomenon and that the above classical explanation should not be stretched much further. The main message is to illustrate that attractive electron-electron interactions may exist.
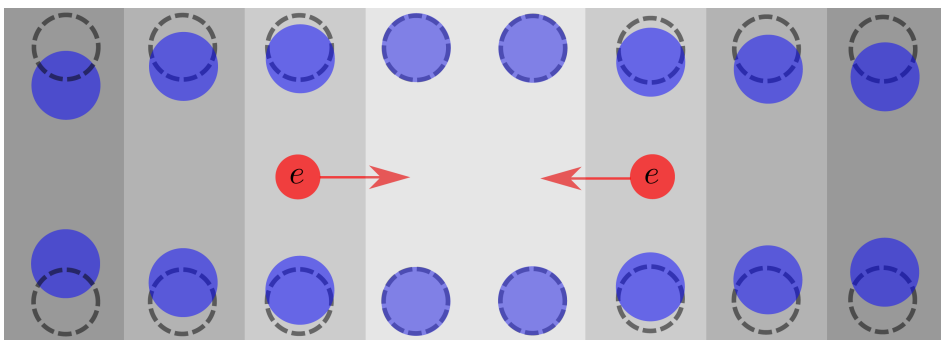

Figure 3.2. The classical analogy describing the attractive interaction between two electrons mediated by phonons that may produce superconductivity. Itinerant electrons (red) drag positively charged ions (blue) out of their equilibrium positions, creating a positive charge density. The positive charge density attracts other electrons, allowing an indirect attractive electron-electron interaction. The gray color gradient in the background indicates the strength of the positive charge density.

More rigorously, the electrons in a metal experience both Coulomb electron-electron interactions mediated by photons and electron-electron interactions me-

diated by phonons.   Since photons are massless and phonons are massive, the
Couloumb electron-electron interaction is effectively instantaneous, and the electron-
electron interaction mediated by phonons is effectively retarded. Thus, the photon-
and phonon-mediated electron-electron interactions are frequency (ω) independent
and dependent, respectively. Taking both of these interactions into account, we can
show that the simplified effective potential between two electrons is given by

$$V_{\text{eff}} = V_{\text{C}}(\mathbf{q}, k_{\text{s}}) \left(1 + \frac{\omega_{\mathbf{q}}^2}{\omega^2 - \omega_{\mathbf{q}}^2} \right). \tag{3.4}$$

Here, $V_{\text{C}}(\mathbf{q}, k_{\text{s}})$, $\mathbf{q}$, k_s, and $\omega_{\mathbf{q}}$ are the screened Coulomb potential, the momentum
transfer between electrons, the inverse screening length, and the phonon frequency,
respectively. The scale of the phonon frequency is set by the Debye frequency ω_{D}.
We emphasize that Eq. (3.4) is a simplification, where the metal is approximated
by a fluid of electrons and point ions, with complete neglect of the crystal structure
and finite ion-core size effects [115]. Nevertheless, it captures some of the qualitative
features of the possible attractive electron-electron interaction mediated by phonons.
The important point is that if the electron frequency is smaller than and sufficiently
close to the Debye frequency, the net electron-electron interaction can be attractive,
as shown in Fig. 3.3.

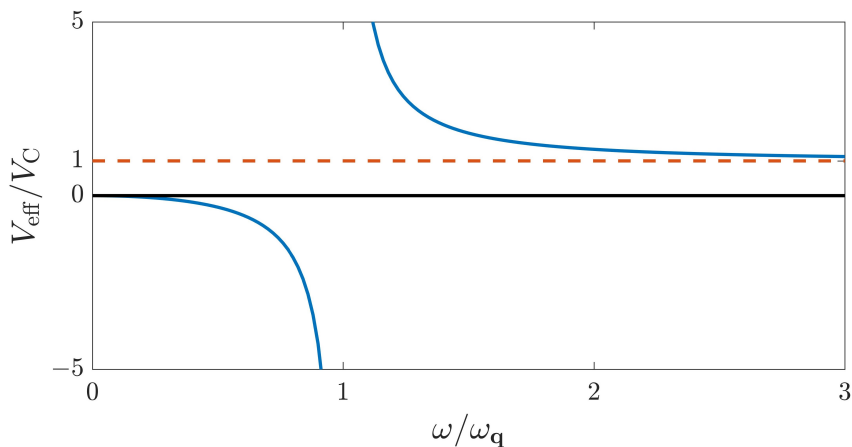**Figure 3.3.** The effective electron-electron interaction potential $V_{\text{eff}}/V_{\text{C}}$ as a function
of the frequency $\omega/\omega_{\mathbf{q}}$. The formation of Cooper pairs, and therefore superconductiv-
ity, is possible when the potential is attractive, as shown here for $\omega/\omega_{\mathbf{q}} < 1$. For higher
frequencies, the potential becomes repulsive, and superconductivity breaks down.

3.2.2 Cooper instability

In 1956, Cooper presented the basic idea that an arbitrarily weak attraction can bind electrons into bound states. Today, we recognize these bound states as Cooper pairs [116]. Specifically, he demonstrated that the Fermi sea of electrons is unstable against the formation of at least one Cooper pair, given that the electron-electron interaction is attractive. To understand the formation of the Cooper pair, we consider a simple model of two electrons added to a Fermi sea at zero temperature. We allow the two electrons to interact with each other through a potential V_{e-e} but not with the Fermi sea, except via the Pauli exclusion principle. For simplicity, we assume that the two electrons have opposite momenta and spins.

The relevant two-body problem is governed by the eigenvalue equation

$$H|\mathbf{k}, -\mathbf{k}\rangle = E|\mathbf{k}, -\mathbf{k}\rangle, \tag{3.5}$$

where H is the total Hamiltonian and $|\mathbf{k}, -\mathbf{k}\rangle$ is the eigenstate, with eigenenergy E. The total Hamiltonian is $H = H_0 + V_{e-e}$, where the first term represents the kinetic energy operator of the two electrons. In the absence of the interaction potential, the eigenvalue problem is

$$H_0|\mathbf{k}, -\mathbf{k}\rangle_0 = \epsilon_{\mathbf{k}}|\mathbf{k}, -\mathbf{k}\rangle_0, \tag{3.6}$$

with solution $|\mathbf{k}, -\mathbf{k}\rangle_0$ and kinetic energy $\epsilon_{\mathbf{k}}$.

We solve Eq. (3.5) by using the expansion

$$|\mathbf{k}, -\mathbf{k}\rangle = \sum_{\mathbf{q}} a_{\mathbf{q}}|\mathbf{q}, -\mathbf{q}\rangle_0, \tag{3.7}$$

where $\mathbf{q}$ satisfies $\epsilon_{\mathbf{q}} > 2\epsilon_{\mathrm{F}}$, and ϵ_{F} is the Fermi energy of the Fermi sea. By substituting Eq. (3.7) into Eq. (3.5), we obtain

$$a_{\mathbf{k}}(\epsilon_{\mathbf{k}} - E) = -\sum_{\mathbf{q}} a_{\mathbf{q}} V_{\mathbf{k}, \mathbf{q}}, \tag{3.8}$$

where we use that $\langle \mathbf{k}, -\mathbf{k}|\mathbf{q}, -\mathbf{q}\rangle = \delta_{\mathbf{k}, \mathbf{q}}$ and define $V_{\mathbf{k}, \mathbf{q}} = \langle \mathbf{k}, -\mathbf{k}|V_{e-e}|\mathbf{q}, -\mathbf{q}\rangle$. To proceed, we must specify the potential $V_{\mathbf{k}, \mathbf{q}}$. Based on our discussion of the phonon-mediated electron-electron interaction, we assume that the electrons interact in a thin shell around the Fermi surface and neglect all other interactions

$$V_{\mathbf{k}, \mathbf{q}} = \begin{cases} -V, & |\epsilon_{\mathbf{k}} - 2\epsilon_{\mathrm{F}}|, |\epsilon_{\mathbf{q}} - 2\epsilon_{\mathrm{F}}| < 2\hbar\omega_{\mathrm{D}}, \\ 0, & \text{otherwise.} \end{cases} \tag{3.9}$$

By using this simplified potential and converting the momentum sum to an energy integral, we obtain

$$a(\epsilon)(\epsilon - E) = V \int_{2\epsilon_{\mathrm{F}}}^{2\epsilon_{\mathrm{F}} + 2\hbar\omega_{\mathrm{D}}} \mathrm{d}\varepsilon\, a(\varepsilon) N(\varepsilon) \equiv W, \tag{3.10}$$

where $N(\varepsilon)$ is the density of states. Note that the right side of Eq. (3.10) is energy independent. The coefficients in the expansion (3.7) therefore take the form

$$a(\epsilon) = \frac{W}{\epsilon - E}. \tag{3.11}$$

The eigenvalues can be determined by substituting Eq. (3.11) into Eq. (3.10), and we then obtain

$$\frac{1}{\lambda} = \ln\left(1 + \frac{2\hbar\omega_{\mathrm{D}}}{\Delta}\right). \tag{3.12}$$

Here, we assume that $N(\varepsilon) \approx N(\epsilon_{\mathrm{F}})$ and define the binding energy $\Delta = 2\epsilon_{\mathrm{F}} - E$ of the electron pair, and $\lambda = V N(\epsilon_{\mathrm{F}})$. When, the right-hand side of Eq. (3.12) is positive, it follows that we can obtain a bound-state solution only if the potential is attractive $V > 0$. For an attractive potential, the binding energy becomes

$$\Delta = \frac{2\hbar\omega_{\mathrm{D}}}{e^{1/\lambda} - 1} \approx 2\hbar\omega_{\mathrm{D}} e^{-1/\lambda} > 0, \tag{3.13}$$

where we, in the last step, assume that $\lambda \ll 1$. Eq. (3.13) shows that regardless of how small the attractive interaction is, the binding energy is always positive, and a bound state is formed.

3.2.3   Diagonalizing the BCS Hamiltonian

In the previous section, we demonstrate that two electrons close to the Fermi surface form a Cooper pair in the presence of an arbitrarily weak interaction. We therefore expect that a corresponding many-particle system of interacting electrons and phonons may result in a new ground state consisting of a large number of Cooper pairs.

The effective Hamiltonian describing phonon-mediated superconductivity is [115]

$$H = \sum_{\mathbf{k}\sigma} \xi_{\mathbf{k}} c_{\mathbf{k}\sigma}^{\dagger} c_{\mathbf{k}\sigma} + \frac{1}{N} \sum_{\mathbf{kq}} V_{\mathbf{kq}} c_{\mathbf{k}\uparrow}^{\dagger} c_{-\mathbf{k}\downarrow}^{\dagger} c_{-\mathbf{q}\downarrow} c_{\mathbf{q}\uparrow}. \tag{3.14}$$

In general, the Hamiltonian describes N itinerant fermions $c_{\mathbf{k}}^{(\dagger)}$, with kinetic energy $\xi_{\mathbf{k}}$, interacting with each other through a potential $V_{\mathbf{kq}}$. The interaction couples only fermions of opposite spin and momentum.

The quartic term in Eq. (3.14) can be decoupled by performing a BCS mean-field approximation of the form

$$c_{\mathbf{k}\uparrow}^{\dagger} c_{-\mathbf{k}\downarrow}^{\dagger} c_{-\mathbf{q}\downarrow} c_{\mathbf{q}\uparrow} \approx \langle c_{\mathbf{k}\uparrow}^{\dagger} c_{-\mathbf{k}\downarrow}^{\dagger} \rangle c_{-\mathbf{q}\downarrow} c_{\mathbf{q}\uparrow} + c_{\mathbf{k}\uparrow}^{\dagger} c_{-\mathbf{k}\downarrow}^{\dagger} \langle c_{-\mathbf{q}\downarrow} c_{\mathbf{q}\uparrow} \rangle - \langle c_{\mathbf{k}\uparrow}^{\dagger} c_{-\mathbf{k}\downarrow}^{\dagger} \rangle \langle c_{-\mathbf{q}\downarrow} c_{\mathbf{q}\uparrow} \rangle, \tag{3.15}$$

where it is convenient to define the mean-field quantity

$$\Delta_{\mathbf{k}} = -\frac{1}{N} \sum_{\mathbf{q}} V_{\mathbf{k}\mathbf{q}} \langle c_{-\mathbf{q}\downarrow} c_{\mathbf{q}\uparrow} \rangle, \tag{3.16}$$

commonly referred to as the superconducting gap. The mean-field BCS Hamiltonian is then

$$H = \sum_{\mathbf{k}\sigma} \xi_{\mathbf{k}} c_{\mathbf{k}\sigma}^{\dagger} c_{\mathbf{k}\sigma} - \sum_{\mathbf{k}} \left(\Delta_{\mathbf{k}} c_{\mathbf{k}\uparrow}^{\dagger} c_{-\mathbf{k}\downarrow}^{\dagger} + \text{h.c.} \right) + \sum_{\mathbf{k}} \Delta_{\mathbf{k}} \langle c_{\mathbf{k}\uparrow}^{\dagger} c_{-\mathbf{k}\downarrow}^{\dagger} \rangle. \tag{3.17}$$

To determine the ground state, we diagonalize the mean-field BCS Hamiltonian by performing a Bogoliubov transformation. Concretely, we introduce new fermion operators $\gamma_{\mathbf{k}}^{(\dagger)}$ and the coefficients $u_{\mathbf{k}}$ and $v_{\mathbf{k}}$ through the linear transformation:

$$\begin{aligned} c_{\mathbf{k}\uparrow} &= u_{\mathbf{k}}^{*} \gamma_{\mathbf{k}\uparrow} + v_{\mathbf{k}} \gamma_{-\mathbf{k}\downarrow}^{\dagger}, \\ c_{-\mathbf{k}\downarrow}^{\dagger} &= u_{\mathbf{k}} \gamma_{-\mathbf{k}\downarrow}^{\dagger} - v_{\mathbf{k}}^{*} \gamma_{\mathbf{k}\uparrow}^{\dagger}. \end{aligned} \tag{3.18}$$

To preserve the fermionic anticommutation relations, the normalization condition

$$|u_{\mathbf{k}}|^2 + |v_{\mathbf{k}}|^2 = 1 \tag{3.19}$$

must be satisfied. In order to diagonalize Eq. (3.17), we need to choose coefficients so that the requirement

$$\frac{v_{\mathbf{k}}}{u_{\mathbf{k}}} = \frac{\sqrt{\xi_{\mathbf{k}}^2 + |\Delta_{\mathbf{k}}|^2} - \xi_{\mathbf{k}}}{\Delta_{\mathbf{k}}^{*}} \tag{3.20}$$

is satisfied. Combining Eqs. (3.19) with (3.20), we obtain the explicit form of the coefficients

$$\begin{aligned} |u_{\mathbf{k}}|^2 &= \frac{1}{2} \left(1 + \frac{\xi_{\mathbf{k}}}{\sqrt{\xi_{\mathbf{k}}^2 + |\Delta_{\mathbf{k}}|^2}} \right), \\ |v_{\mathbf{k}}|^2 &= \frac{1}{2} \left(1 - \frac{\xi_{\mathbf{k}}}{\sqrt{\xi_{\mathbf{k}}^2 + |\Delta_{\mathbf{k}}|^2}} \right), \end{aligned} \tag{3.21}$$

that diagonalize Eq. (3.17). The mean-field BCS Hamiltonian in its diagonal form is

$$H = E_0 + \sum_{\mathbf{k}\sigma} E_{\mathbf{k}} \gamma_{\mathbf{k}\sigma}^{\dagger} \gamma_{\mathbf{k}\sigma}, \tag{3.22}$$

where

$$E_0 = \sum_{\mathbf{k}} \left(\xi_{\mathbf{k}} - E_{\mathbf{k}} + \Delta_{\mathbf{k}} \langle c_{\mathbf{k}\uparrow}^{\dagger} c_{-\mathbf{k}\downarrow}^{\dagger} \rangle \right) \tag{3.23}$$

is the ground-state energy and

$$E_{\mathbf{k}} = \sqrt{\xi_{\mathbf{k}}^2 + |\Delta_{\mathbf{k}}|^2} \tag{3.24}$$

is the excitation energy. In Fig. 3.4, we plot the excitation energy, with $\xi_{\mathbf{k}} = \frac{\hbar^2}{2m}\left(\mathbf{k}^2 - k_{\mathrm{F}}^2\right)$. Here, k_{F} and $E_{\mathrm{F}} = \frac{\hbar^2}{2m}k_{\mathrm{F}}^2$ denote the Fermi wavevector and energy, respectively. Note that the mean-field quantity $\Delta_{\mathbf{k}}$ appears as a gap in the dispersion separating the ground state from its excited states.
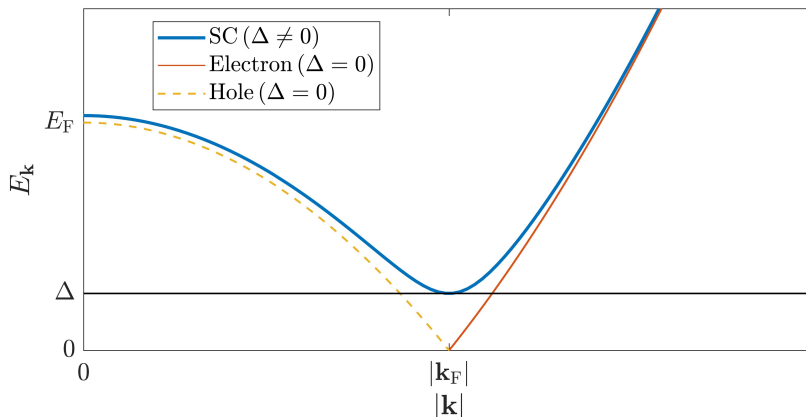

Figure 3.4. The BCS excitation energies $E_{\mathbf{k}}$ with $\xi_{\mathbf{k}} = \frac{\hbar^2}{2m}\left(\mathbf{k}^2 - k_{\mathrm{F}}^2\right)$ in the super-conducting and normal metal limits $\Delta_{\mathbf{k}} = \Delta > 0$ and $\Delta_{\mathbf{k}} = 0$, respectively. Note that with the onset of the superconducting gap, the electron (red) and hole (green) branches merge to form the quasiparticle (blue) dispersion.

From the Bogoliubov transformation in Eq. (3.18) and Fig. 3.4, we note that the quasiparticle excitations of the system consist of a linear combination of electrons and holes. For quasiparticles with $|\mathbf{k}| > |\mathbf{k}_{\mathrm{F}}|$ or $|\mathbf{k}| < |\mathbf{k}_{\mathrm{F}}|$, we say that the particles are electron-like or hole-like, respectively. This nomenclature can be understood by considering the normal metal limit $\Delta_{\mathbf{k}} \to 0$, where the Bogoliubov coefficients reduce to

$$|u_{\mathbf{k}}|^2 = \begin{cases} 0, & |\mathbf{k}| < |\mathbf{k}_{\mathrm{F}}|, \\ 1, & |\mathbf{k}| > |\mathbf{k}_{\mathrm{F}}|, \end{cases} \qquad |v_{\mathbf{k}}|^2 = \begin{cases} 1, & |\mathbf{k}| < |\mathbf{k}_{\mathrm{F}}|, \\ 0, & |\mathbf{k}| > |\mathbf{k}_{\mathrm{F}}|. \end{cases} \tag{3.25}$$

To some extent, we can therefore say that $u_{\mathbf{k}}$ and $v_{\mathbf{k}}$ determine the degree to which a quasiparticle exhibits "electron-like" and "hole-like" properties, respectively.

Finally, we briefly comment on the form of the superconducting quantum ground state $|\Psi_{\mathrm{BCS}}\rangle$ in terms of the normal metal vacuum of electrons $|0\rangle$. The superconducting quantum ground state is defined by the equation

$$\gamma_{\mathbf{k}\sigma}|\Psi_{\mathrm{BCS}}\rangle = 0. \tag{3.26}$$

By utilizing the Bogoliubov transformation in Eq. (3.18), we can show that

$$|\Psi_{\mathrm{BCS}}\rangle = \prod_{\mathbf{k}} \left(u_{\mathbf{k}} + v_{\mathbf{k}} c_{\mathbf{k}\uparrow}^{\dagger} c_{-\mathbf{k}\downarrow}^{\dagger} \right) |0\rangle. \tag{3.27}$$

Physically, this means that the superconducting quantum ground state consists of a combination of a large number of Cooper pairs.

3.2.4 The gap equation

In general, the superconducting gap must be determined self-consistently from its definition in Eq. (3.16). Since the Bogoliubov quasiparticles are fermions, their statistics are governed by the Fermi-Dirac distribution such that

$$\langle \gamma_{\mathbf{k}\sigma}^{\dagger} \gamma_{\mathbf{k}\sigma} \rangle = \frac{1}{1 + e^{E_{\mathbf{k}}/k_{\mathrm{B}}T}}. \tag{3.28}$$

By then utilizing the Bogoliubov transformation, we can rewrite Eq. (3.16) as the self-consistent gap equation

$$\Delta_{\mathbf{k}} = -\frac{1}{N} \sum_{\mathbf{q}} \frac{V_{\mathbf{k}\mathbf{q}} \Delta_{\mathbf{q}}}{2E_{\mathbf{q}}} \tanh\left(\frac{E_{\mathbf{q}}}{2k_{\mathrm{B}}T}\right). \tag{3.29}$$

To solve the gap equation, it is necessary to specify the potential. Based on our discussion of phonon-mediated superconductivity, we choose the potential

$$V_{\mathbf{k}\mathbf{q}} = \begin{cases} -V_0, & |\xi_{\mathbf{k}}|, |\xi_{\mathbf{q}}| < \hbar\omega_{\mathrm{D}}, \\ 0, & \text{otherwise.} \end{cases} \tag{3.30}$$

We also assume that the superconducting gap is uniform and isotropic $\Delta_{\mathbf{k}} = \Delta$, physically restricting us to s-wave superconductivity. With these two assumptions, the gap equation becomes

$$1 = \frac{V_0}{N} \sum_{|\mathbf{k}|<k_{\mathrm{D}}} \frac{1}{2E_{\mathbf{k}}} \tanh\left(\frac{E_{\mathbf{k}}}{2k_{\mathrm{B}}T}\right). \tag{3.31}$$

By introducing the density of states per spin ρ and assuming that the Fermi energy is the largest energy scale in the problem, we can rewrite the gap equation as

$$1 = V_0 \rho_{\mathrm{F}} \int_0^{\hbar\omega_{\mathrm{D}}} \frac{d\epsilon}{\sqrt{\epsilon^2 + \Delta^2}} \tanh\left(\frac{\sqrt{\epsilon^2 + \Delta^2}}{2k_{\mathrm{B}}T}\right) \tag{3.32}$$

where we approximate the density of states by its value at the Fermi level ρ_{F}.

We can analytically calculate the zero-temperature gap Δ_0 by assuming that $\Delta_0 \ll \hbar\omega_{\mathrm{D}}$ in Eq. (3.32), and we then obtain

$$\Delta_0 = 2\hbar\omega_{\mathrm{D}} e^{-1/V_0\rho_{\mathrm{F}}}. \tag{3.33}$$

We can also use use Eq. (3.32) to analytically determine the critical temperature T_C where the gap vanishes. By assuming that $\hbar\omega_D \gg k_B T_C$, we obtain

$$T_C = \frac{2e^{\gamma_E}}{\pi} \frac{\hbar\omega_D}{k_B} e^{-1/V_0\rho_F}, \qquad (3.34)$$

where γ_E is the Euler–Mascheroni constant. Since the squared Debye frequency is inversely proportional to the phonon mass, the expression in Eq. (3.34) predicts that $T_C \propto M^{-1/2}$, in agreement with the experimentally verified isotope effect [117, 118]. By combining Eqs. (3.33) and (3.34), we obtain the celebrated universal BCS relation

$$\frac{\Delta_0}{k_B T_C} = \pi e^{-\gamma_E} \approx 1.76. \qquad (3.35)$$

3.3   The Bogoliubov de-Gennes equations

The research papers [2, 3] supplementing this thesis focus on transport through superconducting heterostructures. To this end, a convenient framework is the Bogoliubov-de Gennes (BdG) equations [61, 64, 119]. There are of course other important frameworks such as the Usadel formalism [120], but here, we restrict ourselves to the formalism utilized in the research papers.

To demonstrate one possible derivation of the BdG equations, it is convenient to start with the simplest real-space mean-field Hamiltonian exhibiting superconductivity of the form

$$H = -t \sum_{\langle ij \rangle} c^{\dagger}_{i,\sigma} c_{j,\sigma} - V_0 \sum_{i,\sigma} c^{\dagger}_{i,\sigma} c_{i,\sigma} + \sum_{i\sigma} \left(\sigma \Delta c^{\dagger}_{i,\sigma} c^{\dagger}_{i,-\sigma} + \text{h.c.} \right). \qquad (3.36)$$

Here, t represents the kinetic energy of itinerant charges, V_0 is an arbitrary constant that determines the minimum of the dispersion, and Δ is the superconducting gap. The BdG equations derived from this Hamiltonian are used to model normal metal-superconductor junctions in Chapter 6. For concreteness and simplicity, we choose here to embed the Hamiltonian (3.36) on a square lattice with lattice spacing a. Other choices, such as triangular-, hexagonal-, Kagome-, and 3D-lattices, are of course also possible. To describe more complicated systems including interactions such as ferromagnetism, antiferromagnetism, and spin-orbit coupling, we need only to add appropriate interactions to Eq. (3.36) and to employ the same procedure that we now demonstrate.

We utilize the Fourier representation of the fermion operators

$$c_j = \frac{1}{\sqrt{N}} \sum_{\mathbf{k}} e^{i\mathbf{k}\cdot\mathbf{r}_j} c_{\mathbf{k}}, \qquad (3.37)$$

where N is the number of lattice sites, $\mathbf{k}$ is a wavenumber within the first Brillouin zone, and $\mathbf{r}_j$ is the position vector of site j. The anticommutation relations of the fermion operators guarantee that

$$\frac{1}{N} \sum_j e^{i(\mathbf{k}-\mathbf{q})\cdot\mathbf{r}_j} = \delta_{\mathbf{k},\mathbf{q}}. \tag{3.38}$$

We then obtain the Hamiltonian

$$H = \sum_{\mathbf{k},\sigma} \gamma_\mathbf{k} c_{\mathbf{k},\sigma}^\dagger c_{\mathbf{k},\sigma} - V_0 \sum_{\mathbf{k},\sigma} c_{\mathbf{k},\sigma}^\dagger c_{\mathbf{k},\sigma} + \sum_{\mathbf{k},\sigma} \left(\sigma \Delta c_{\mathbf{k},\sigma}^\dagger c_{-\mathbf{k},-\sigma}^\dagger + \text{h.c.} \right), \tag{3.39}$$

where $\gamma_\mathbf{k} = -t \sum_{\boldsymbol{\delta}} e^{i\mathbf{k}\cdot\boldsymbol{\delta}}$ is the lattice-dependent structure factor and $\boldsymbol{\delta}$ is a vector connecting nearest neighbors. Since the superconducting gap couples electrons and holes, it is natural to explicitly separate the electron and hole degrees of freedom by utilizing the anticommutation relations to write

$$\sum_{\mathbf{k},\sigma} c_{\mathbf{k}\sigma}^\dagger c_{\mathbf{k}\sigma} = \frac{1}{2} \sum_{\mathbf{k},\sigma} \left(\delta_{i,j} + c_{\mathbf{k},\sigma}^\dagger c_{\mathbf{k},\sigma} - c_{-\mathbf{k},-\sigma} c_{-\mathbf{k},-\sigma}^\dagger \right). \tag{3.40}$$

The Hamiltonian then takes the form

$$H = H_0 + \sum_{\mathbf{k}\sigma} \left[c_{\mathbf{k},\sigma}^\dagger \; c_{-\mathbf{k},-\sigma} \right] \begin{bmatrix} \gamma_\mathbf{k} - V_0 & \sigma\Delta \\ \sigma\Delta^* & -\gamma_{-\mathbf{k}} + V_0 \end{bmatrix} \begin{bmatrix} c_{\mathbf{k},\sigma} \\ c_{-\mathbf{k},-\sigma}^\dagger \end{bmatrix}, \tag{3.41}$$

where H_0 is a constant that shifts the minimum value of the dispersion.

To obtain the continuum limit, we can expand the structure factor around the minimum point in the Brillouin zone. For the square lattice, we expand around the Γ-point. We then obtain

$$\gamma_\mathbf{k} \approx \frac{\hbar^2}{2m} \left(\mathbf{k}^2 - k_0^2 \right), \tag{3.42}$$

where m is the effective mass and k_0 is a constant. Specifically, we make the standard identification $a^2 t = \hbar^2/2m$ and define $k_0 = \sqrt{2}/a$. If we now introduce the electron and hole operators as $\psi_{e,\sigma}^\dagger = c_{\mathbf{k},\sigma}^\dagger$ and $\psi_{h,\sigma}^\dagger = c_{-\mathbf{k},-\sigma}$, respectively, the total continuum BdG Hamiltonian becomes

$$H = H_0 + \sum_\sigma \left[\psi_{e,\sigma}^\dagger \; \psi_{h,\sigma}^\dagger \right] \begin{bmatrix} H_e & \sigma\Delta \\ \sigma\Delta^* & H_h \end{bmatrix} \begin{bmatrix} \psi_{e,\sigma} \\ \psi_{h,\sigma} \end{bmatrix}, \tag{3.43}$$

where we absorb the constant $\hbar^2 k_0^2/2m$ into H_0. Here, $H_e = \hbar^2\mathbf{k}^2/2m - V_0$ and $H_h = -\hbar\mathbf{k}^2/2m + V_0$ are the Hamiltonians for free itinerant electrons and holes, respectively. Finally, we use the first quantization prescription to replace the wavenumber with the differential operator

$$\mathbf{k} = -i\nabla. \tag{3.44}$$

We then obtain the BdG equation

$$\begin{bmatrix} H_e & \sigma\Delta \\ \sigma\Delta^* & H_h \end{bmatrix} \begin{bmatrix} \psi_{e,\sigma} \\ \psi_{h,\sigma} \end{bmatrix} = E \begin{bmatrix} \psi_{e,\sigma} \\ \psi_{h,\sigma} \end{bmatrix}. \tag{3.45}$$

where $\psi_{e,\sigma}$ are wavefunctions and E is the excitation energy relative to the potential V_0.

The transport properties for superconducting heterostructures are described well by the BdG equation (3.45). In principle, the BdG equation needs to be solved self-consistently since the superconducting gap depends on the electron and hole wavefunctions. However, a useful approximation is to assume that the gap acts as a step-like potential describing an abrupt transition from a superconductor to a nonsuperconducting material. We present explicit examples of solving the BdG equation in Chapters 6 and 7.

3.3.1   Possible generalizations and extensions

As it is, the Hamiltonian in Eq. (3.43) can be used to study transport across normal metal-superconductor interfaces. However, there are several natural ways of modifying the starting point in Eq. (3.36) to generalize the BdG Hamiltonian to describe more complicated systems. Here, we restrict ourselves to interactions that are either related to the research papers or natural extensions that may be interesting to pursue in future works.

Itinerant magnetism

To describe superconductors with either intrinsic or proximity to magnetic metals, we can utilize the *s-d* interaction [75, 121–123]. Physically, the spin of itinerant *s* electrons couples with the spin of localized *d* electrons. If we assume that the localized spins have negligible deviations from their ordering direction $\mathbf{m}_i$, then the isotropic *s-d* interaction is

$$H_J = J \sum_{i,\alpha,\beta} c_{i,\alpha}^\dagger \left(\mathbf{m}_i \cdot \boldsymbol{\sigma} \right)_{\alpha,\beta} c_{i,\beta}. \tag{3.46}$$

Here, J is the *s-d* exchange strength, and $\boldsymbol{\sigma}$ is a vector of Pauli matrices describing the itinerant spins. If the order parameter $\mathbf{m}_i$ is independent of the lattice sites, then H_J describes the *s-d* interaction in a ferromagnetic metal. To describe collinear antiferromagnetism, we introduce two sublattices (A and B) and require that

$$\mathbf{m}_{i \in A} = -\mathbf{m}_{i \in B}. \tag{3.47}$$

Transport through any other magnetic structure, such as noncollinear (anti)ferromagnets, spin spirals, and skyrmions, can be described by choosing an appropriate order parameter vector $\mathbf{m}_i$.

Nonideal and uncompensated interfaces

To model generic microscopic interface effects in the continuum limit, we phenomenologically introduce a repulsive spin-independent delta-function potential

$$H_V = V\delta(x - x_0), \tag{3.48}$$

with strength $V > 0$ located at the interface $x = x_0$. Examples of such interface effects include intrinsic contact resistance across the interface, energy barriers, and mismatches between Fermi wavevectors, effective masses, and lattice structures [124–126].

For two-sublattice and collinear antiferromagnets, the effects of an uncompensated interface may also be important. To include such an effect in our description, we use a spin-dependent potential barrier, where only one of the sublattices gives a nonzero contribution. By letting the Pauli matrices $\boldsymbol{s}$ and $\boldsymbol{\sigma}$ denote the spin and sublattice degrees of freedom, the interaction takes the form

$$H_{\text{Un.}} = \frac{h}{2}\Big[(\mathbf{m} \cdot \mathbf{s}) \otimes (\sigma_0 + \sigma_z)\Big]\delta(x - x_0). \tag{3.49}$$

Here, h and $\boldsymbol{m}$ are the strength and direction of the uncompensated magnetic moment, respectively.

Spin-orbit coupling

An important interaction in solid-state physics is spin-orbit coupling (SOC) [127]. Formally, SOC can be understood as a relativistic effect for an electron moving with velocity v in an electric potential V. By expanding the Dirac equation in the parameter v/c, we obtain the Schrödinger equation with a relativistic correction of the form [128]

$$H_{\text{SOC}} = -\frac{\hbar}{(2mc)^2}\boldsymbol{\sigma} \cdot (\nabla V \times \mathbf{p}). \tag{3.50}$$

Here, m, c, $\boldsymbol{\sigma}$, and $\mathbf{p}$ are the electron mass, speed of light in vacuum, electron spin, and electron momentum, respectively. Depending on the form of the potential, SOC takes different forms. Physically, SOC can be thought of as a momentum-dependent Zeeman coupling between the electron spin and the effective magnetic field generated in the rest frame of the moving electron.

In broad strokes, SOC can be divided into two types:

1. *Symmetry independent SOC.* Exists in all types of crystals and originates from SOC in atomic orbitals.

2. *Symmetry dependent SOC.* Exists only in crystals without inversion symmetry.

   - If the inversion symmetry is broken by an interface, it is known as Rashba SOC [129, 130].

   - If the inversion symmetry is broken in the bulk, such as in Zincblende structures, it is known as Dresselhaus SOC [131].

   - There are also other more general types of SOC, where the inversion symmetry is broken by other means. A well-known example is the Kane-Mele model [132, 133].

In the tight-binding framework, the general form of symmetry-dependent SOC takes the form of spin-dependent hopping between lattice sites

$$H_{\text{SOC}} = \sum_{i,j,\alpha,\beta} c_{i,\alpha}^{\dagger} \left(\boldsymbol{\omega}(\mathbf{p}) \cdot \boldsymbol{\sigma} \right)_{\alpha,\beta} c_{j,\beta}. \tag{3.51}$$

The type of spin-orbit coupling that occurs is specified by the vector $\boldsymbol{\omega}(\mathbf{p})$, which is constrained by the symmetry properties of the system and acts like a momentum-dependent magnetic field. For Rashba and linear Dresselhaus SOC, we have

$$\begin{aligned}
\boldsymbol{\omega}_{\text{R}} &= \lambda_{\text{R}} \left(p_y, -p_x, 0 \right), \\
\boldsymbol{\omega}_{\text{D}} &= \lambda_{\text{D}} \left(p_x, -p_y, 0 \right),
\end{aligned} \tag{3.52}$$

respectively. Here, $\lambda_{\text{R(D)}}$ denotes the strength of the Rashba (Dresselhaus) SOC. In Fig. 3.5, we compare the texture of the momentum-dependent magnetic fields for Rashba and Dresselhaus SOC.

Singlet and triplet pairing

In section 3.2, we discuss BCS theory and define the superconducting gap via the mean-field parameter $F_{\downarrow\uparrow}(\mathbf{k}) = \langle c_{-\mathbf{k}\downarrow} c_{\mathbf{k}\uparrow} \rangle$. This gives a spin singlet Cooper pair with zero centre of mass momentum. One can easily generalize to both $\mathbf{k}$- and spin-dependent pairing states $F_{\alpha\beta}(\mathbf{k}) = \langle c_{-\mathbf{k}\alpha} c_{\mathbf{k}\beta} \rangle$ [134]. The general superconducting gap is then defined by

$$\Delta_{\alpha\beta}^{*}(\mathbf{k}) = \sum_{\mathbf{q}\gamma\delta} V_{\alpha\beta\gamma\delta}(\mathbf{k}, \mathbf{q}) \langle c_{-\mathbf{q}\gamma} c_{\mathbf{q}\delta} \rangle. \tag{3.53}$$

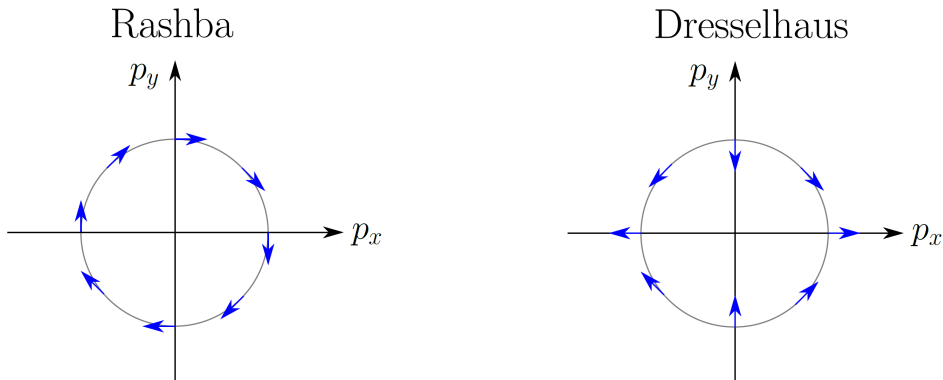**Figure 3.5.** A comparison of the effective momentum-dependent magnetic fields $\boldsymbol{\omega}_\mathrm{R}$ and $\boldsymbol{\omega}_\mathrm{D}$ for Rashba and Dresselhaus SOC, respectively.

The Pauli principle enforces the symmetry requirement $F_{\alpha\beta}(\mathbf{k}) = -F_{\beta\alpha}(-\mathbf{k})$, which again constrains the form of the superconducting gap $\Delta_{\alpha\beta}(\mathbf{k}) = -\Delta_{\beta\alpha}(-\mathbf{k})$. The matrix structure of the superconducting gap then becomes

$$\begin{bmatrix} \Delta_{\uparrow\uparrow}(\mathbf{k}) & \Delta_{\uparrow\downarrow}(\mathbf{k}) \\ \Delta_{\downarrow\uparrow}(\mathbf{k}) & \Delta_{\downarrow\downarrow}(\mathbf{k}) \end{bmatrix} = i\left(\Delta_{\mathbf{k}}I + \mathbf{d}_{\mathbf{k}}\cdot\boldsymbol{\sigma}\right)\sigma_y. \tag{3.54}$$

This structure allows either singlet pairing or triplet pairing with a complex order parameter $\Delta_{\mathbf{k}} = \Delta_{-\mathbf{k}}$ or a vector order parameter $\boldsymbol{d}_{\mathbf{k}} = -\boldsymbol{d}_{-\mathbf{k}}$, respectively.

For singlet pairing, some common choices of the symmetry of the superconducting gap are either the isotropic s-wave or anisotropic d-wave of the form

$$\Delta_{\mathbf{k}} = \begin{cases} \Delta, & s\text{-wave,} \\ \Delta\left(k_x^2 - k_y^2\right)/k_\mathrm{F}^2, & d_{x^2-y^2}\text{-wave,} \\ \Delta\left(2k_x k_y\right)/k_\mathrm{F}^2, & d_{xy}\text{-wave,} \end{cases} \tag{3.55}$$

where $\Delta > 0$ is a constant. For triplet pairing, the more exotic anisotropic p-wave symmetry is possible. We decompose $\mathbf{d}_{\mathbf{k}} = d(\mathbf{k})\hat{d}$, where $d(\mathbf{k})$ is a momentum-dependent scalar and $\hat{d}$ is a unit vector in spin space. The p-wave symmetry can then be represented as

$$d(\mathbf{k}) = \begin{cases} \Delta k_x/k_\mathrm{F}, & p_x\text{-wave,} \\ \Delta k_y/k_\mathrm{F}, & p_y\text{-wave.} \end{cases} \tag{3.56}$$

Underlying lattice

The lattice on which the Hamiltonian (3.36) is embedded is important for the description in the continuum limit. An elegant example is given by considering the

nearest neighbor hopping Hamiltonian

$$H_t = -t \sum_{\langle ij \rangle} \left(c_i^\dagger c_j + \text{h.c.} \right) \tag{3.57}$$

embedded first on a square lattice and then on a hexagonal lattice.

For the square lattice, the dispersion reaches its minimum value at the centre of the Brillouin zone (Γ-point), and the structure factor in the continuum approximation becomes

$$\gamma_{\mathbf{k}=\Gamma} \approx -\frac{\hbar^2}{2m} \mathbf{k}^2. \tag{3.58}$$

Particles embedded on the square lattice hence exhibit dynamics governed by the Schrödinger equation. On the other hand, the dispersion for the hexagonal lattice reaches its minimum value at the corners of the Brillouin zone (K-points). Only two of these points are inequivalent; we denote them K and K'. Close to these two inequivalent points, the structure factor takes the form

$$\begin{aligned} \gamma_{\mathbf{k}=K} &\approx \hbar v_{\text{F}} \left(k_x + i k_y \right), \\ \gamma_{\mathbf{k}=K'} &\approx \hbar v_{\text{F}} \left(k_x - i k_y \right), \end{aligned} \tag{3.59}$$

in the continuum approximation. Hence, the low-energy dynamics of hexagonal lattices are described by the Dirac equation with Fermi velocity $v_{\text{F}} = 3at/2\hbar$. These Dirac-like dynamics have been intensively researched since the experimental discovery of graphene [135, 136]. In Fig. 3.6, we plot the dispersion of the square lattice and the hexagonal lattice as well as their Brillouin zones to highlight their differences.
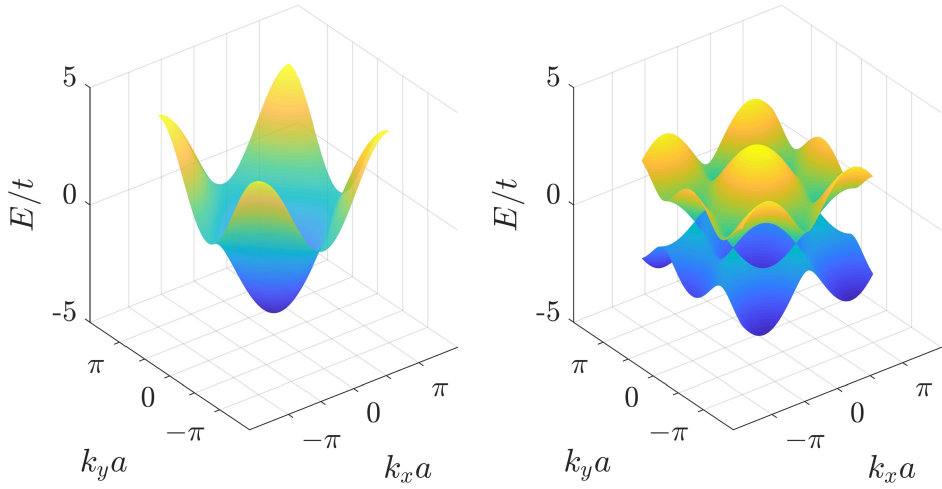
(a) The tight-binding dispersion relation for the square (left) and hexagonal (right) lattices.
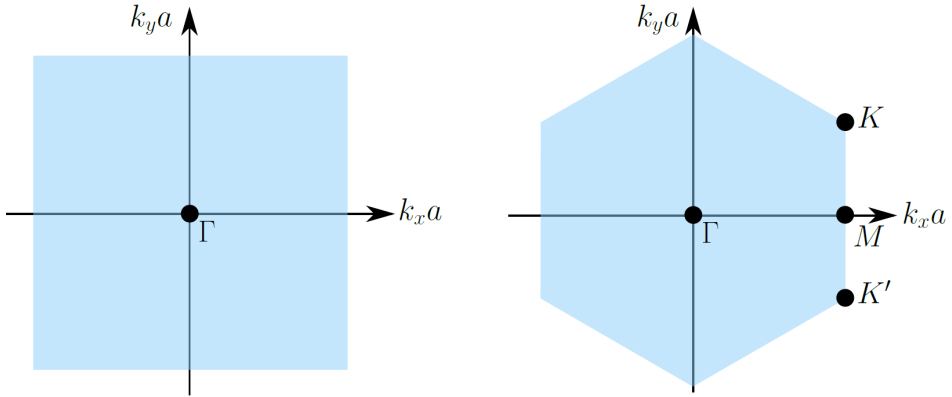
(b) The first Brillouin zone for the square (left) and hexagonal (right) lattices.

Figure 3.6. The dispersion and first Brillouin zone for the tight-binding model embedded on square (left) and hexagonal (right) lattices.

4

Scattering theory

In the research papers accompanying this thesis, we describe transport through magnetic insulators and superconducting heterostructures. The previous chapters introduce each component individually. In this chapter, we present a scattering matrix formalism that allows us to describe transport through heterostructures composed of these components. Depending on the context, the scattering matrix framework is given different names, with slight variations in technical details, yet the formulations are equivalent.

4.1 The scattering matrix formalism

Let us first discuss the general idea behind the scattering matrix, often alternatively referred to as the Landauer-Büttiker [137–143], formalism in mesoscopic systems [144–148]. The system under consideration is shown in Fig. 4.1. We consider two leads attached to a mesoscopic sample (also called the scattering region), whose transport properties are of interest. Each lead is in thermal equilibrium with and attached to a reservoir that is large compared to the mesoscopic sample. Consequently, the mesoscopic sample can be treated as a perturbation, and the reservoirs can be described in terms of an equilibrium state characterized by the chemical po-

tentials μ_L and μ_R and the temperatures T_L and T_R, respectively. The subscripts L and R refer to the left and right reservoirs, respectively. In each reservoir, the electron distribution is therefore given by the Fermi-Dirac statistics

$$f_\alpha = \frac{1}{1 + e^{\frac{E - \mu_\alpha}{k_B T_\alpha}}}, \quad \text{with} \quad \alpha = L, R. \tag{4.1}$$

A charge current can be induced and propagate through the system by then applying a voltage bias $V = (\mu_L - \mu_R)/e$ between the two reservoirs, where e denotes the electron charge. The goal is then to determine the transport properties, such as the average current, conductance, and current fluctuations, as a function of the voltage bias V or other typical parameters characterizing the mesoscopic sample. For brevity and simplicity, in the following discussion, we restrict ourselves to spinless fermions with normal metal leads. The scattering matrix formalism can of course be straightforwardly extended to more general situations, including different types and numbers of leads and heat-, thermoelectric-, and spin-transport.
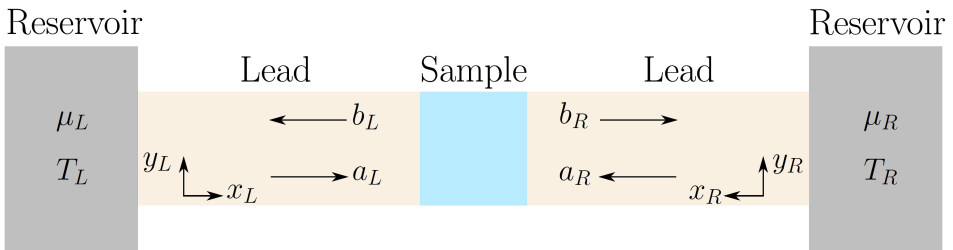

Figure 4.1. A setup for a two-lead scattering problem. Each reservoir is character-ized by a chemical potential $\mu_{L,R}$ and temperature $T_{L,R}$. In each lead, there is a local coordinate system $(x_{L,R}, y_{L,R})$ and local scattering operators for incoming $a_{L,R}$ and outgoing $b_{L,R}$ modes.

In each lead, we introduce a coordinate system (x_α, y_α) such that the positive x_α-direction always points towards the scattering region. In general, the wavefunc-tion in the scattering region is very complicated, but the wavefunction in the leads is very simple. The wavefunction in a normal metal lead is the sum of left- and right-moving plane waves and takes the form

$$\psi_\alpha(\mathbf{r}, t) = \frac{1}{\sqrt{2\pi}} \int \frac{dE}{\sqrt{\hbar v_\alpha}} e^{-i\frac{E}{\hbar}t} \left(a_\alpha(E) e^{ik_\alpha x_\alpha} + b_\alpha(E) e^{-ik_\alpha x_\alpha} \right) \phi_\alpha. \tag{4.2}$$

Here, α is the lead index, and $\phi_\alpha(y_\alpha, z_\alpha)$ are the orthonormal transversal wavefunc-tions. The energy and velocity of the propagating mode are denoted by E and

v_α, respectively. We also introduce fermionic annihilation operators describing the incoming (a_α) and outgoing (b_α) modes; see Fig. 4.1.

The charge current operator in the normal metal lead α is given by

$$I_\alpha(\mathbf{r}, t) = \frac{i\hbar e}{2m} \int \mathrm{d}y_\alpha \mathrm{d}z_\alpha \left(\frac{\partial \psi_\alpha^\dagger}{\partial x} \psi_\alpha - \psi_\alpha^\dagger \frac{\partial \psi_\alpha}{\partial x} \right). \tag{4.3}$$

To simplify the following discussion, we assume that the relevant energies, with the dominant contribution to physical properties, are those in a narrow range around the Fermi energy. By then substituting Eq. (4.2) into Eq. (4.3) and linearizing around the Fermi energy, we obtain the current operator in the lead α as

$$I_\alpha(t) = \frac{e}{h} \int \mathrm{d}E \, \mathrm{d}E' e^{i\frac{E-E'}{\hbar}t} \left(b_\alpha^\dagger(E) b_\alpha(E') - a_\alpha^\dagger(E) a_\alpha(E') \right). \tag{4.4}$$

To evaluate the physically observable charge current, we need to perform quantum-statistical averaging over the state of the incoming electrons, denoted by $\langle \cdot \rangle$. If we assume that the electrons originating at different reservoirs are uncorrelated, we can write

$$\langle a_\alpha^\dagger(E) a_\beta(E') \rangle = \delta_{\alpha\beta} \delta(E - E') f_\alpha(E) \tag{4.5}$$

for the incoming electrons. The average over the outgoing electrons is not straightforward because the particles can have originated from any reservoir by a corresponding reflection and/or transmission process in the scattering region. To proceed, we therefore introduce the unitary scattering matrix relating incoming and outgoing particles through the relation

$$b_\alpha = \sum_\beta S_{\alpha\beta} a_\beta. \tag{4.6}$$

Utilizing Eq. (4.6), the average current takes the form [140, 141]

$$\langle I_\alpha \rangle = \frac{e}{h} \int \mathrm{d}E \sum_\beta |S_{\alpha\beta}|^2 \left(f_\beta(E) - f_\alpha(E) \right). \tag{4.7}$$

Generally, the current flowing in lead α is driven by the difference in the distribution functions multiplied by the corresponding scattering matrix element modulus. If all the reservoirs have identical chemical potentials and temperatures, then the current is zero.

4.1.1 Linear response

From Eq. (4.7), we observe that a current can be caused by either a difference in chemical potential or a difference in temperature. The corresponding differential

conductance can be calculated by taking the appropriate derivative. However, to obtain simple analytical expressions, the linear response regime, where we assume small voltage or temperature biases, is useful. For completeness, we now consider first a finite voltage bias and then a finite temperature bias.

Voltage bias

We assume that between the reservoirs, there is zero temperature bias and a finite voltage bias such that

$$\mu_\alpha = \mu_0 + eV_\alpha,$$
$$T_\alpha = T_0. \tag{4.8}$$

In the linear response regime, we assume that the voltage bias is small such that both $eV_\alpha \ll \mu_0$ and $eV_\alpha \ll k_\mathrm{B} T_0$ are satisfied simultaneously. These assumptions allow us to expand the distribution functions as

$$f_\alpha \approx f_0 - eV_\alpha \frac{\partial f_0}{\partial E}, \tag{4.9}$$

where f_0 is the distribution function with chemical potential μ_0 and temperature T_0. Substituting Eq. (4.9) into Eq. (4.7), we obtain

$$\langle I_\alpha \rangle = \sum_\beta G_{\alpha\beta} \left(V_\beta - V_\alpha\right), \tag{4.10}$$

where we introduce the conductance matrix

$$G_{\alpha\beta} = G_0 \int \mathrm{d}E \left(-\frac{\partial f_0}{\partial E}\right) |S_{\alpha\beta}(E)|^2, \tag{4.11}$$

with the conductance quantum $G_0 = e^2/h$.

Temperature bias

A charge current driven by a temperature bias is referred to as thermoelectricity. To calculate the thermoelectric current, we assume zero voltage bias and finite temperature bias between reservoirs as follows:

$$\mu_\alpha = \mu_0,$$
$$T_\alpha = T_0 + T_\alpha. \tag{4.12}$$

In the linear response regime, we assume that $T_\alpha \ll T_0$ and perform the expansion

$$f_\alpha \approx f_0 + T_\alpha \frac{\partial f_0}{\partial T}. \tag{4.13}$$

By substituting Eq. (4.13) into Eq. (4.7), we obtain

$$I_\alpha = \sum_\beta L_{\alpha\beta} \left(T_\beta - T_\alpha \right),$$ (4.14)

where we introduce the thermoelectric conductance matrix

$$L_{\alpha\beta} = \frac{e}{h} \int dE \left(\frac{\partial f_0}{\partial T} \right) |S_{\alpha\beta}(E)|^2.$$ (4.15)

4.2 Scattering theory of spin transport in magnetic insulators

The scattering theory can also be extended to the transport of bosons, which is relevant for the study of spin-wave propagation through magnetic insulators. For bosons, the distribution function is given by the Bose-Einstein distribution

$$n_{B,\alpha} = \frac{1}{e^{\frac{E - \mu_\alpha}{k_B T}} - 1}.$$ (4.16)

A typical setup consists of an arbitrarily complicated scattering region sandwiched between two ferromagnetic leads. In a ferromagnetic lead, the Holstein-Primakoff representation in Eq. (2.6) can be utilized to define the magnon-spin density operator at site i as $N_i = \hbar a_i^\dagger a_i$. We can then obtain a continuity equation for the spin current in the lead by using the Heisenberg equation to calculate the rate of change of magnons. For a d-dimensional hypercubic lattice, we obtain

$$\frac{d}{dt} N_i + \sum_{\boldsymbol{\delta}} I_{j,j+\boldsymbol{\delta}} = 0,$$ (4.17)

where the current operator connecting site j with its nearest neighbor $j + \boldsymbol{\delta}$ is

$$I_{j,j+\boldsymbol{\delta}} = iJS\hbar^2 \left(a_j^\dagger a_{j+\boldsymbol{\delta}} - a_{j+\boldsymbol{\delta}}^\dagger a_j \right).$$ (4.18)

Note that here, we reinstate $\hbar$ such that the spin current has the appropriate dimension for the transfer of the angular momentum, $\hbar/t$. In this picture, the spin current is carried by magnons hopping from site to site in a nearest neighbor approximation. In parallel to the previous section, we can introduce the scattering matrix and obtain the thermal average with the appropriate statistics to obtain an expression for the spin current. In a one-dimensional two-lead system, the average spin current is

$$I = \frac{1}{2\pi} \int dE \, T(E) \left(n_{B,L} - n_{B,R} \right)$$ (4.19)

where $T(E)$ is the transmission probability through the scattering region and $n_{B,L(R)}$ denotes the Bose-Einstein distribution in the corresponding lead. A more detailed derivation is given in paper [1].

4.3 Scattering theory for superconducting heterostructures

To use the scattering formalism to describe transport through superconducting heterostructures, we need to incorporate the hole degrees of freedom. There are then two properties that need to be included:

- Electrons and holes carry opposite charges, so they make opposite contributions to the average current.

- Electrons and holes have different distribution functions. For electrons, the distribution function is the probability that a state with energy E is occupied, $f_{e,\alpha} = f_\alpha(E)$. For holes, the distribution function is the probability that a state with energy $-E$ is empty, $f_{h,\alpha} = 1 - f_\alpha(-E)$.

The opposite electron and hole charges can be straightforwardly implemented in the charge operator as

$$I_\alpha(\mathbf{r}, t) = \frac{i\hbar e}{2m} \int \mathrm{d}y_\alpha \mathrm{d}z_\alpha \left(\frac{\partial \boldsymbol{\Psi}_\alpha^\dagger}{\partial x} \tau_z \boldsymbol{\Psi}_\alpha - \boldsymbol{\Psi}_\alpha^\dagger \tau_z \frac{\partial \boldsymbol{\Psi}_\alpha}{\partial x} \right), \qquad (4.20)$$

where $\boldsymbol{\Psi} = (\psi_e, \psi_h)^T$ is the electron and hole operators and τ_z is a Pauli matrix in charge space. To account for the different electron and hole statistics, each lead should be split into separate electron and hole leads attached to reservoirs with the appropriate distribution functions, as shown in Fig. 4.2.
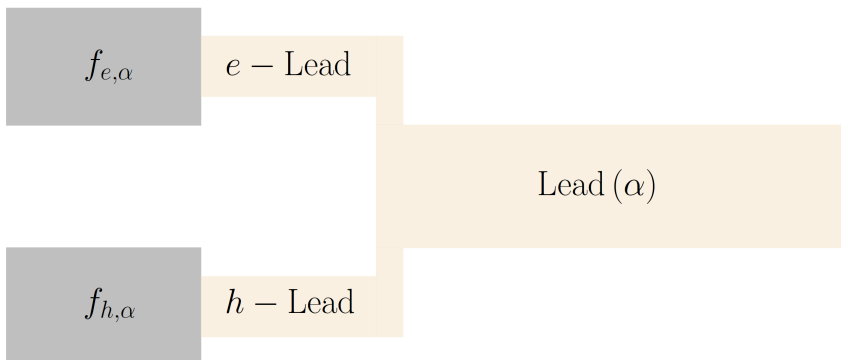

Figure 4.2. To include the hole degrees of freedom, it is convenient to split up the lead (α) into one electron lead and one hole lead, each attached to a reservoir with the appropriate statistics.

The transport properties of superconducting heterostructures were first developed by Blonder, Tinkham, and Klapwijk. In their seminal paper, they consider a superconducting bilayer, where a normal metal is connected to a superconductor and a voltage bias is applied [149]. Today, their approach is so widely recognized that the scattering matrix formalism is usually known as the Blonder-Tinkham-Klapwijk (BTK) formalism in the context of superconducting spintronics. The BTK formula for the current in a normal metal-superconductor junction is

$$I_{\text{BTK}} = \frac{2e}{h} \int \mathrm{d}E \left(1 - R_e + R_h\right) \left(f_N - f_S\right), \tag{4.21}$$

where R_e and R_h are the probabilities of electron and hole reflection, respectively, and $f_{N(S)}$ refers to the electron-distribution function in the normal metal (superconductor). The hole reflection is known as Andreev reflection and has been essential in the research papers accompanying this thesis. We introduce this concept in more detail in Chapter 6. In a variety of papers, this formula has been extended to different types and numbers of leads, higher dimensions, and heat currents [124, 150–154]. Of particular interest for the research conducted in this thesis, the BTK formula has also been generalized to the three-terminal problem, where two spatially separated leads are in contact with a common superconductor [155]. The geometry allows both theoretical and experimental studies of nonlocal transport properties. We consider the three-terminal problem in more detail in Chapter 7.

4.4 The big picture

In this chapter, we show that by considering appropriate quantum-mechanical scattering problems, we can determine the transport phenomena of, in principle, any mesoscopic system. The main idea is that the system of interest is attached, indirectly through leads, to appropriate reservoirs. The statistics of the reservoirs are specified by the particles carrying the relevant information. The transport properties of the system can be understood by considering the scattering of the information carriers. In each scattering event, a given particle can either be reflected into its original reservoir or transmitted into a new reservoir. Therefore, the problem of calculating transport properties such as the spin-, charge-, or heat-current is reduced to solving a quantum-mechanical scattering problem, with a potential profile given by the system. In general, all of the relevant transport properties are encapsulated by the scattering matrix. In crude terms, the subject of the three research papers is the determination of the scattering matrices of different systems and the calculation of

the relevant response functions. In the next three chapters, we briefly introduce each scattering problem and attempt to set them in an appropriate perspective within each scientific community.

5

Disordered magnetic insulators and Anderson localization

In this chapter, we introduce the physics necessary to understand disordered magnetic insulators, the research topic of [1]. Here, we focus on a concise introduction and refer readers to our first paper for additional details. We first give a brief overview of what a disordered magnetic insulator is, how they are usually modeled, and their role in insulating spintronics. Finally, we briefly introduce Anderson localization and discuss its relevance to our research.

5.1 Disordered magnets

In spin insulatronics, the research focus has mainly been on ideally ordered magnetic systems, where spin waves can propagate and transfer information over long distances without significant Joule heating [54]. In realistic systems, the effects of disorder are also important, as they strongly affect the transport properties of the related technologies. In general, when the disorder of a particular system is sufficiently strong, the eigenstates become trapped in a finite spatial region, completely suppressing the relevant transport properties. This behaviour is generic for all trans-

port phenomena related to electric currents, electromagnetic waves, and spin waves
and is known as Anderson localization [156, 157]. Nevertheless, the transport prop-
erties of disordered systems appear to be more subtle. Recently, an experimental
group claimed that a spin current could propagate tens of micrometers through
a sample of amorphous yttrium iron garnet without any long-range magnetic or-
der [158]. The underlying mechanism, limitations, and experimental procedure are
still intensely debated within the community [159–167]. Another class of materials
where the spin structure is strongly disordered are spin glasses [168], historically
exemplified through dilute magnetic alloys such as copper-manganese (CuMn). A
central characteristic property that distinguishes spin glasses from ordered magnets
and paramagnets is that below a characteristic "freezing" temperature, the spins are
frozen in fixed random directions. A good historical perspective on theoretical and
experimental investigations of spin glasses can be found in several popular science
papers by Anderson [169–175].

In a disordered magnetic insulator, frustration is induced, meaning that the
system has greater difficulty finding a configuration that minimizes its energy. Con-
sequently, the energy landscape exhibits many local minima, and determining the
true quantum ground state and its transport properties are challenging. In strongly
disordered systems, such as spin glasses, this energy landscape can result in noner-
godic behaviour; the system becomes trapped in a subset of the available states due
to the complex energy landscape and high energy barrier separating states. However,
there are simplified Ising-like toy models such as the random field (RF) Ising model
[176–178], the spherical model [179, 180], the Edwards-Anderson model [181], and
the Sherrington-Kirkpatrick model [182, 183] that have been studied extensively.
A drawback of these models is that the spins are treated as scalars, making them
unsuitable for describing spin-wave transport.

5.2   Disordered Heisenberg models

To describe realistic spin-wave transport in disordered systems, it is necessary to
treat the spins as three-dimensional operators, as we do in Chapter 2. Two relevant
models that we study in [1] are the RF model and the random anisotropy (RA)
model, where the disorder is modeled by a site-dependent magnetic field and a site-
dependent anisotropy term, respectively. The direction of the site-dependent field
and anisotropy is modeled by a vector $\mathbf{n}_i$ uniformly distributed on the unit sphere

and varying from site to site. The Hamiltonian is

$$H = -J \sum_{i\boldsymbol{\delta}} \mathbf{S}_i \cdot \mathbf{S}_{i+\boldsymbol{\delta}} - K \sum_i (\mathbf{n}_i \cdot \mathbf{S}_i)^{\kappa+1}, \tag{5.1}$$

where $\kappa = 0$ and $\kappa = 1$ represent the RF and RA models, respectively. The term proportional to $J > 0$ attempts to align neighboring spins in parallel, and the term proportional to $K > 0$ attempts to align each spin $\mathbf{S}_i$ with the vector $\mathbf{n}_i$. The result is a noncollinear disordered ground state, and the strength of the disorder is parameterized by the ratio K/J. Other related works [166, 184, 185] have demonstrated that the transport properties can often also effectively be investigated by considering coupled classical spins embedded on a lattice, obeying atomistic [186] Landau-Lifschitz-Gilbert equations [187–189].

5.3 Anderson localization

In [1], we use the scattering matrix formalism to study the one-dimensional propagation of a spin current through the RF and RA Heisenberg models. We use ferromagnetic leads, where the eigenstates are circularly polarized spin waves. In the magnon picture, the spin current is carried by magnons hopping from site to site. Concretely, spin disorder leads to both random hopping amplitudes and random onsite potentials, which completely breaks the translational symmetry. This allows us to physically understand the Anderson localization in a simple wavefunction picture, as shown in Fig. 5.1. There are three effects originating from the
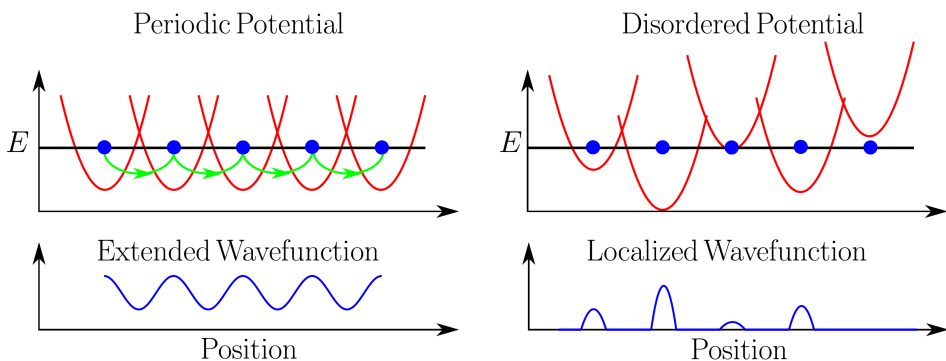

Figure 5.1. The wavefunction in a periodic potential (left) and disordered potential (right). For sufficiently strong disorder, the wavefunction becomes completely localized, a phenomenon known as Anderson localization.

effectively aperiodic disordered potential. First, each individual wavefunction is also aperiodic. Second, the individual wavefunction amplitudes generally decrease with an increasing distance from the parent lattice site. Third, the relative phases between individual wavefunctions are random. The net result is complete destructive quantum-wavefunction interference, giving a localized total wavefunction and suppressing the transport properties. Consequently, the conductance for a system of length L becomes exponentially suppressed

$$G \propto \exp\left\{-L/\tilde{L}\right\} \tag{5.2}$$

on the length scale given by the localization length $\tilde{L}$. Furthermore, we investigate the relationship between the localization length $\tilde{L}$ and the strength of disorder K/J in the RF and RA models. In the limit of weak disorder, the localization lengths obey power laws, and we calculate the relevant critical exponents. To avoid a lengthy and rather technical discussion, we refer the reader to paper [1] for additional details.

An interesting research idea that we leave for future work is to investigate how the Anderson localization of spin waves manifests in higher dimensions ($d = 2, 3$). In electronic systems, this problem has been addressed using scaling theory, and universal features have been determined [190, 191]. The scaling theory argument is applicable to electronic systems of dimensionless length l and rests on the fact that in the weakly and strongly disordered regimes, the dimensionless conductance g obeys Ohm's law $g \propto l^{d-2}$ and is exponentially suppressed $g \propto \exp(-l)$, respectively. In addition, it is assumed that the d-dimensional beta function

$$\beta_d = \frac{\mathrm{d}\ln g}{\mathrm{d}\ln l} \tag{5.3}$$

possibly connecting the conductive and localized regimes is continuous and monotonic. If the beta function is positive or negative, the system is conducting or localized, respectively. The Anderson localization for electronic systems depends on the dimension in the following way:

- In one dimension, $\beta_1 < -1$: Anderson localization occurs regardless of the disorder strength.

- Two dimensions represent the critical dimension, and $\beta_2 < 0$: Anderson localization occurs for all disorder strengths, but the beta function approaches zero in the ohmic regime.

- In three dimensions, the beta function can be both positive and negative $\beta_3 < 1$, and it has one unique fixed point $\beta_3 = 0$: There is a critical strength of

disorder where a phase transition from the localized regime to the conductive regime exists.

The aforementioned features are summarized in Fig. 5.2. We can only speculate
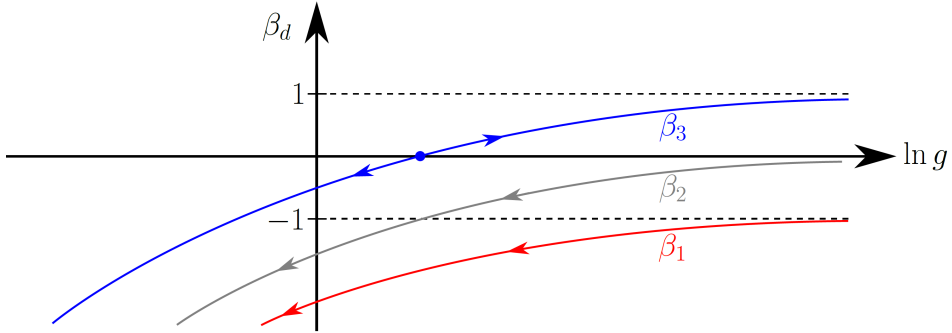

Figure 5.2. The simplest possible scaling behaviour of the beta function β_d for an electronic system in dimension d. In $d = 1, 2$ the beta function is negative and the system is localized. In $d = 3$ the beta function changes sign, and hence a phase transition from the localized to the conductive regime exists. The arrows indicate the direction of the conductance scaling flow as a function of increasing system length.

about whether scaling laws similar to the above govern the spin-wave dynamics in disordered magnets. In any case, a corresponding scaling law analysis seems to be an interesting research direction.

6

Superconducting bilayers and Andreev reflection

In this thesis, we refer to a superconducting bilayer as any structure of the form X-S, where X can in principle be any nonsuperconducting material and S is a superconductor. In this chapter, we introduce the cases most relevant to our research in [2], i.e., when X is a normal metal (N), ferromagnetic metal (F), and antiferromagnetic metal (AF). In turn, we go through each example and elucidate the main physics. The most central idea is the Andreev reflection (AR), which manifests uniquely depending on the choice of nonsuperconducting material.

6.1 Normal metal

The interface between a normal metal and a superconductor can be modeled by the Bogoliubov-de Gennes (BdG) equations, which we derived in Sec. 3.3,

$$
\begin{bmatrix} H_e - E_{\mathrm{F}} & \Delta \\ \Delta^{\dagger} & E_{\mathrm{F}} - H_h \end{bmatrix} \begin{bmatrix} \psi_e \\ \psi_h \end{bmatrix} = E \begin{bmatrix} \psi_e \\ \psi_h \end{bmatrix}. \tag{6.1}
$$

Here, $H_e = -\frac{\hbar^2}{2m}\nabla^2$ and $H_h = T H_e T^{-1} = H_e$ are the kinetic energies of electrons and holes, respectively. T is the time-reversal operator. For simplicity, we assume

that electrons and holes have the same effective mass m and that the supercon-
ducting gap is a step potential $\Delta = \Delta_0 \Theta(x)$. The superconducting gap couples the
electron ψ_e and hole ψ_h degrees of freedom in the superconductor. Since there is
only one superconductor, we choose Δ_0 to be real. The Fermi energy and excitation
energy are denoted by E_{F} and E, respectively. Experimentally, the excitation en-
ergy can be controlled by applying a bias voltage V between the normal metal and
superconductor. At zero temperature the exact relationship between bias voltage
and excitation energy is $E = eV$.

Let us comment on the step-function approximation that we utilize for the
superconducting gap. In reality, the superconducting gap has a potential profile
that changes from 0 to Δ_0 across the N-S interface on a length scale set by the
corresponding coherence lengths. Therefore, on an atomic scale, Δ is a continuous
position-dependent function. However, in bilayer structures, we are typically inter-
ested in larger mesoscopic length scales, where the N-S interface can be described
as a sharp boundary without losing essential physics [64, 147].

In the following, we also employ the Andreev approximation, which utilizes that
$E_{\mathrm{F}} \gg \Delta_0, E$. This assumption is justified in metals where E_{F} is typically on the
scale of eV, while E and Δ_0 are typically on the scale of meV. We emphasize that
we did not utilize the Andreev approximation in the research papers.

6.1.1   Retroreflective Andreev reflection

In the normal metal, the electron ($\mathbf{k}$) and hole ($\mathbf{q}$) wavenumbers are

$$\mathbf{k}^2 = \frac{2m}{\hbar^2}\left(E_{\mathrm{F}} + E\right), \quad \mathbf{q}^2 = \frac{2m}{\hbar^2}\left(E_{\mathrm{F}} - E\right), \tag{6.2}$$

respectively. The corresponding group velocities are

$$\mathbf{v}_e = \frac{\hbar^2}{m}\mathbf{k}, \quad \mathbf{v}_h = -\frac{\hbar^2}{m}\mathbf{q}. \tag{6.3}$$

Note that the orientation of the hole velocity is opposite to the orientation of the
wavenumber, a consequence of the opposite curvatures of the dispersion relations.

Let us now consider a scattering problem with an electron incident from the
metal with $E < \Delta_0$. For mathematical conciseness, we consider two dimensions, but
the generalization to three dimensions is straightforward. The incident electron can
in principle either be reflected as an electron (normal reflection (NR)) or reflected
as a hole (AR) due to electron-hole coupling in the superconductor [153, 192–194].

Therefore, the wavefunction

$$\Psi = e^{i|\mathbf{k}|(x\cos\alpha + y\sin\alpha)}\begin{bmatrix}1\\0\end{bmatrix} + r_{ee}e^{i|\mathbf{k}|(-x\cos\beta + y\sin\beta)}\begin{bmatrix}1\\0\end{bmatrix} + r_{eh}e^{i|\mathbf{q}|(x\cos\gamma + y\sin\gamma)}\begin{bmatrix}0\\1\end{bmatrix} \quad (6.4)$$

is a solution of Eq. (6.1) for $x < 0$. The angles α, β, and γ denote the angle of incidence, the angle of NR, and the angle of AR, respectively. Due to the translational invariance in the y-direction, we have

$$|\mathbf{k}|\sin\alpha = |\mathbf{k}|\sin\beta = |\mathbf{q}|\sin\gamma. \quad (6.5)$$

Utilizing the Andreev approximation, Eqs. (6.3) and (6.5) imply that electrons and holes are reflected specularly and retroreflectively, respectively. The two underlying assumptions are i) that $\Delta_0 \ll E_F$ and ii) that the electron and hole dispersions have opposite curvatures.

The physical interpretation of AR is that an electron above the Fermi sea combines with an electron below the Fermi sea to form a Cooper pair propagating in the superconductor. The process leaves a positively charged hole in the normal metal (see Fig. 6.1). Thus far, we have neglected the electron spin. In the absence of spin-orbit coupling, a reflected hole always has a spin pointing in the opposite direction of the incident electron. If this were not the case, a spin current would be generated through the application of a voltage bias to the N-S junction.
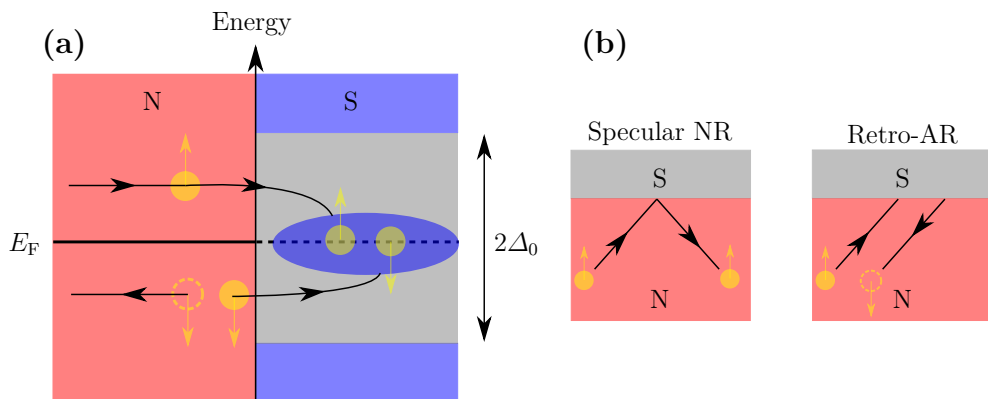

Figure 6.1. (a) An illustration of AR. An electron above the Fermi energy combines with an electron below the Fermi energy to form a Cooper pair in the superconductor. The formation of the Cooper pair can be interpreted as an incoming electron being reflected as a hole. (b) The NR is specular, while the AR is retroreflective.

6.1.2   The matching condition and local conductance

The reflection coefficients r_{ee} and r_{eh} can be determined by requiring that the wavefunction and its derivative be continuous at the interface

$$\left(\Psi - \Psi_S\right)\Big|_{x=0} = 0, \quad \frac{\mathrm{d}}{\mathrm{d}x}\left(\Psi - \Psi_S\right)\Big|_{x=0} = 0. \tag{6.6}$$

Here, Ψ and Ψ_S are the wavefunctions in the normal metal and superconductor, respectively. In Eq. (6.6), we assume a perfect interface. We can, to some extent, lift this assumption by introducing, e.g., an effective potential barrier or spin-orbit coupling at the interface, as illustrated in Sec. 3.3.1. Interface terms result in the derivative of the wavefunction picking up a discontinuity. The discontinuity is determined by the strength of the potential barrier and/or the strength of the spin-orbit coupling.

As we show in Sec. 4.3, once we know the reflection coefficients, we can compute the zero-temperature electrical conductance G by using the extended Blonder-Tinkham-Klapwijk formula [149]

$$G = G_N \int \mathrm{d}\alpha \cos\alpha \left[1 - R_{ee}\left(eV, \alpha\right) + R_{he}\left(eV, \alpha\right)\right], \tag{6.7}$$

where we average over the angle of incidence α. The reflection probabilities are $R_{ee} = |r_{ee}|^2$ and $R_{he} = |r_{he}|^2$. The Sharvin conductance G_N is defined as the conductance in the limit $\Delta_0 \to 0$ [195, 196]. Charge conservation, relating electrons, holes, and Cooper pairs, dictates that NR and AR suppress and enhance the conductance, respectively. In the absence of a potential barrier, the AR completely dominates the NR. A finite potential barrier blocks electrons from entering the superconductor. Consequently, the conductance decreases as the potential barrier becomes stronger, as shown in Fig. 6.2. Note that when the potential barrier is strong, the conductance approaches the density of states of the superconductor.
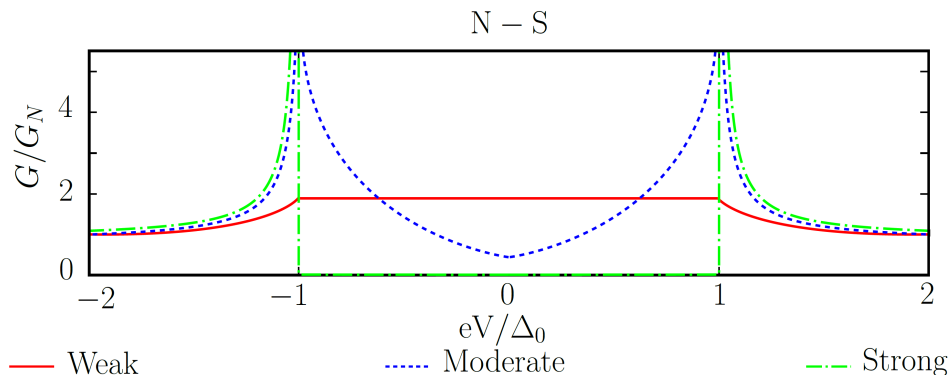
Figure 6.2. An illustration of the effect that a finite potential barrier has on the conductance of the N-S junction. The conductance G is normalized with respect to the Sharvin conductance G_N. The conductance is plotted as a function of the voltage bias eV/Δ_0. The figure shows three limiting cases, where the potential barrier is weak, moderate, and strong.
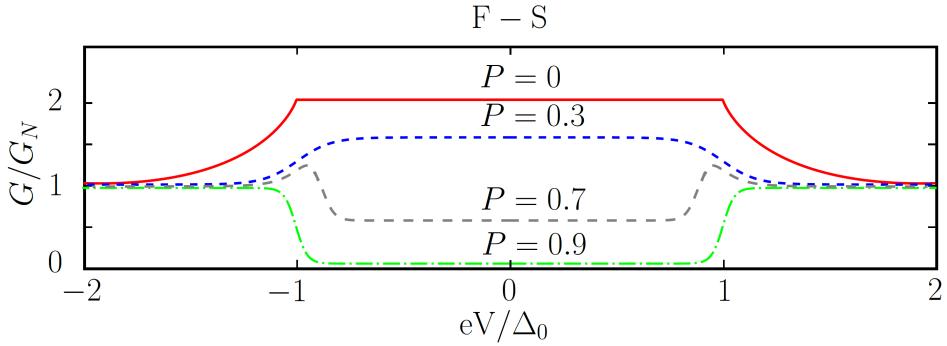
6.2 Ferromagnet

Unlike a normal metal, the energy bands in a ferromagnetic metal are not spin degenerate due to the finite exchange interaction J_{FM}. Since AR is a spin-dependent process, the conductance depends on the dimensionless exchange strength $P = J_{\mathrm{FM}}/E_{\mathrm{F}}$. More physically, we can understand this dependence by plotting the density of states for spin-up and spin-down electrons in a ferromagnet, as shown in Fig. 6.3a. To form a Cooper pair, an incoming spin-up electron must combine with a spin-down electron below the Fermi energy. For a fixed voltage, spin splitting makes Cooper pair formation impossible for a sufficiently large exchange strength. Consequently, the AR and conductance decrease with increasing exchange strength, as shown in Fig. 6.3b [150, 197–200].

Furthermore, with the introduction of spin-orbit coupling at the interface, spin is no longer conserved. Spin-orbit coupling thus allows for spin-flipped AR, where the Cooper pair forms a spin-triplet state [201–203]. Potentially, this can lead to the capability to enhance and tune the conductance of the F-S junction with an external magnetic field. However, ferromagnets also produce finite magnetic fields, making them both sensitive to stray fields and disruptive in high-density quantum applications.
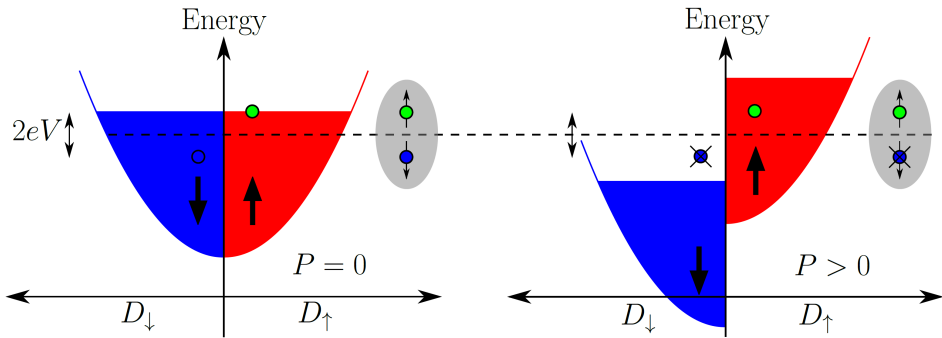
(a) A finite exchange strength $P > 0$ causes spin splitting in the density of states $D_{\uparrow,\downarrow}$. Consequently, for certain voltages, an incident electron with spin s cannot find a partner with spin $-s$ to form a Cooper pair. The dashed horizontal line is the Fermi energy.

**(b)** An increasing exchange strength P leads to a decreasing conductance because AR gradually becomes suppressed.

Figure 6.3.   The density of states **(a)** and conductance **(b)** as a function of the ferromagnetic exchange strength.

6.3 Antiferromagnet

To eliminate the problems caused by the finite net magnetizations of ferromagnets, it is natural to consider what happens if a ferromagnet is replaced by an antiferromagnet. In a series of theoretical papers, [204–207], it is shown that an antiferromagnet allows two unusual scattering processes: i) retro-NR and ii) specular AR. In Josephson junctions, antiferromagnetism theoretically causes low-energy bound states that lead to anomalous phase shifts and atomic-scale $0 - \pi$ transitions. The existence of supercurrents in S-AF-S junctions has been experimentally reported [208, 209], yet other theoretical predictions are relatively unexplored. In the second paper [2] complementing this thesis, we investigated possible experimental signatures in the electrical and thermal conductance of the AF-S bilayer.

An antiferromagnetic dispersion, with band gap $2J_{\mathrm{AFM}}$, is sketched in Fig. 6.4a. The antiferromagnetic exchange interaction produces a curvature in the dispersion that allows both specular and retroreflective NR and AR to occur. As the exchange interaction J_{AFM} or voltage bias eV increases, the probability of both types of AR decreases. Conservation of probability then dictates that both types of NR must increase. In agreement with previous literature, an explicit calculation confirms that for a transparent interface, the antiferromagnetic interactions favor retroreflective NR over specular NR. As the transparency of the interface decreases, both retroreflective and specular NR eventually contribute equally. The net result of these competitions among the various scattering processes is encapsulated in the electrical conductance, as shown in Fig. 6.4b

Although the underlying physics is fundamentally different, the conductance of the AF-S junction behaves similarly to that of the F-S junction as a function of the voltage bias. From the application point of view, the important characteristic of antiferromagnets is the complete lack of stray field production and coupling. In some instances, antiferromagnets may therefore act as a suitable replacement for ferromagnets in high-density quantum technology applications at the nanoscale.
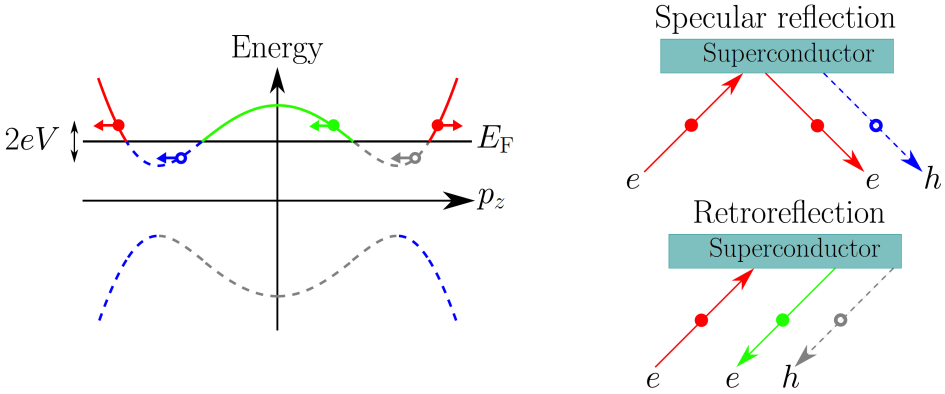
(a) The antiferromagnetic dispersion (left) and possible scattering processes (right) at the AF-S bilayer junction. The colors give the correspondence between scattering processes and the dispersion branch, and p_z denotes the component of the wavenumber that is orthogonal to the interface.
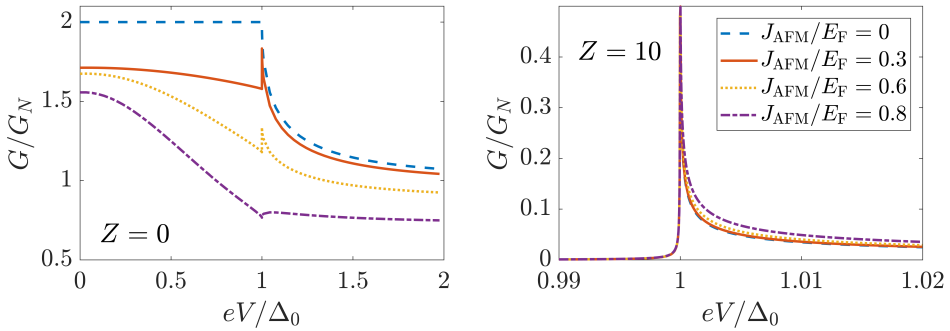
(b) The electrical conductance as a function of the voltage bias and antiferromagnetic exchange strength for transparent (left) and nontransparent (right) interfaces.

Figure 6.4. **(a)** The antiferromagnetic dispersion with possible scattering processes at the AF-S bilayer, and **(b)** the corresponding electrical conductance.

6.4 PCAR spectroscopy - experimental proposal

AR is frequently utilized in an experimental technique called point contact Andreev reflection (PCAR) spectroscopy [125, 126, 197, 210, 211]. Typically, a voltage biased metallic or ferromagnetic tip is placed in contact with a single superconductor. The controllable voltage bias induces a measurable current with both electron and hole contributions. Consequently, PCAR spectroscopy allows the determination of the current-voltage characteristics. In superconducting spintronics, PCAR spectroscopy is commonly used to determine the spin polarization of a ferromagnet or the temperature dependence and symmetry of the superconducting gap [212–214]. An important milestone is the measurement of the zero-bias conductance peak in high-temperature superconducting cuprates such as $YBa_2Cu_3O_7$ [215–217]. The existence of the zero-bias conductance peak is often attributed to the fact that high-temperature cuprates may exhibit d-wave pairing symmetry [218–222].
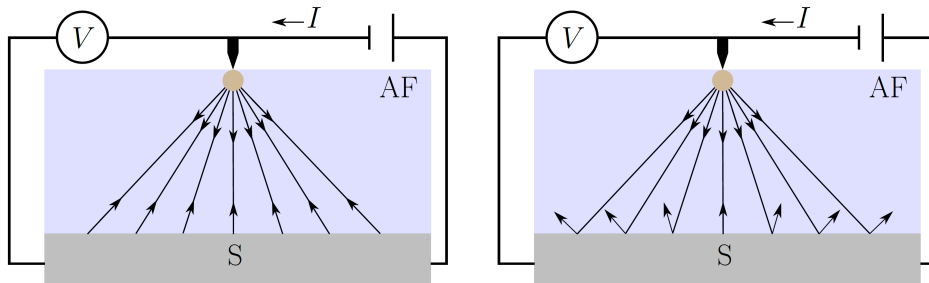
Figure 6.5. A proposed setup for measuring the contribution of retroreflective scattering processes to the conductance. A voltage-biased point contact is attached to an AF-S junction, forming a focused measuring point (beige) for the induced current I. The left and right figures demonstrate that the contributions to the conductance from the retroreflective and specular reflection processes are enhanced and suppressed, respectively.

The total conductance of N-S, F-S, and AF-S junctions can be measured straightforwardly by coupling the junctions to reservoirs, but it is then difficult to distinguish between specular and retroreflective processes. This is an issue that we did not address in our paper [2] on retroreflective NR in AF-S junctions. Here, we propose an experimental setup in which it is possible to distinguish between specular and retroreflective scattering processes that may be useful in the investigation of the AF-S junctions. The setup we propose has been used in an experiment where the goal was to separate the contribution to the total conductance from the

retroreflective AR and specular NR in N-S junctions [223]. The experimental proposal is shown in Fig. 6.5. By attaching a point contact to an AF-S junction, we can create a focus point for incoming electrons. We measure the conductance at the same focus point. As shown in the figure, the dominant contribution to the measured conductance consists primarily of retroreflective NR and AR as the specular processes become dispersed. Distinguishing whether the electrons or holes dominate for a finite exchange interaction can in principle be done by subtracting the Sharvin conductance and checking whether the measured conductance is positive or negative. We hope that this proposal may be useful to experimentalists wanting to test our predictions.

7

Superconducting trilayers and crossed Andreev reflection

The final research topic that we consider in our research is related to the nonlocal transport properties in X-S-X trilayers. Here, X can be any conducting material, and S is a superconductor. In this chapter, we briefly introduce some of the relevant physics. Concretely, we focus on the nonlocal Andreev reflection between the two leads. The central issue is designing a system that allows successful experimental detection of this nonlocal process. The reciprocal process, where a Cooper pair is split into its two constituent electrons, is considered a natural source for generating entangled particles that may be useful in quantum computing, communication, and cryptography technology. The goal of this chapter is to motivate the research performed in [3] and to put our main findings into perspective.

7.1   Nonlocal experimental signature

In this section, we consider the X-S-X geometry shown in Fig. 7.1. The lower and upper leads are referred to as lead 0 and lead 1, respectively. The relevant experimental setup is obtained by keeping lead 0 at a finite voltage V and grounding both

the superconductor and lead 1. This geometry induces local and nonlocal conductance in lead 0 and lead 1, respectively. The local and nonlocal conductances can be measured separately by probing the appropriate lead. To calculate the conductances, we can use the scattering matrix approach discussed in Chapters 4 and 6.
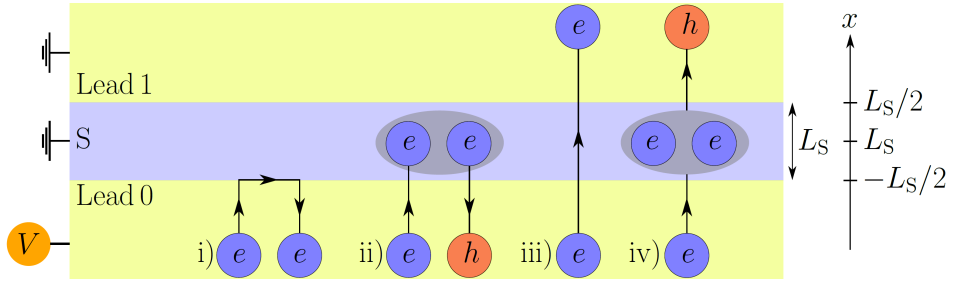

Figure 7.1. The possible scattering processes in the X-S-X trilayer system are i) local NR, ii) local AR, iii) nonlocal CT, and iv) nonlocal CAR. We assume that lead 0 is voltage biased, while the superconductor and lead 1 are grounded. The voltage bias V induces local and nonlocal currents in lead 0 and lead 1, respectively. The local (nonlocal) current is determined by competition between NR and AR (CT and CAR).

In the relevant scattering problem, an electron is incident from lead 0, and there are four possible scattering processes:

i) Local normal reflection (NR), where the incident electron is reflected back into lead 0.

ii) Local AR, where the incident electron is reflected as a hole into lead 0.

iii) Nonlocal electron cotunnelling (CT), where the incident electron is transmitted into lead 1.

iv) Nonlocal crossed Andreev reflection (CAR), where the incident electron is transmitted as a hole into lead 1.

We assume that the excitation energy eV is smaller than the superconducting gap Δ_0, so both AR and CAR can be clearly associated with Cooper pair formation in the superconductor. In the regime $eV > \Delta_0$, AR and CAR can also result from the propagation of electron-like and hole-like quasiparticles in the superconductor.

Since electrons and holes carry opposite charges, their contributions are opposite in the conductance. Generally, the local G_L and nonlocal G_{NL} conductance can be expressed as

$$G_L = G_0 - G_{NR} + G_{AR}, \quad \text{and} \quad G_{NL} = G_{CT} - G_{CAR}. \tag{7.1}$$

Here, G_0, G_{NR}, G_{AR}, G_{CT}, and G_{CAR} are the contributions to the conductance from the incident electrons, local NR, local AR, nonlocal CT, and nonlocal CAR. Importantly, we note that if CAR dominates CT, then the nonlocal conductance is negative. The sign of nonlocal conductance is a direct experimental signature of CAR-dominant transport. Unfortunately, the CAR process is delicate and is often masked by more robust competing scattering processes. Of special significance is the CT process because it makes a direct contribution to the nonlocal conductance in the same lead as CAR. NR and AR are somewhat less important because their direct contribution goes to the biased lead. In any case, to unambiguously detect CAR, the optimal solution is to design a geometry where CAR is enhanced and the competing scattering processes are suppressed. Additionally, to measure a finite nonlocal conductance, the width of the superconductor L_S must be close to or smaller than the superconducting coherence length ξ. For larger L_S, the nonlocal conductance becomes exponentially suppressed. In the limit $L_S \to \infty$, the local conductance of the X-S-X trilayer becomes identical to the conductance of the X-S bilayer, a useful consistency check.

7.2 Unmasking the crossed Andreev reflection

Numerous superconducting heterostructures of the form X-S-X have been theoretically proposed to enhance CAR signals. Some well-known choices for X are normal metals (N) [224–227], ferromagnetic metals (F) [155, 228–231], two-dimensional graphene (G) [232, 233], and topological insulators [234–239]. The experimental detection of CAR and the simultaneous preservation of the entanglement in the corresponding Cooper pair splitting process remain challenging issues. However, there has been successful experimental detection in both N-S-N [240–245] and F-S-F [246–250] junctions. Furthermore, enhanced CAR signals have been detected when quantum dots were utilized [251–257]. Very recently, the experimental detection of CAR utilizing oppositely doped graphene-based leads has been fruitful [258, 259].

Nevertheless, current state-of-the-art theoretical and experimental proposals require incredibly precise fine-tuning of the electronic structure and bias voltage,

which may limit their technological applications. Additionally, utilizing ferromagnets may destroy the entanglement between quantum spins. We elaborate on this issue in Sec. 7.2.3. One especially important parameter in the fine tuning in the aforementioned experiments is the local Fermi energy in each lead. This motivates utilizing two-dimensional systems where the local Fermi energy can be tuned by applying appropriate gate voltages to the leads. In the following, we briefly discuss the G-S-G, F-S-F, and AF-S-AF junctions embedded on a two-dimensional hexagonal lattice, which is the subject of [3]. To keep our discussion general, we discuss a model that is applicable to systems in which ferromagnetism, antiferromagnetism, and superconductivity are either intrinsic to the materials or induced by proximity.

7.2.1   Model

For materials with hexagonal lattices, the equation of motion governing electrons (e) and holes (h) is the 2D Dirac-Bogoliubov-de Gennes (DBdG) equation,

$$\begin{bmatrix} H_e + H_{s\text{-}d}(x) - E_{\mathrm{F}}(x) & \Delta(x) \\ \Delta^*(x) & H_h - H_{s\text{-}d}^T(x) + E_{\mathrm{F}}(x) \end{bmatrix} \Psi(x) = E\Psi(x). \qquad (7.2)$$

Here, $E_{\mathrm{F}}(x)$ is the local Fermi energy, which is experimentally controllable by a gate voltage, and T is the transpose operator. For convenience, we introduce the Pauli matrices $\boldsymbol{s}$ and $\boldsymbol{\sigma}$ in spin- and sublattice-space, respectively.

The kinetic term governing the free dynamics of the electrons and holes associated with the K-point is

$$H_{e(h)} = \pm v_{\mathrm{F}}\, \mathbf{p} \cdot \boldsymbol{\sigma}. \qquad (7.3)$$

The possible magnetic s-d exchange interactions where the stationary spins have order parameter $\mathbf{m}(x)$ are

$$H_{s\text{-}d} = J(x)\left(\mathbf{m}(x) \cdot \boldsymbol{s}\right) \otimes \begin{cases} \sigma_0, & \text{Ferromagnet,} \\ \sigma_z, & \text{Antiferromagnet.} \end{cases} \qquad (7.4)$$

The mean-field superconducting gap coupling electrons and holes is given by

$$\tilde{\Delta}(x) = is_y \otimes \Delta(x)\sigma_0. \qquad (7.5)$$

The approximate size of the Cooper pairs is given by the superconducting coherence length $\xi = \hbar v_{\mathrm{F}}/\Delta$. To ensure that the mean-field requirement of superconductivity is satisfied, we assume that the Fermi energy in the superconductor is much larger than the superconducting gap.

For simplicity, we neglect the possible coexistence of magnetism and superconductivity close to the interfaces and assume step-function behavior

$$\{J(x), E_{\mathrm{F}}(x), \Delta(x)\} = \begin{cases} \{J, E_{\mathrm{F}0}, 0\}, & x < -\frac{L_{\mathrm{S}}}{2}, \\ \{0, E_{\mathrm{FS}}, \Delta_0\}, & -\frac{L_{\mathrm{S}}}{2} < x < \frac{L_{\mathrm{S}}}{2}, \\ \{J, E_{\mathrm{F}1}, 0\}, & x > \frac{L_{\mathrm{S}}}{2}. \end{cases} \qquad (7.6)$$

Here, we introduced the constants $\{J, E_{\mathrm{F}j}, E_{\mathrm{FS}}, \Delta_0\}$ and the subindex $j = \{0,1\}$, which labels the lead. To justify the step-function behaviour of $\Delta(x)$ and $J(x)$, we assume that $E_{\mathrm{FS}} \gg E_{\mathrm{F}j}$. This requirement is equivalent to the Fermi wavelength in the leads being much larger than the Fermi wavelength in the superconductor, giving a large Fermi wavelength mismatch [154, 260]. In any case, we expect a realistic spatial profile of the order parameters to result in only minor perturbative quantitative changes to the nonlocal conductance.

To determine the local and nonlocal conductances, we consider a scattering problem with incident electrons from lead 0. We then write the solution of the DBdG equation in lead 0, the superconductor, and lead 1 and match the wavefunctions at the interfaces. Concretely, we find the matching condition

$$i \begin{bmatrix} s_0 \otimes \sigma_x & 0 \\ 0 & -s_0 \otimes \sigma_x \end{bmatrix} \left[\psi(x_0^+) - \psi(x_0^-) \right] =$$

$$Z_V \begin{bmatrix} s_0 \otimes \sigma_0 & 0 \\ 0 & -s_0 \otimes \sigma_0 \end{bmatrix} \psi(x_0) + \frac{Z_h}{2} \begin{bmatrix} (\mathbf{m} \cdot \mathbf{s}) \otimes (\sigma_0 + \sigma_z) & 0 \\ 0 & -[(\mathbf{m} \cdot \mathbf{s}) \otimes (\sigma_0 + \sigma_z)]^T \end{bmatrix} \psi(x_0)$$

$$(7.7)$$

for the total wavefunction $\psi(x)$, with an interface located at the position $x = x_0$. Here, $Z_V = V/\hbar v_{\mathrm{F}}$ and $Z_h = h/\hbar v_{\mathrm{F}}$ represent a potential barrier with strength V and a potentially uncompensated magnetization h. In the following, we assume a perfect interface with $Z_V = Z_h = 0$. We discuss interface effects in the supplemental material of [3].

7.2.2 Graphene

To model the G-S-G junction where the leads are nonmagnetic graphene, we set the s-d exchange interaction $H_{s\text{-}d}$ to zero. To detect a CAR signal, it was theoretically proposed to electron dope lead 0 and hole dope lead 1 by using a gate voltage [232]; the corresponding dispersion is shown in Fig. 7.2. At the Dirac points, the density of states is zero. Consequently, if the bias voltage is tuned to exactly coincide with the local Fermi energy, both AR and CT are blocked in favor of CAR, as sketched

in Fig. 7.2. The dominant CAR signal leads to a resonant negative signal when $eV = E_F < \Delta_0$ in the nonlocal conductance, as shown in Fig. 7.2.
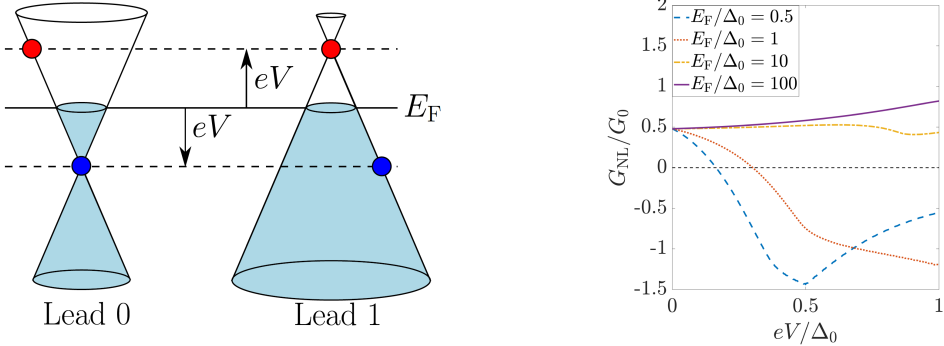

Figure 7.2. Left: The possible scattering processes in a G-S-G junction. The left and right graphene layers are electron- and hole-doped, respectively. Note that when $eV = E_F < \Delta_0$, only CAR is possible in lead 1. Right: The resulting nonlocal conductance as a function of the voltage bias and different gate-controllable local Fermi energies.

Experimentally, it has been challenging to measure a CAR-dominant signal in the G-S-G junction because of spatial fluctuations in the gate-controlled local Fermi energy δE_F, often referred to as electron-hole puddles. In monolayer graphene, the local fluctuations are $\delta E_F \approx 30\,\text{meV}$ [261] or $\delta E_F \approx 5.5\,\text{meV}$ [262] when grown on silicon oxide (SiO_2) or hexagonal boron nitride (h-BN), respectively. The fluctuations δE_F usually exceed the value of the superconducting gap, of which a typical value is $\Delta_0 \approx 1.1\,\text{meV}$ in, e.g., niobium (Nb). Only recently has this problem been circumvented by utilizing bilayer graphene instead of monolayer graphene [259] and in a four-terminal geometry [258]. In addition to the fluctuations in δE_F, a drawback of the G-S-G junction is that the CAR-dominant signal is guaranteed only at the specific voltage $eV = E_F$.

7.2.3   Ferromagnets

In an F-S-F junction, it has been theoretically shown that a CAR-dominant voltage is possible for all voltages $eV < \Delta_0$ [228, 263]. CAR dominates when the two ferromagnetic magnetizations are antiparallel $\mathbf{m}_0 = -\mathbf{m}_1$ and the band structure is tuned so that the density of states of minority spins is negligible compared to majority spins. Specifically, the conditions $J_{FM} = E_F$ and $J_{FM} \gg \Delta_0 > eV$ must be

satisfied to obtain a negative nonlocal conductance where CT and AR are suppressed in favor of CAR. Figure 7.3 shows the lead dispersions and nonlocal conductance in the CAR-dominant regime for an F-S-F junction.
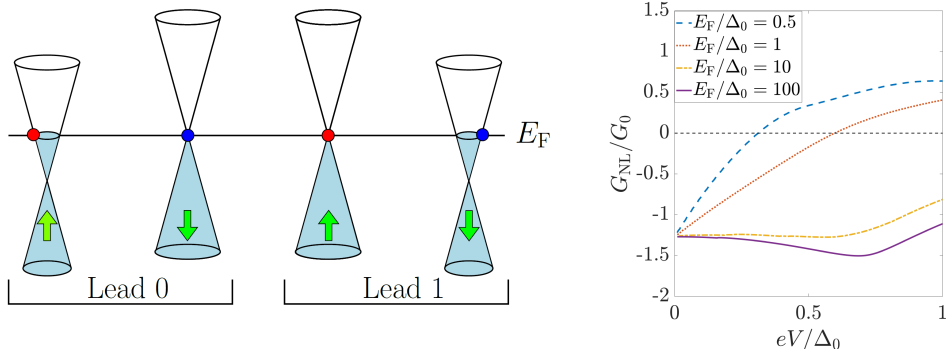

Figure 7.3. Left: The possible scattering processes in a hexagonal F-S-F junction when the magnetizations in lead 0 and lead 1 are antiparallel and the bias voltage is low $eV \ll E_\mathrm{F}$. Right: The resulting nonlocal conductance in lead 1. Completely dominant CAR is possible only when $eV < \Delta_0 \ll E_\mathrm{F}$; when the inequality is violated, CAR competes with CT.

However, utilizing ferromagnets may be unwanted, but not just because of their coupling and production of stray fields. The CAR-dominant signal in an F-S-F junction rests on the suppressed density of states of minority and majority spins in leads 0 and 1, respectively. Effectively, this locks the spin orientation of the charge carriers, which in turn destroys their quantum entanglement [228, 233]. Nevertheless, the F-S-F junction exhibits an experimentally realizable and controllable local and nonlocal magnetoresistance that may have technological applications.

7.2.4　Antiferromagnets

To avoid the destruction of quantum entanglement and simultaneously obtain an experimentally detectable CAR signal, the utilization of leads where the density of states is spin degenerate is promising. Prominent candidates, with a large number of possible experimental realizations, are two-dimensional, two-sublattice, and collinear antiferromagnets. In paper [3], we investigate the possibility of CAR-dominant transport in an AF-S-AF junction. The antiferromagnetic exchange interaction induces a gap in the leads. The antiferromagnetic gap allows the possibility of completely suppressing AR and CT in favor of CAR by electron doping lead 0 and

hole doping lead 1, such that $E_{F0} = -E_{F1} \equiv E_F > 0$. Specifically, we tune the local Fermi energy such that $E_F = J > \Delta_0/2$, resulting in CAR dominating the nonlocal conductance for $eV < \Delta_0$. The relevant dispersion and resulting conductance are shown in Fig. 7.4.
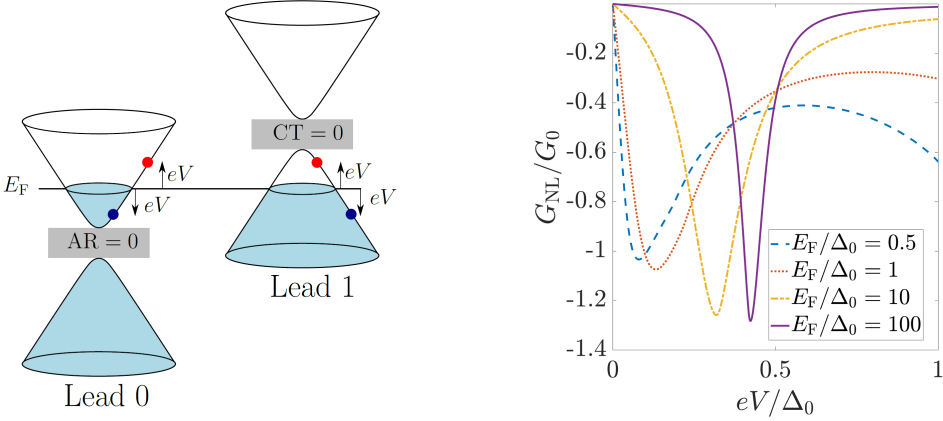

Figure 7.4. Left: the possible scattering process in a hexagonal AF-S-AF junction when lead 0 and lead 1 are electron- and hole-doped, respectively. The induced antiferromagnetic gap allows CAR to become the dominant scattering process when the gate-controllable local Fermi energy is tuned appropriately. Right: The resulting nonlocal conductance in lead 1 when $E_F = J > \Delta_0/2$.

We also investigate the robustness of our result by lifting the specific conditions $E_F = J > \Delta_0/2$. By considering the possible band structures, we map out the parameter space (E_F, J) displaying where CAR is and is not masked by CT. The complete parameter space is shown in Fig. 7.5. The figure shows that CAR dominates the nonlocal conductance (blue region) when the deviation of the local Fermi energy from the antiferromagnetic exchange energy is smaller than the voltage bias. For larger deviations, the sign of the nonlocal conductance is determined by a competition between CT and CAR (beige). If the exchange interaction is significantly larger than both the local Fermi energy and the voltage bias, then the junction is insulating, and the nonlocal conductance vanishes (red).

In contrast to a G-S-G junction, an AF-S-AF junction supports experimental detection in the experimentally more accessible regime $E_F > \Delta_0$. Additionally, a dominant CAR signal in AF-S-AF junctions is predicted on a larger voltage interval than that in G-S-G junctions.

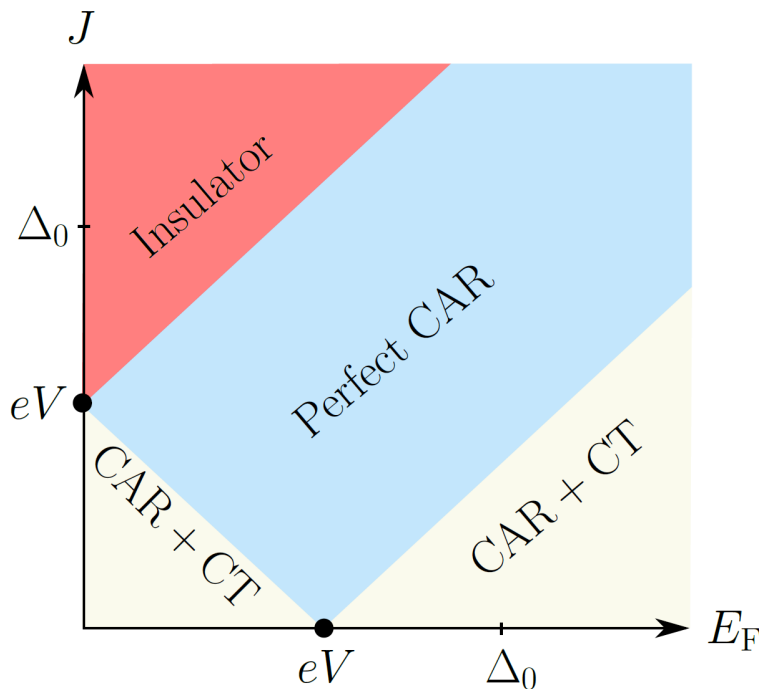Unlike ferromagnets, the density of states in antiferromagnets is spin degener-

Figure 7.5. The parameter space (E_F, J) of the total nonlocal conductance. The CAR signal dominates in the blue region. CAR competes with CT in the beige regions. The antiferromagnets are insulating, suppressing all transport properties in the red region. In the special cases $J = 0$ and $E_F = 0$, the leads are nonmagnetic graphene and undoped antiferromagnets, respectively

ate. Consequently, we expect quantum entanglement between charge carriers to be preserved in an AF-S-AF junction and destroyed in an F-S-F junction. Additionally, in an F-S-F junction, it is necessary that $J = E_F$ and $J \gg \Delta_0$ so that the density of states for minority spins is suppressed. To have CAR-dominant transport in an AF-S-AF junction, these requirements are no longer as strict, as sketched in Fig. 7.5.

In contrast to the conclusions for G-S-G and F-S-F junctions, our results suggest that an AF-S-AF junction exhibits electrically controllable, robust, and entanglement-preserving CAR. The reciprocal Cooper pair-splitting process may allow for the production of entangled electron pairs in solid-state quantum entanglement technologies. As a final remark, a recently published related work demonstrated that it is also possible to enhance CAR in an AF-S-AF system without opposite charge doping of the leads. Instead, the leads are subjected to an electric

field and contain intrinsic SOC. Consequently, both the spin and valley degeneracies of the leads break, potentially allowing for an electric-field controllable nonlocal conductance [264].

8

Conclusion and outlook

In the preceding chapters, we try to concisely introduce the physics necessary to understand and motivate the attached research papers. After all, the research papers [1–3] form the backbone of this thesis. The papers cover research within the subfields of spin insulatronics and superconducting spintronics. A central and common theme is how additional quantum mechanical degrees of freedom can be exploited to develop new technologies in the future.

In our first paper [1], we investigated the role of disorder on spin-wave transport. In one dimension, we found that disorder exponentially suppresses spin-wave conductance, a hallmark of Anderson localization. It would be interesting to extend our analysis to two and three dimensions, where we expect the Anderson localization to become less pronounced. This expectation is based on the scaling theory of Anderson localization in electronic systems [190].

We also developed a continuum theory for the transport properties of an antiferromagnet-superconductor bilayer [2]. In agreement with previous literature [204–207], we showed that the antiferromagnetic staggered field allows two unique scattering processes: specular Andreev reflection and retroreflective normal reflection. The unique scattering processes have direct and observable consequences on the electrical and thermal conductance of the system. Similar to the ferromagnet-

superconductor bilayer, we showed that it is possible to tune the supercurrent with a voltage bias. However, since the antiferromagnet produces a negligible magnetic field, the antiferromagnet-superconductor bilayer may be more suitable for high-density applications because it does not couple with stray fields or disturb other surrounding components.

In a two-dimensional antiferromagnet-superconductor-antiferromagnet trilayer, we showed that it was possible to suppress both Andreev reflection and electron cotunnelling to enhance crossed Andreev reflection [3]. In this paper, we considered two-dimensional antiferromagnets with hexagonal lattices and gate-controllable charge doping. If the two antiferromagnets are electron- and hole-doped, respectively, we predict a robust and electrically controllable experimental signature of crossed Andreev reflection in the nonlocal conductance. Enhancement of crossed Andreev reflection has also been predicted using ferromagnets instead of antiferromagnets. However, when ferromagnets are used, spin entanglement is usually not preserved because of spin splitting in the density of states [228, 233]. A promising technological application of crossed Andreev reflection is the reciprocal process where a Cooper pair is split into two entangled electrons, which may be useful in the development of solid-state quantum computers [265].

Papers [2] and [3] share possible extensions that would be interesting to explore, which we briefly mention in Sec. 3.3.1. For instance, we used the approximation that all energy scales are given by step functions. A fully self-consistent calculation with interpenetrating antiferromagnetism and superconductivity may produce new physics in devices where the length scales are on the order of the corresponding coherence lengths. In addition, in both papers, we assumed the simplest type of superconductivity, namely, the s-wave. It would of course also be interesting to study more exotic forms of superconductivity, such as d-waves, which typically produce zero-bias conductance peaks in superconducting junctions with normal metals or ferromagnets.

9

Bibliography

[1] M. F. Jakobsen, A. Qaiumzadeh, and A. Brataas, Scattering theory of transport through disordered magnets, Phys. Rev. B **100**, 134431 (2019).

[2] M. F. Jakobsen, K. B. Naess, P. Dutta, A. Brataas, and A. Qaiumzadeh, Electrical and thermal transport in antiferromagnet-superconductor junctions, Phys. Rev. B **102**, 140504 (2020).

[3] M. F. Jakobsen, A. Brataas, and A. Qaiumzadeh, Electrically Controlled Crossed Andreev Reflection in Two-Dimensional Antiferromagnets, Phys. Rev. Lett. **127**, 017701 (2021).

[4] J. S. C. Kilby, Turning Potential into Realities: The Invention of the Integrated Circuit (Nobel Lecture), Chem. Phys. Chem. **2**, 482 (2001).

[5] G. Moore, Cramming more components onto integrated circuits, Reprinted from Electronics, volume 38, number 8, April 19, 1965, pp.114 ff, Solid-State Circuits Newsletter, IEEE **11**, 33 (2006).

[6] G. Moore, Progress In Digital Integrated Electronics [Technical literature, Copyright 1975 IEEE. Reprinted, with permission. Technical Digest. Interna-

tional Electron Devices Meeting, IEEE, 1975, pp. 11-13.], Solid-State Circuits Newsletter, IEEE **20**, 36 (2006).

[7] J. Shalf, The future of computing beyond Moore's Law, Phil. Trans. Roy. Soc. A: Math., Phys., Eng. Sci. **378**, 20190061 (2020).

[8] S. A. Wolf, D. D. Awschalom, R. A. Buhrman, J. M. Daughton, S. von Molnár, M. L. Roukes, A. Y. Chtchelkanova, and D. M. Treger, Spintronics: A Spin-Based Electronics Vision for the Future, Science **294**, 1488 (2001).

[9] S. Wolf, A. Chtchelkanova, and D. Treger, Spintronics - A retrospective and perspective, IBM J. Res. Dev. **50**, 101 (2006).

[10] M. N. Baibich, J. M. Broto, A. Fert, F. N. Van Dau, F. Petroff, P. Etienne, G. Creuzet, A. Friederich, and J. Chazelas, Giant Magnetoresistance of (001)Fe/(001)Cr Magnetic Superlattices , Phys. Rev. Lett. **61**, 2472 (1988).

[11] G. Binasch, P. Grünberg, F. Saurenbach, and W. Zinn, Enhanced magnetoresistance in layered magnetic structures with antiferromagnetic interlayer exchange, Phys. Rev. B **39**, 4828 (1989).

[12] Press release: The Nobel Prize in Physics 2007, `https://www.nobelprize.org/prizes/physics/2007/summary/`, accessed: 08/07/2021.

[13] W. P. McCray, How spintronics went from the lab to the iPod, Nat. Nano. **4**, 2 (2009).

[14] W. H. Meiklejohn and C. P. Bean, New Magnetic Anisotropy, Phys. Rev. **105**, 904 (1957).

[15] M. Julliere, Tunneling between ferromagnetic films, Physics Lett. A **54**, 225 (1975).

[16] S. Yuasa, T. Nagahama, A. Fukushima, Y. Suzuki, and K. Ando, Giant room-temperature magnetoresistance in single-crystal Fe/MgO/Fe magnetic tunnel junctions, Nat. Mater. **3**, 868 (2004).

[17] S. S. P. Parkin, C. Kaiser, A. Panchula, P. M. Rice, B. Hughes, M. Samant, and S.-H. Yang, Giant tunnelling magnetoresistance at room temperature with mgo (100) tunnel barriers, Nat. Mater. **3**, 862 (2004).

[18] S. Ikeda, J. Hayakawa, Y. Ashizawa, Y. M. Lee, K. Miura, H. Hasegawa, M. Tsunoda, F. Matsukura, and H. Ohno, Tunnel magnetoresistance of 604% at 300 K by suppression of Ta diffusion in CoFeB/MgO/CoFeB pseudo-spin-valves annealed at high temperature, App. Phys. Lett. **93**, 082508 (2008).

[19] T. Song, X. Cai, M. W.-Y. Tu, X. Zhang, B. Huang, N. P. Wilson, K. L. Seyler, L. Zhu, T. Taniguchi, K. Watanabe, M. A. McGuire, D. H. Cobden, D. Xiao, W. Yao, and X. Xu, Giant tunneling magnetoresistance in spin-filter van der Waals heterostructures, Science **360**, 1214 (2018).

[20] H. H. Kim, B. Yang, T. Patel, F. Sfigakis, C. Li, S. Tian, H. Lei, and A. W. Tsen, One Million Percent Tunnel Magnetoresistance in a Magnetic van der Waals Heterostructure, Nano Lett. **18**, 4885 (2018).

[21] J. Slonczewski, Current-driven excitation of magnetic multilayers, Journal of Magnetism and Magnetic Materials **159**, L1 (1996).

[22] L. Berger, Emission of spin waves by a magnetic multilayer traversed by a current, Phys. Rev. B **54**, 9353 (1996).

[23] A. D. Kent and D. C. Worledge, A new spin on magnetic memories, Nat. Nano. **10**, 187 (2015).

[24] S. Bhatti, R. Sbiaa, A. Hirohata, H. Ohno, S. Fukami, and S. Piramanayagam, Spintronics based random access memory: a review, Materials Today **20**, 530 (2017).

[25] Everspin Technologies, *Spin-transfer Torque MRAM Technology*, `https://www.everspin.com/spin-transfer-torque-mram-technology` (2021), accessed: 24/06/2021.

[26] CMOS with a spin, Nat. Elec. **2**, 263 (2019).

[27] Avalanche Technology, *Magnetoresistive Random Access Memory Technology*, `https://www.avalanche-technology.com/technology/mram-technology/` (2021), accessed: 25/06/2021.

[28] California Memory Technologies, *Magnetic Random Access Memory P-Series Solution*, `https://memtech.ai/mram-memory-solution/` (2021), accessed: 25/06/2021.

[29] S. S. Parkin, Shiftable magnetic shift register and method of using the same, U.S. Patent 6 834 005, Dec. 21, 2004.

[30] S. S. P. Parkin, M. Hayashi, and L. Thomas, Magnetic Domain-Wall Racetrack Memory, Science **320**, 190 (2008).

[31] M. Hayashi, L. Thomas, R. Moriya, C. Rettner, and S. S. P. Parkin, Current-Controlled Magnetic Domain-Wall Nanowire Shift Register, Science **320**, 209 (2008).

[32] R. Bläsing, A. A. Khan, P. C. Filippou, C. Garg, F. Hameed, J. Castrillon, and S. S. P. Parkin, Magnetic Racetrack Memory: From Physics to the Cusp of Applications Within a Decade, Proc. IEEE **108**, 1303 (2020).

[33] C. Monzio Compagnoni, A. Goda, A. S. Spinelli, P. Feeley, A. L. Lacaita, and A. Visconti, Reviewing the Evolution of the NAND Flash Technology, Proc. IEEE **105**, 1609 (2017).

[34] S. Mittal, J. S. Vetter, and D. Li, A Survey Of Architectural Approaches for Managing Embedded DRAM and Non-Volatile On-Chip Caches, IEEE Trans. Par. Distrib. Syst. **26**, 1524 (2015).

[35] G. Sun, J. Zhao, M. Poremba, C. Xu, and Y. Xie, Memory that never forgets: emerging nonvolatile memory and the implication for architecture design, Nation. Sci. Rev. **5**, 577 (2017).

[36] J. S. Meena, S. M. Sze, U. Chand, and T.-Y. Tseng, Overview of emerging nonvolatile memory technologies, Nano. Res. Lett. **9**, 526 (2014).

[37] T. Coughlin, Crossing the Chasm to New Solid-State Storage Architectures [The Art of Storage], IEEE Cons. Elec. Mag. **5**, 133 (2016).

[38] S. Datta and B. Das, Electronic analog of the electro-optic modulator, App. Phys. Lett. **56**, 665 (1990).

[39] H. C. Koo, J. H. Kwon, J. Eom, J. Chang, S. H. Han, and M. Johnson, Control of Spin Precession in a Spin-Injected Field Effect Transistor, Science **325**, 1515 (2009).

[40] P. Chuang, S.-C. Ho, L. W. Smith, F. Sfigakis, M. Pepper, C.-H. Chen, J.-C. Fan, J. P. Griffiths, I. Farrer, H. E. Beere, G. A. C. Jones, D. A. Ritchie, and

T.-M. Chen, All-electric all-semiconductor spin field-effect transistors, Nat. Nano. **10**, 35 (2015).

[41] A. Dankert and S. P. Dash, Electrical gate control of spin current in van der Waals heterostructures at room temperature, Nat. Comms. **8**, 16093 (2017).

[42] J. Sinova and I. Žutić, New moves of the spintronics tango, Nat. Mater. **11**, 368 (2012).

[43] A. Brataas, B. van Wees, O. Klein, G. de Loubens, and M. Viret, Spin insulatronics, Phys. Rep. **885**, 1 (2020).

[44] B. Heinrich, C. Burrowes, E. Montoya, B. Kardasz, E. Girt, Y.-Y. Song, Y. Sun, and M. Wu, Spin Pumping at the Magnetic Insulator (YIG)/Normal Metal (Au) Interfaces, Phys. Rev. Lett. **107**, 066604 (2011).

[45] M. B. Jungfleisch, V. Lauer, R. Neb, A. V. Chumak, and B. Hillebrands, Improvement of the yttrium iron garnet/platinum interface for spin pumping-based applications, App. Phys. Lett. **103**, 022411 (2013).

[46] J. Xiao and G. E. W. Bauer, Spin-Wave Excitation in Magnetic Insulators by Spin-Transfer Torque, Phys. Rev. Lett. **108**, 217204 (2012).

[47] A. Kapelrud and A. Brataas, Spin Pumping and Enhanced Gilbert Damping in Thin Magnetic Insulator Films, Phys. Rev. Lett. **111**, 097602 (2013).

[48] A. Hamadeh, O. d'Allivy Kelly, C. Hahn, H. Meley, R. Bernard, A. H. Molpeceres, V. V. Naletov, M. Viret, A. Anane, V. Cros, S. O. Demokritov, J. L. Prieto, M. Muñoz, G. de Loubens, and O. Klein, Full Control of the Spin-Wave Damping in a Magnetic Insulator Using Spin-Orbit Torque, Phys. Rev. Lett. **113**, 197203 (2014).

[49] C. Du, T. van der Sar, T. X. Zhou, P. Upadhyaya, F. Casola, H. Zhang, M. C. Onbasli, C. A. Ross, R. L. Walsworth, Y. Tserkovnyak, and A. Yacoby, Control and local measurement of the spin chemical potential in a magnetic insulator, Science **357**, 195 (2017).

[50] V. E. Demidov, S. Urazhdin, B. Divinskiy, V. D. Bessonov, A. B. Rinkevich, V. V. Ustinov, and S. O. Demokritov, Chemical potential of quasi-equilibrium magnon gas driven by pure spin current, Nat. Comms. **8**, 1579 (2017).

[51] Y. Kajiwara, K. Harii, S. Takahashi, J. Ohe, K. Uchida, M. Mizuguchi, H. Umezawa, H. Kawai, K. Ando, K. Takanashi, S. Maekawa, and E. Saitoh, Transmission of electrical signals by spin-wave interconversion in a magnetic insulator, Nature **464**, 262 (2010).

[52] L. J. Cornelissen, J. Liu, R. A. Duine, J. B. Youssef, and B. J. van Wees, Long-distance transport of magnon spin information in a magnetic insulator at room temperature, Nat. Phys. **11**, 1022 (2015).

[53] C. Liu, J. Chen, T. Liu, F. Heimbach, H. Yu, Y. Xiao, J. Hu, M. Liu, H. Chang, T. Stueckler, S. Tu, Y. Zhang, Y. Zhang, P. Gao, Z. Liao, D. Yu, K. Xia, N. Lei, W. Zhao, and M. Wu, Long-distance propagation of short-wavelength spin waves, Nat. Comms. **9**, 738 (2018).

[54] R. Lebrun, A. Ross, S. A. Bender, A. Qaiumzadeh, L. Baldrati, J. Cramer, A. Brataas, R. A. Duine, and M. Kläui, Tunable long-distance spin transport in a crystalline antiferromagnetic iron oxide, Nature **561**, 222 (2018).

[55] A. V. Chumak, V. I. Vasyuchka, A. A. Serga, and B. Hillebrands, Magnon spintronics, Nat. Phys. **11**, 453 (2015).

[56] L. J. Cornelissen, J. Liu, B. J. van Wees, and R. A. Duine, Spin-Current-Controlled Modulation of the Magnon Spin Conductance in a Three-Terminal Magnon Transistor, Phys. Rev. Lett. **120**, 097702 (2018).

[57] T. Fischer, M. Kewenig, D. A. Bozhko, A. A. Serga, I. I. Syvorotka, F. Ciubotaru, C. Adelmann, B. Hillebrands, and A. V. Chumak, Experimental prototype of a spin-wave majority gate, App. Phys. Lett. **110**, 152401 (2017).

[58] J. Linder and J. W. A. Robinson, Superconducting spintronics, Nat. Phys. **11**, 307 (2015).

[59] M. Eschrig, Spin-polarized supercurrents for spintronics, Physics Today **64**, 43 (2011).

[60] R. Holm and W. Meissner, Messungen mit Hilfe von flüssigem Helium. XIII, Zeit. Phys. **74**, 715 (1932).

[61] P. G. De Gennes and E. Guyon, Superconductivity in "normal" metals, Phys. Lett. **3**, 168 (1963).

[62] N. R. Werthamer, Theory of the Superconducting Transition Temperature and Energy Gap Function of Superposed Metal Films, Phys. Rev. **132**, 2440 (1963).

[63] J. J. Hauser, H. C. Theuerer, and N. R. Werthamer, Superconductivity in Cu and Pt by Means of Superimposed Films with Lead, Phys. Rev. **136**, A637 (1964).

[64] P. G. De Gennes, Boundary Effects in Superconductors, Rev. Mod. Phys. **36**, 225 (1964).

[65] J. Clarke, Principles and applications of SQUIDs, Proc. IEEE **77**, 1208 (1989).

[66] R. Kleiner, D. Koelle, F. Ludwig, and J. Clarke, Superconducting quantum interference devices: State of the art and applications, Proc. IEEE **92**, 1534 (2004).

[67] J. Clarke and A. I. Braginski, *The SQUID handbook Vol 2 Applications of SQUIDs and SQUID systems* (Wiley-VCH, Germany, 2006).

[68] H.-S. Zhong, H. Wang, Y.-H. Deng, M.-C. Chen, L.-C. Peng, Y.-H. Luo, J. Qin, D. Wu, X. Ding, Y. Hu, P. Hu, X.-Y. Yang, W.-J. Zhang, H. Li, Y. Li, X. Jiang, L. Gan, G. Yang, L. You, Z. Wang, L. Li, N.-L. Liu, C.-Y. Lu, and J.-W. Pan, Quantum computational advantage using photons, Science **370**, 1460 (2020).

[69] D. Castelvecchi, IBM's quantum cloud computer goes commercial, Nature **543**, 159 (2017).

[70] F. Arute *et al.*, Quantum supremacy using a programmable superconducting processor, Nature **574**, 505 (2019).

[71] D. Maslov, J.-S. Kim, S. Bravyi, T. J. Yoder, and S. Sheldon, Quantum advantage for computations with limited space, Nat. Phys. 10.1038/s41567-021-01271-7 (2021).

[72] K. Olejník, T. Seifert, Z. Kašpar, V. Novák, P. Wadley, R. P. Campion, M. Baumgartner, P. Gambardella, P. Němec, J. Wunderlich, J. Sinova, P. Kužel, M. Müller, T. Kampfrath, and T. Jungwirth, Terahertz electrical writing speed in an antiferromagnetic memory, Sci. Adv. **4**, 10.1126/sciadv.aar3566 (2018).

[73] V. Baltz, A. Manchon, M. Tsoi, T. Moriyama, T. Ono, and Y. Tserkovnyak, Antiferromagnetic spintronics, Rev. Mod. Phys. **90**, 015005 (2018).

[74] T. Jungwirth, X. Marti, P. Wadley, and J. Wunderlich, Antiferromagnetic spintronics, Nat. Nano. **11**, 231 (2016).

[75] J. Železný, H. Gao, K. Výborný, J. Zemen, J. Mašek, A. Manchon, J. Wunder-lich, J. Sinova, and T. Jungwirth, Relativistic Néel-Order Fields Induced by Electrical Current in Antiferromagnets, Phys. Rev. Lett. **113**, 157201 (2014).

[76] P. Wadley *et al.*, Electrical switching of an antiferromagnet, Science **351**, 587 (2016).

[77] T. Kosub, M. Kopte, R. Hühne, P. Appel, B. Shields, P. Maletinsky, R. Hüb-ner, M. O. Liedke, J. Fassbender, O. G. Schmidt, and D. Makarov, Purely antiferromagnetic magnetoelectric random access memory, Nat. Comms. **8**, 13985 (2017).

[78] P. Coleman, *Introduction to Many-Body Physics* (Cambridge University Press, 2015).

[79] A. Altland and B. D. Simons, *Condensed Matter Field Theory*, 2nd ed. (Cambridge University Press, 2010).

[80] W. Heisenberg, Zur Theorie des Ferromagnetismus, Zeit. Phys. **49**, 619 (1928).

[81] J. Hubbard and B. H. Flowers, Electron correlations in narrow energy bands, Proc. Roy. Soc. Lond. A. Math. Phys. Sci. **276**, 238 (1963).

[82] Y. Nagaoka, Ferromagnetism in a Narrow, Almost Half-Filled s Band, Phys. Rev. **147**, 392 (1966).

[83] A. Mielke and H. Tasaki, Ferromagnetism in the Hubbard model. Examples from models with degenerate single-electron ground states, Comms. Math. Phys. **158**, 341 (1993).

[84] T. Holstein and H. Primakoff, Field Dependence of the Intrinsic Domain Magnetization of a Ferromagnet, Phys. Rev. **58**, 1098 (1940).

[85] J. G. Valatin, Comments on the theory of superconductivity, Il Nuovo Cimento (1955-1965) **7**, 843 (1958).

[86] N. N. Bogoljubov, On a new method in the theory of superconductivity, Il Nuovo Cimento (1955-1965) **7**, 794 (1958).

[87] P. C. Hohenberg, Existence of Long-Range Order in One and Two Dimensions, Phys. Rev. **158**, 383 (1967).

[88] N. D. Mermin and H. Wagner, Absence of Ferromagnetism or Antiferromagnetism in One- or Two-Dimensional Isotropic Heisenberg Models, Phys. Rev. Lett. **17**, 1133 (1966).

[89] B. I. Halperin, On the Hohenberg–Mermin–Wagner Theorem and Its Limitations, Journal of Statistical Physics **175**, 521 (2019).

[90] J.-U. Lee, S. Lee, J. H. Ryoo, S. Kang, T. Y. Kim, P. Kim, C.-H. Park, J.-G. Park, and H. Cheong, Ising-Type Magnetic Ordering in Atomically Thin FePS3, Nano Lett. **16**, 7433 (2016).

[91] C.-T. Kuo, M. Neumann, K. Balamurugan, H. J. Park, S. Kang, H. W. Shiu, J. H. Kang, B. H. Hong, M. Han, T. W. Noh, and J.-G. Park, Exfoliation and Raman Spectroscopic Fingerprint of Few-Layer NiPS3 Van der Waals Crystals, Sci. Rep. **6**, 20904 (2016), srep20904[PII].

[92] J.-U. Lee, S. Lee, J. H. Ryoo, S. Kang, T. Y. Kim, P. Kim, C.-H. Park, J.-G. Park, and H. Cheong, Ising-Type Magnetic Ordering in Atomically Thin FePS3, Nano Lett. **16**, 7433 (2016).

[93] S. Lee, K.-Y. Choi, S. Lee, B. H. Park, and J.-G. Park, Tunneling transport of mono- and few-layers magnetic van der Waals MnPS3, APL Materials **4**, 086108 (2016).

[94] B. Huang, G. Clark, E. Navarro-Moratalla, D. R. Klein, R. Cheng, K. L. Seyler, D. Zhong, E. Schmidgall, M. A. McGuire, D. H. Cobden, W. Yao, D. Xiao, P. Jarillo-Herrero, and X. Xu, Layer-dependent ferromagnetism in a van der Waals crystal down to the monolayer limit, Nature **546**, 270 (2017).

[95] C. Gong, L. Li, Z. Li, H. Ji, A. Stern, Y. Xia, T. Cao, W. Bao, C. Wang, Y. Wang, Z. Q. Qiu, R. J. Cava, S. G. Louie, J. Xia, and X. Zhang, Discovery of intrinsic ferromagnetism in two-dimensional van der Waals crystals, Nature **546**, 265 (2017).

[96] N. Samarth, Magnetism in flatland, Nature **546**, 216 (2017).

[97] Z. Fei, B. Huang, P. Malinowski, W. Wang, T. Song, J. Sanchez, W. Yao, D. Xiao, X. Zhu, A. F. May, W. Wu, D. H. Cobden, J.-H. Chu, and X. Xu, Two-dimensional itinerant ferromagnetism in atomically thin Fe3GeTe2, Nat. Mater. **17**, 778 (2018).

[98] D. J. O'Hara, T. Zhu, A. H. Trout, A. S. Ahmed, Y. K. Luo, C. H. Lee, M. R. Brenner, S. Rajan, J. A. Gupta, D. W. McComb, and R. K. Kawakami, Room Temperature Intrinsic Ferromagnetism in Epitaxial Manganese Selenide Films in the Monolayer Limit, Nano Lett. **18**, 3125 (2018).

[99] K. S. Burch, D. Mandrus, and J.-G. Park, Magnetism in two-dimensional van der Waals materials, Nature **563**, 47 (2018).

[100] Y. Deng, Y. Yu, Y. Song, J. Zhang, N. Z. Wang, Z. Sun, Y. Yi, Y. Z. Wu, S. Wu, J. Zhu, J. Wang, X. H. Chen, and Y. Zhang, Gate-tunable room-temperature ferromagnetism in two-dimensional Fe3GeTe2, Nature **563**, 94 (2018).

[101] M. Gibertini, M. Koperski, A. F. Morpurgo, and K. S. Novoselov, Magnetic 2D materials and heterostructures, Nat. Nano. **14**, 408 (2019).

[102] R. J. Birgeneau and G. Shirane, Magnetism in one dimension, Physics Today **31**, 32 (1978).

[103] A. K. Bera, B. Lake, F. H. L. Essler, L. Vanderstraeten, C. Hubig, U. Schollwöck, A. T. M. N. Islam, A. Schneidewind, and D. L. Quintero-Castro, Spinon confinement in a quasi-one-dimensional anisotropic Heisenberg magnet, Phys. Rev. B **96**, 054423 (2017).

[104] A. Sapkota, B. G. Ueland, V. K. Anand, N. S. Sangeetha, D. L. Abernathy, M. B. Stone, J. L. Niedziela, D. C. Johnston, A. Kreyssig, A. I. Goldman, and R. J. McQueeney, Effective One-Dimensional Coupling in the Highly Frustrated Square-Lattice Itinerant Magnet $CaCo_{2-y}As_2$, Phys. Rev. Lett. **119**, 147201 (2017).

[105] M. Nishi, O. Fujita, and J. Akimitsu, Neutron-scattering study on the spin-Peierls transition in a quasi-one-dimensional magnet $CuGeO_3$, Phys. Rev. B **50**, 6508 (1994).

[106] M. Steiner, J. Villain, and C. Windsor, Theoretical and experimental studies on one-dimensional magnetic systems, Adv. Phys. **25**, 87 (1976).

[107] D. van Delft, Little cup of helium, big science, Physics Today **61**, 36 (2008).

[108] H. K. Onnes, Further experiments with liquid helium. C. On the change of electric resistance of pure metals at very low temperatures etc. IV. The resistance of pure mercury at helium temperatures, in *Through Measurement to Knowledge: The Selected Papers of Heike Kamerlingh Onnes 1853–1926*, edited by K. Gavroglu and Y. Goudaroulis (Springer Netherlands, Dordrecht, 1991) pp. 261–263.

[109] van Delft, Dirk and Kes, Peter, The discovery of superconductivity, Europhys. News **42**, 21 (2011).

[110] D. van Delft and P. Kes, The discovery of superconductivity, Physics Today **63**, 38 (2010).

[111] W. Meissner and R. Ochsenfeld, Ein neuer Effekt bei Eintritt der Supraleitfähigkeit, Naturwissenschaften **21**, 787 (1933).

[112] J. Bardeen, L. N. Cooper, and J. R. Schrieffer, Microscopic Theory of Superconductivity, Phys. Rev. **106**, 162 (1957).

[113] J. Bardeen, L. N. Cooper, and J. R. Schrieffer, Theory of Superconductivity, Phys. Rev. **108**, 1175 (1957).

[114] E. Maxwell, The isotope effect in superconductivity, Physics Today **5**, 14 (1952).

[115] M. Tinkham, *Introduction to Superconductivity*, International series in pure and applied physics (McGraw Hill, 1996).

[116] L. N. Cooper, Bound Electron Pairs in a Degenerate Fermi Gas, Phys. Rev. **104**, 1189 (1956).

[117] E. Maxwell, Isotope Effect in the Superconductivity of Mercury, Phys. Rev. **78**, 477 (1950).

[118] C. A. Reynolds, B. Serin, W. H. Wright, and L. B. Nesbitt, Superconductivity of Isotopes of Mercury, Phys. Rev. **78**, 487 (1950).

[119] P. G. De Gennes, *Superconductivity of Metals and Alloys*, Advanced book classics (Perseus, Cambridge, MA, 1999).

[120] K. D. Usadel, Generalized Diffusion Equation for Superconducting Alloys, Phys. Rev. Lett. **25**, 507 (1970).

[121] A. H. Mitchell, Ferromagnetic Relaxation by the Exchange Interaction between Ferromagnetic Electrons and Conduction Electrons, Phys. Rev. **105**, 1439 (1957).

[122] C. Zener, Interaction Between the d Shells in the Transition Metals, Phys. Rev. **81**, 440 (1951).

[123] T. Kasuya, A Theory of Metallic Ferro- and Antiferromagnetism on Zener's Model, Prog. Theor. Phys. **16**, 45 (1956).

[124] M. Octavio, M. Tinkham, G. E. Blonder, and T. M. Klapwijk, Subharmonic energy-gap structure in superconducting constrictions, Phys. Rev. B **27**, 6739 (1983).

[125] G. E. Blonder and M. Tinkham, Metallic to tunneling transition in Cu-Nb point contacts, Phys. Rev. B **27**, 112 (1983).

[126] Y. G. Naidyuk and K. Gloos, Anatomy of point-contact Andreev reflection spectroscopy from the experimental point of view, Low Temperature Physics **44**, 257 (2018).

[127] V. Galitski and I. B. Spielman, Spin–orbit coupling in quantum gases, Nature **494**, 49 (2013).

[128] R. Winkler, *Spin-orbit coupling effects in two-dimensional electron and hole systems*, Springer tracts in modern physics (Springer, Berlin, 2003).

[129] A. Manchon, H. C. Koo, J. Nitta, S. M. Frolov, and R. A. Duine, New perspectives for Rashba spin–orbit coupling, Nat. Mater. **14**, 871 (2015).

[130] Y. A. Bychkov and E. I. Rashba, Oscillatory effects and the magnetic susceptibility of carriers in inversion layers, J. Phys. C: S. S. Phys. **17**, 6039 (1984).

[131] G. Dresselhaus, Spin-Orbit Coupling Effects in Zinc Blende Structures, Phys. Rev. **100**, 580 (1955).

[132] C. L. Kane and E. J. Mele, Quantum Spin Hall Effect in Graphene, Phys. Rev. Lett. **95**, 226801 (2005).

[133] F. D. M. Haldane, Model for a Quantum Hall Effect without Landau Levels: Condensed-Matter Realization of the "Parity Anomaly", Phys. Rev. Lett. **61**, 2015 (1988).

[134] M. Sigrist and K. Ueda, Phenomenological theory of unconventional superconductivity, Rev. Mod. Phys. **63**, 239 (1991).

[135] K. S. Novoselov, A. K. Geim, S. V. Morozov, D. Jiang, Y. Zhang, S. V. Dubonos, I. V. Grigorieva, and A. A. Firsov, Electric Field Effect in Atomically Thin Carbon Films, Science **306**, 666 (2004).

[136] K. S. Novoselov, A. K. Geim, S. V. Morozov, D. Jiang, M. I. Katsnelson, I. V. Grigorieva, S. V. Dubonos, and A. A. Firsov, Two-dimensional gas of massless Dirac fermions in graphene, Nature **438**, 197 (2005).

[137] R. Landauer, Spatial Variation of Currents and Fields Due to Localized Scatterers in Metallic Conduction, IBM J. Res. and Develop. **1**, 223 (1957).

[138] R. Landauer, Electrical resistance of disordered one-dimensional lattices, Phil. Mag. **21**, 863 (1970).

[139] R. Landauer, Residual resistivity dipoles, Z. Phys. B. **21**, 247 (1975).

[140] M. Büttiker, Scattering theory of thermal and excess noise in open conductors, Phys. Rev. Lett. **65**, 2901 (1990).

[141] M. Büttiker, Scattering theory of current and intensity noise correlations in conductors and wave guides, Phys. Rev. B **46**, 12485 (1992).

[142] M. Buttiker, Capacitance, admittance, and rectification properties of small conductors, J. Phys. Cond. Mat. **5**, 9361 (1993).

[143] D. S. Fisher and P. A. Lee, Relation between conductivity and transmission matrix, Phys. Rev. B **23**, 6851 (1981).

[144] Y. Imry, Physics of Mesoscopic Systems, in *Directions in Condensed Matter Physics*, pp. 101–163.

[145] Y. Imry, *Introduction to Mesoscopic Physics*, Mesoscopic physics and nanotechnology (Oxford University Press, 2002).

[146] M. Büttiker and M. Moskalets, From Anderson Localization to Mesoscopic Physics, International Journal of Modern Physics B **24**, 1555 (2010).

[147] C. W. J. Beenakker, Random-matrix theory of quantum transport, Rev. Mod. Phys. **69**, 731 (1997).

[148] S. Datta, *Electronic Transport in Mesoscopic Systems*, Cambridge Studies in Semiconductor Physics and Microelectronic Engineering (Cambridge University Press, 1995).

[149] G. E. Blonder, M. Tinkham, and T. M. Klapwijk, Transition from metallic to tunneling regimes in superconducting microconstrictions: Excess current, charge imbalance, and supercurrent conversion, Phys. Rev. B **25**, 4515 (1982).

[150] M. J. M. de Jong and C. W. J. Beenakker, Andreev Reflection in Ferromagnet-Superconductor Junctions, Phys. Rev. Lett. **74**, 1657 (1995).

[151] S. Chaudhuri and P. F. Bagwell, Andreev resonances in the current-voltage characteristics of a normal-metal–superconductor junction, Phys. Rev. B **51**, 16936 (1995).

[152] R. A. Riedel and P. F. Bagwell, Current-voltage relation of a normal-metal–superconductor junction, Phys. Rev. B **48**, 15198 (1993).

[153] J. A. Sauls, Andreev bound states and their signatures, Phil. Trans. Roy. Soc. A: Math., Phys., Eng. Sci. **376**, 20180140 (2018).

[154] C. W. J. Beenakker, Specular Andreev Reflection in Graphene, Phys. Rev. Lett. **97**, 067007 (2006).

[155] G. Deutscher and D. Feinberg, Coupling superconducting-ferromagnetic point contacts by Andreev reflections, App. Phys. Lett. **76**, 487 (2000).

[156] P. W. Anderson, Absence of Diffusion in Certain Random Lattices, Phys. Rev. **109**, 1492 (1958).

[157] D. Vollhardt and P. Wölfle, Scaling Equations from a Self-Consistent Theory of Anderson Localization, Phys. Rev. Lett. **48**, 699 (1982).

[158] D. Wesenberg, T. Liu, D. Balzar, M. Wu, and B. L. Zink, Long-distance spin transport in a disordered magnetic insulator, Nat. Phys. **13**, 987 (2017).

[159] J. M. Gomez-Perez, K. Oyanagi, R. Yahiro, R. Ramos, L. E. Hueso, E. Saitoh, and F. Casanova, Absence of evidence of spin transport through amorphous Y3Fe5O12, App. Phys. Lett. **116**, 032401 (2020).

[160] M. Pfirrmann, I. Boventer, A. Schneider, T. Wolz, M. Kläui, A. V. Ustinov, and M. Weides, Magnons at low excitations: Observation of incoherent coupling to a bath of two-level systems, Phys. Rev. Res. **1**, 032023 (2019).

[161] H. Yu, J. Xiao, and H. Schultheiss, Magnetic texture based magnonics, Phys. Rep. **905**, 1 (2021).

[162] Y. Fujimoto, M. Ichioka, and H. Adachi, Spin pumping into a spin glass material, Phys. Rev. B **101**, 184412 (2020).

[163] H. Ochoa, R. Zarzuela, and Y. Tserkovnyak, Spin hydrodynamics in amorphous magnets, Phys. Rev. B **98**, 054424 (2018).

[164] Y. Tserkovnyak and H. Ochoa, Generalized boundary conditions for spin transfer, Phys. Rev. B **96**, 100402 (2017).

[165] N. Arakawa and J.-i. Ohe, Inplane anisotropy of longitudinal thermal conductivities and weak localization of magnons in a disordered spiral magnet, Phys. Rev. B **98**, 014421 (2018).

[166] M. Evers, C. A. Müller, and U. Nowak, Weak localization of magnons in chiral magnets, Phys. Rev. B **97**, 184423 (2018).

[167] P. Buczek, S. Thomas, A. Marmodoro, N. Buczek, X. Zubizarreta, M. Hoffmann, T. Balashov, W. Wulfhekel, K. Zakeri, and A. Ernst, Spin waves in disordered materials, J. Phys.: Cond. Mat. **30**, 423001 (2018).

[168] U. Kamber, A. Bergman, A. Eich, D. Iuşan, M. Steinbrecher, N. Hauptmann, L. Nordström, M. I. Katsnelson, D. Wegner, O. Eriksson, and A. A. Khajetoorians, Self-induced spin glass state in elemental and crystalline neodymium, Science **368**, eaay6757 (2020).

[169] P. W. Anderson, Spin Glass I: A Scaling Law Rescued, Physics Today **41**, 9 (1988).

[170] P. W. Anderson, Spin Glass II: Is There a Phase Transition?, Physics Today **41**, 9 (1988).

[171] P. W. Anderson, Spin Glass III: Theory Raises its Head, Physics Today **41**, 9 (1988).

[172] P. W. Anderson, Spin Glass IV: Glimmerings of Trouble, Physics Today **41**, 9 (1988).

[173] P. W. Anderson, Spin Glass V: Real Power Brought to Bear, Physics Today **42**, 9 (1989).

[174] P. W. Anderson, Spin Glass VI: Spin Glass As Cornucopia, Physics Today **42**, 9 (1989).

[175] P. W. Anderson, Spin Glass VII: Spin Glass as Paradigm, Physics Today **43**, 9 (1990).

[176] S. Fishman and A. Aharony, Random field effects in disordered anisotropic antiferromagnets, J. Phys. C: S. S. Phys. **12**, L729 (1979).

[177] J. L. Cardy, Random-field effects in site-disordered Ising antiferromagnets, Phys. Rev. B **29**, 505 (1984).

[178] A. P. Young, *Spin Glasses and Random Fields* (World Scientific, 1997).

[179] J. M. Kosterlitz, D. J. Thouless, and R. C. Jones, Spherical Model of a Spin-Glass, Phys. Rev. Lett. **36**, 1217 (1976).

[180] P. Shukla and S. Singh, Classical and quantum spherical models of spin-glasses: A complete treatment of statistics and dynamics, Phys. Rev. B **23**, 4661 (1981).

[181] S. F. Edwards and P. W. Anderson, Theory of spin glasses, J. Phys. F: Metal Physics **5**, 965 (1975).

[182] D. Sherrington and S. Kirkpatrick, Solvable Model of a Spin-Glass, Phys. Rev. Lett. **35**, 1792 (1975).

[183] G. Parisi, Infinite Number of Order Parameters for Spin-Glasses, Phys. Rev. Lett. **43**, 1754 (1979).

[184] M. Evers, C. A. Müller, and U. Nowak, Spin-wave localization in disordered magnets, Phys. Rev. B **92**, 014411 (2015).

[185] U. Ritzmann, D. Hinzke, and U. Nowak, Propagation of thermally induced magnonic spin currents, Phys. Rev. B **89**, 024409 (2014).

[186] O. Eriksson, A. Bergman, L. Bergqvist, and J. Hellsvik, *Atomistic Spin Dynamics: Foundations and Applications* (Oxford University Press, Oxford, 2017).

[187] T. Gilbert, A phenomenological theory of damping in ferromagnetic materials, IEEE Trans. Mag. **40**, 3443 (2004).

[188] T. L. Gilbert and J. M. Kelly, Anomalous Rotational Damping in Ferromagnetic Sheets, in *Conference on magnetism and magnetic materials: papers presented, Pittsburgh, Pa., June 14-16, 1955* (American Institute of Electrical Engineers, 1955) pp. 253–263.

[189] M. Lakshmanan, The fascinating world of the Landau-Lifshitz-Gilbert equation: an overview, Phil. Trans. Roy. Soc. A: Math., Phys., Eng. Sci. **369**, 1280 (2011).

[190] E. Abrahams, P. W. Anderson, D. C. Licciardello, and T. V. Ramakrishnan, Scaling Theory of Localization: Absence of Quantum Diffusion in Two Dimensions, Phys. Rev. Lett. **42**, 673 (1979).

[191] A. Lagendijk, B. v. Tiggelen, and D. S. Wiersma, Fifty years of Anderson localization, Physics Today **62**, 24 (2009).

[192] A. F. Andreev, Thermal conductivity of the intermediate state of superconductors, JETP **19**, 1228 (1964).

[193] P. de Gennes and D. Saint-James, Elementary excitations in the vicinity of a normal metal-superconducting metal contact, Phys. Lett. **4**, 151 (1963).

[194] G. Deutscher, Andreev–Saint-James reflections: A probe of cuprate superconductors, Rev. Mod. Phys. **77**, 109 (2005).

[195] Y. V. Sharvin, A Possible Method for Studying Fermi Surfaces, Sov. J. Exp. Theor. Phys. **21**, 655 (1965).

[196] I. Žutić, J. Fabian, and S. Das Sarma, Spintronics: Fundamentals and applications, Rev. Mod. Phys. **76**, 323 (2004).

[197] S. K. Upadhyay, A. Palanisami, R. N. Louie, and R. A. Buhrman, Probing Ferromagnets with Andreev Reflection, Phys. Rev. Lett. **81**, 3247 (1998).

[198] V. A. Vas'ko, K. R. Nikolaev, V. A. Larkin, P. A. Kraus, and A. M. Gold-
man, Differential conductance of the ferromagnet/superconductor interface of
DyBa2Cu3O7/La2/3Ba1/3MnO3 heterostructures, App. Phys. Lett. **73**, 844
(1998).

[199] J.-X. Zhu, B. Friedman, and C. S. Ting, Spin-polarized quasiparticle transport
in ferromagnet–d-wave-superconductor junctions with a 110 interface, Phys.
Rev. B **59**, 9558 (1999).

[200] I. Žutić and O. T. Valls, Spin-polarized tunneling in ferromag-
net/unconventional superconductor junctions, Phys. Rev. B **60**, 6320 (1999).

[201] P. Högl, A. Matos-Abiague, I. Žutić, and J. Fabian, Magnetoanisotropic An-
dreev Reflection in Ferromagnet-Superconductor Junctions, Phys. Rev. Lett.
115, 116601 (2015).

[202] P. Dutta, K. R. Alves, and A. M. Black-Schaffer, Thermoelectricity carried
by proximity-induced odd-frequency pairing in ferromagnet/superconductor
junctions, Phys. Rev. B **102**, 094513 (2020).

[203] A. Costa, A. Matos-Abiague, and J. Fabian, Skew Andreev reflection in fer-
romagnet/superconductor junctions, Phys. Rev. B **100**, 060507 (2019).

[204] I. V. Bobkova, P. J. Hirschfeld, and Y. S. Barash, Spin-Dependent Quasiparti-
cle Reflection and Bound States at Interfaces with Itinerant Antiferromagnets,
Phys. Rev. Lett. **94**, 037005 (2005).

[205] B. M. Andersen, I. V. Bobkova, P. J. Hirschfeld, and Y. S. Barash, Bound
states at the interface between antiferromagnets and superconductors, Phys.
Rev. B **72**, 184510 (2005).

[206] D. S. Rabinovich, I. V. Bobkova, and A. M. Bobkov, Anomalous phase shift
in a Josephson junction via an antiferromagnetic interlayer, Phys. Rev. Res.
1, 033095 (2019).

[207] B. M. Andersen, I. V. Bobkova, P. J. Hirschfeld, and Y. S. Barash, $0 - \pi$
Transitions in Josephson Junctions with Antiferromagnetic Interlayers, Phys.
Rev. Lett. **96**, 117005 (2006).

[208] C. Bell, E. J. Tarte, G. Burnell, C. W. Leung, D.-J. Kang, and M. G. Blamire,
Proximity and Josephson effects in superconductor/antiferromagnetic $Nb/\gamma-$
$Fe_{50}Mn_{50}$ heterostructures, Phys. Rev. B **68**, 144517 (2003).

[209] P. Komissinskiy, G. A. Ovsyannikov, I. V. Borisenko, Y. V. Kislinskii, K. Y. Constantinian, A. V. Zaitsev, and D. Winkler, Josephson Effect in Hybrid Oxide Heterostructures with an Antiferromagnetic Layer, Phys. Rev. Lett. **99**, 017004 (2007).

[210] R. J. Soulen, J. M. Byers, M. S. Osofsky, B. Nadgorny, T. Ambrose, S. F. Cheng, P. R. Broussard, C. T. Tanaka, J. Nowak, J. S. Moodera, A. Barry, and J. M. D. Coey, Measuring the Spin Polarization of a Metal with a Superconducting Point Contact, Science **282**, 85 (1998).

[211] P. Parab, D. Singh, S. Haram, R. P. Singh, and S. Bose, Point contact Andreev reflection studies of a non-centro symmetric superconductor Re6Zr, Sci. Rep. **9**, 2498 (2019).

[212] R. Gonnelli, D. Daghero, and M. Tortello, Point contact spectroscopy in Fe-based superconductors: Recent advancements and future challenges, Current Opinion in Solid State and Materials Science **17**, 72 (2013), fe-based Superconductors.

[213] G. Annunziata, M. Cuoco, P. Gentile, A. Romano, and C. Noce, Charge and spin transport through a ferromagnet/insulator/unconventional superconductor junction, Phys. Rev. B **83**, 094507 (2011).

[214] D. Daghero, M. Tortello, G. A. Ummarino, and R. S. Gonnelli, Directional point-contact Andreev-reflection spectroscopy of Fe-based superconductors: Fermi surface topology, gap symmetry, and electron–boson interaction, Rep. Prog. Phys. **74**, 124509 (2011).

[215] J. Geerk, X. X. Xi, and G. Linker, Electron tunneling into thin films of Y1Ba2Cu3O7, Zeit. Phys. B Cond. Mat. **73**, 329 (1988).

[216] J. Lesueur, L. Greene, W. Feldmann, and A. Inam, Zero bias anomalies in YBa2Cu3O7 tunnel junctions, Phys. C: Supercond. **191**, 325 (1992).

[217] M. Covington, R. Scheuerer, K. Bloom, and L. H. Greene, Tunneling and anisotropic charge transport properties of superconducting (110)-oriented YBa2Cu3O7 thin films, App. Phys. Lett. **68**, 1717 (1996).

[218] M. Covington, M. Aprili, E. Paraoanu, L. H. Greene, F. Xu, J. Zhu, and C. A. Mirkin, Observation of Surface-Induced Broken Time-Reversal Symmetry in $YBa_2Cu_3O_7$ Tunnel Junctions, Phys. Rev. Lett. **79**, 277 (1997).

[219] C.-R. Hu, Midgap Surface States as a Novel Signature for d_{xa}^2-x_b^2-wave Super-
conductivity, Phys. Rev. Lett. **72**, 1526 (1994).

[220] Y. Tanaka and S. Kashiwaya, Theory of Tunneling Spectroscopy of d-Wave
Superconductors, Phys. Rev. Lett. **74**, 3451 (1995).

[221] S. Kashiwaya, Y. Tanaka, M. Koyanagi, H. Takashima, and K. Kajimura,
Tunneling spectroscopy of d-wave superconductors, J. Phys. Chem. Sol. **56**,
1721 (1995), proceedings of the Conference on Spectroscopies in Novel Super-
conductors.

[222] S. Kashiwaya, Y. Tanaka, M. Koyanagi, and K. Kajimura, Theory for tun-
neling spectroscopy of anisotropic superconductors, Phys. Rev. B **53**, 2667
(1996).

[223] P. A. M. Benistant, A. P. van Gelder, H. van Kempen, and P. Wyder, Angular
relation and energy dependence of Andreev reflection, Phys. Rev. B **32**, 3351
(1985).

[224] G. Falci, D. Feinberg, and F. W. J. Hekking, Correlated tunneling into a
superconductor in a multiprobe hybrid structure, Europhys. Lett. **54**, 255
(2001).

[225] M. S. Kalenkov and A. D. Zaikin, Nonlocal Andreev reflection at high trans-
missions, Phys. Rev. B **75**, 172503 (2007).

[226] J. P. Morten, D. Huertas-Hernando, W. Belzig, and A. Brataas, Full counting
statistics of crossed Andreev reflection, Phys. Rev. B **78**, 224515 (2008).

[227] H. Cheraghchi, H. Esmailzadeh, and A. G. Moghaddam, Superconducting elec-
tron and hole lenses, Phys. Rev. B **93**, 214508 (2016).

[228] J. Linder, M. Zareyan, and A. Sudbø, Spin-switch effect from crossed Andreev
reflection in superconducting graphene spin valves, Phys. Rev. B **80**, 014513
(2009).

[229] K. Li and Y.-Y. Zhang, Spin-filtered and spatially distinguishable crossed An-
dreev reflection in a silicene-superconductor junction, Phys. Rev. B **94**, 165441
(2016).

[230] R. Beiranvand, H. Hamzehpour, and M. Alidoust, Nonlocal Andreev entanglements and triplet correlations in graphene with spin-orbit coupling, Phys. Rev. B **96**, 161403(R) (2017).

[231] F. Giazotto, F. Taddei, F. Beltram, and R. Fazio, Crossed Andreev Reflection-Induced Magnetoresistance, Phys. Rev. Lett. **97**, 087001 (2006).

[232] J. Cayssol, Crossed Andreev Reflection in a Graphene Bipolar Transistor, Phys. Rev. Lett. **100**, 147001 (2008).

[233] M. Veldhorst and A. Brinkman, Nonlocal Cooper Pair Splitting in a $p\mathbf{S}n$ Junction, Phys. Rev. Lett. **105**, 107002 (2010).

[234] J. Nilsson, A. R. Akhmerov, and C. W. J. Beenakker, Splitting of a Cooper Pair by a Pair of Majorana Bound States, Phys. Rev. Lett. **101**, 120403 (2008).

[235] W. Chen, R. Shen, L. Sheng, B. G. Wang, and D. Y. Xing, Electron Entanglement Detected by Quantum Spin Hall Systems, Phys. Rev. Lett. **109**, 036802 (2012).

[236] W. Chen, R. Shen, L. Sheng, B. G. Wang, and D. Y. Xing, Resonant nonlocal Andreev reflection in a narrow quantum spin hall system, Phys. Rev. B **84**, 115420 (2011).

[237] R. W. Reinthaler, P. Recher, and E. M. Hankiewicz, Proposal for an All-Electrical Detection of Crossed Andreev Reflection in Topological Insulators, Phys. Rev. Lett. **110**, 226802 (2013).

[238] J. J. He, J. Wu, T.-P. Choy, X.-J. Liu, Y. Tanaka, and K. T. Law, Correlated spin currents generated by resonant-crossed Andreev reflections in topological superconductors, Nat. Comms. **5**, 3232 (2014).

[239] J. Wang, L. Hao, and K. S. Chan, Quantized crossed-Andreev reflection in spin-valley topological insulators, Phys. Rev. B **91**, 085415 (2015).

[240] A. Kleine, A. Baumgartner, J. Trbovic, and C. Schönenberger, Contact resistance dependence of crossed Andreev reflection, Europhys. Lett. **87**, 27011 (2009).

[241] S. Russo, M. Kroug, T. M. Klapwijk, and A. F. Morpurgo, Experimental Observation of Bias-Dependent Nonlocal Andreev Reflection, Phys. Rev. Lett. **95**, 027002 (2005).

[242] P. Cadden-Zimansky and V. Chandrasekhar, Nonlocal Correlations in Normal-Metal Superconducting Systems, Phys. Rev. Lett. **97**, 237003 (2006).

[243] P. Cadden-Zimansky, J. Wei, and V. Chandrasekhar, Cooper-pair-mediated coherence between two normal metals, Nat. Phys. **5**, 393 (2009).

[244] J. Wei and V. Chandrasekhar, Positive noise cross-correlation in hybrid superconducting and normal-metal three-terminal devices, Nat. Phys. **6**, 494 (2010).

[245] A. Das, Y. Ronen, M. Heiblum, D. Mahalu, A. V. Kretinin, and H. Shtrikman, High-efficiency Cooper pair splitting demonstrated by two-particle conductance resonance and positive noise cross-correlation, Nat. Comms. **3**, 1165 (2012).

[246] D. Beckmann, H. B. Weber, and H. v. Löhneysen, Evidence for Crossed Andreev Reflection in Superconductor-Ferromagnet Hybrid Structures, Phys. Rev. Lett. **93**, 197003 (2004).

[247] I. Asulin, O. Yuli, G. Koren, and O. Millo, Evidence for crossed Andreev reflections in bilayers of (100) $YBa_2Cu_3O_{7-\delta}$ and the itinerant ferromagnet $SrRuO_3$, Phys. Rev. B **74**, 092501 (2006).

[248] D. Beckmann and H. v. Löhneysen, Negative four-terminal resistance as a probe of crossed Andreev reflection, App. Phys. A **89**, 603 (2007).

[249] H. v. Löhneysen, D. Beckmann, F. Pérez-Willard, M. Schöck, C. Strunk, and C. Sürgers, Proximity effect between superconductors and ferromagnets: from thin films to nanostructures, Ann. d. Phys. **14**, 591 (2005).

[250] P. Aronov and G. Koren, Signature of a crossed Andreev reflection effect in the magnetic response of $YBa_2Cu_3O_{7-\delta}$ junctions with the itinerant ferromagnet $SrRuO_3$, Phys. Rev. B **72**, 184515 (2005).

[251] Z. B. Tan, D. Cox, T. Nieminen, P. Lähteenmäki, D. Golubev, G. B. Lesovik, and P. J. Hakonen, Cooper Pair Splitting by Means of Graphene Quantum Dots, Phys. Rev. Lett. **114**, 096602 (2015).

[252] G. Fülöp, F. Domínguez, S. d'Hollosy, A. Baumgartner, P. Makk, M. H. Madsen, V. A. Guzenko, J. Nygård, C. Schönenberger, A. Levy Yeyati, and S. Csonka, Magnetic Field Tuning and Quantum Interference in a Cooper Pair Splitter, Phys. Rev. Lett. **115**, 227003 (2015).

[253] L. Hofstetter, S. Csonka, J. Nygård, and C. Schönenberger, Cooper pair splitter realized in a two-quantum-dot Y-junction, Nature **461**, 960 (2009).

[254] L. Hofstetter, S. Csonka, A. Baumgartner, G. Fülöp, S. d'Hollosy, J. Nygård, and C. Schönenberger, Finite-Bias Cooper Pair Splitting, Phys. Rev. Lett. **107**, 136801 (2011).

[255] J. Schindele, A. Baumgartner, and C. Schönenberger, Near-Unity Cooper Pair Splitting Efficiency, Phys. Rev. Lett. **109**, 157002 (2012).

[256] L. G. Herrmann, F. Portier, P. Roche, A. L. Yeyati, T. Kontos, and C. Strunk, Carbon Nanotubes as Cooper-Pair Beam Splitters, Phys. Rev. Lett. **104**, 026801 (2010).

[257] I. V. Borzenets, Y. Shimazaki, G. F. Jones, M. F. Craciun, S. Russo, M. Yamamoto, and S. Tarucha, High Efficiency CVD Graphene-lead (Pb) Cooper Pair Splitter, Sci. Rep. **6**, 23051 (2016).

[258] P. Pandey, R. Danneau, and D. Beckmann, Ballistic Graphene Cooper Pair Splitter, Phys. Rev. Lett. **126**, 147701 (2021).

[259] G.-H. Park, K. Watanabe, T. Taniguchi, G.-H. Lee, and H.-J. Lee, Engineering Crossed Andreev Reflection in Double-Bilayer Graphene, Nano Lett. **19**, 9002 (2019).

[260] A. G. Moghaddam and M. Zareyan, Long-range Josephson coupling through ferromagnetic graphene, Phys. Rev. B **78**, 115413 (2008).

[261] J. Martin, N. Akerman, G. Ulbricht, T. Lohmann, J. H. Smet, K. von Klitzing, and A. Yacoby, Observation of electron–hole puddles in graphene using a scanning single-electron transistor, Nat. Phys. **4**, 144 (2008).

[262] J. Xue, J. Sanchez-Yamagishi, D. Bulmash, P. Jacquod, A. Deshpande, K. Watanabe, T. Taniguchi, P. Jarillo-Herrero, and B. J. LeRoy, Scanning tunnelling microscopy and spectroscopy of ultra-flat graphene on hexagonal boron nitride, Nat. Mater. **10**, 282 (2011).

[263] Y.-L. Yang, C. Bai, and X.-D. Zhang, Crossed Andreev reflection in graphene-based ferromagnet-superconductor structures, The European Physical Journal B **72**, 217 (2009).

[264] W.-T. Lu and Q.-F. Sun, Electrical control of crossed Andreev reflection and spin-valley switch in antiferromagnet/superconductor junctions, Phys. Rev. B **104**, 045418 (2021).

[265] R. Horodecki, P. Horodecki, M. Horodecki, and K. Horodecki, Quantum entanglement, Rev. Mod. Phys. **81**, 865 (2009).

Paper [1]

Martin F. Jakobsen, Alireza Qaiumzadeh, and Arne Brataas

"Scattering theory of transport through disordered magnets"

Scattering theory of transport through disordered magnets

Martin F. Jakobsen ⬤, Alireza Qaiumzadeh, and Arne Brataas ⬤

Center for Quantum Spintronics, Department of Physics, Norwegian University of Science and Technology, NO-7491 Trondheim, Norway

We present a scattering theory of transport through noncollinear disordered magnetic insulators. For concreteness, we study and compare the random field model (RFM) and the random anisotropy model (RAM). The RFM and RAM are used to model random spin disorder systems and amorphous materials, respectively. We utilize the Landauer-Büttiker formalism to compute the transmission probability and spin conductance of one-dimensional disordered spin chains. The RFM and the RAM both exhibit Anderson localization, which means that the transmission probability and spin conductance decay exponentially with the system length. We define two localization lengths based on the transmission probability and the spin conductance, respectively. Next, we numerically determine the relationship between the localization lengths and the strength of the disorder. In the limit of weak disorder, we find that the localization lengths obey power laws and determine the critical exponents. Our results are expressed via the universal exchange length and are therefore expected to be general.

I. INTRODUCTION

In magnonics [1–8], the primary focus has recently been on the propagation of spin waves through various types of magnetic insulators. A particular emphasis has been on ordered systems, such as (anti)ferromagnets, and ferrimagnets. An advantage is that the spin current may suffer less Joule heating compared to electric currents, making insulator-magnonics applications potentially much more energy efficient [3,9]. Numerous successful experiments have generated and manipulated spin currents using the spin-Hall effect and the inverse spin-Hall effect [10]. A common experimental setup consists of sandwiching a magnetic insulator between two conductors and using the spin-Hall effect to generate a spin current in the left conductor that propagates through the magnetic insulator and into the right conductor. The spin current in the right conductor is converted into a charge current via the inverse spin-Hall effect. This provides a useful method to measure the spin current and infer the spin-transport properties of the magnetic insulator [11–25].

A class of materials that has recently attracted attention in the spintronics community is disordered magnetic insulators [26–31]. Notably, a recent experiment claimed that a spin current flowing through a sample of amorphous yttrium-iron-garnet could travel tens of micrometers [32]. This distance is comparable to the spin current propagation length in a crystalline (anti)ferromagnet [25,33]. More generally, it is crucial to study disordered magnetic materials because almost all materials contain some degree of disorder, which will affect the functional properties of magnonic devices. When the disorder is sufficiently strong, the eigenstates become trapped in a finite spatial region, completely suppressing the transport properties. This phenomenon is known as Anderson localization, and the first discussion of this phenomenon in magnetic systems began in the 1960s [34–42]. Furthermore, it has been shown that, even with a small onset of disorder, the transport properties change from conductive to diffusive

[29,43], which has important consequences for magnonics applications in low dimensions.

The common sources of quenched disorder in magnetic insulators are (i) randomness due to anisotropies, local fields, and amorphous structure and (ii) frustration due to competing long-range exchange interactions. In this paper we focus on magnetic insulators with quenched disorder due to (i). Two models with these properties are the random field model (RFM) and the random anisotropy model (RAM), where the disorder is caused by the competition between the exchange interaction and the coupling to local random fields and anisotropies, respectively. The RFM and RAM is used to model quenched spin disorder and amorphous magnets, respectively [44–49]. Experimental realizations of such systems are plentiful [50–54].

Furthermore, there are two types of RFM/RAM spin models. The first is the Ising model, where the spins are scalars $S_i = \pm 1$ and are randomly pointing either parallel or antiparallel to each other in the ground state [55–62]. The second type is the Heisenberg model, where the spins are vectors $\mathbf{S}_i$ that in the ground state are pointing noncollinearly in random directions [63–68].

Because the ground state in the RFM/RAM Ising model is relatively simple, it can often be studied efficiently with analytical methods. For example, one can either solve the equations of motion by a transfer matrix approach paralleling Anderson's celebrated work on disordered fermionic systems [69,70] or one can use field-theory methods, particularly the replica trick, replica symmetry breaking, and mean-field theory [54,71,72]. Although the RFM/RAM Ising models are analytically accessible, they are only simplified idealizations of a real disordered magnet where the spins are noncollinear. In this work, we wish to focus on systems with noncollinear spins that are harder to describe analytically but exhibit more realistic spin-wave dynamics.

Disordered magnetic insulators with a noncollinear ground state are a notoriously difficult system to describe. Due to their

complexity, it is often useful to study the classical spin waves of the system. Our work is related to a recent study [29,73] in which the micromagnetic Landau-Lifshitz-Gilbert (LLG) equation was solved using a quasimonochromatic Gaussian wave packet as the initial condition. They found that the width of the wave packet increases in time until it saturates around the localization length of the system, which is a hallmark of Anderson localization. In systems that exhibit Anderson localization, the localization length decreases as the system becomes more disordered. However, the exact relationship between the localization length and the strength of disorder is far from being well established in noncollinear disordered magnetic insulators. In this work, we attempt to shed some light on these issues.

The localization effect in spin models depends on the dimensionality of the system, similar to disordered fermionic systems [74]. For fermionic systems in one dimension, there is Anderson localization; in two dimensions, the effect remains present but much weaker, while in three dimensions, there is the possibility of both a localized and a delocalized phase. The same observations have been established for disordered magnets [50,75]. We focus on one-dimensional spin chains. With more computational time, this method can also be applied to two- and three-dimensional systems.

The numerical method that we develop is based on the Landauer-Büttiker formalism [76,77], which has proven to be extremely useful in studying the transport properties of electronic systems. To the best of our knowledge, such a method has not previously been applied to the RFM/RAM Heisenberg model. In this paper, we investigate the effect of Anderson localization on the spin-wave transport properties of a disordered magnetic insulator. To this end, we first determine the relationship between the system size and the transmission probability for different strengths of disorder and then calculate the spin conductance. With this knowledge, we can investigate how the localization length of the system scales with the strength of the disorder. In particular, we calculate and compare the critical exponents of the RFM and the RAM. These quantities provide us with direct insights into how the transport properties of the spin waves are affected by the localization phenomenon that is present due to quenched disorder.

We hope that this theoretical investigation may inspire an experimental investigation into the transport properties of disordered magnetic nanowires [78–82]. In particular, it would be interesting to compare the experimental relationship between the localization length and strength of disorder to the critical exponents that we determine in this work.

The paper is organized as follows. In Sec. II, we introduce the RFM and the RAM Hamiltonians and discuss their ground state. In Sec. III we find the linearized equations of motion, and derive expressions for the spin current and the spin conductance. Section IV contains our numerical calculations of the scattering properties of the system. In Sec. IV we summarize our results.

II. THEORETICAL MODEL

In this section we carefully introduce the model we are interested in studying. We start by presenting the Hamiltonians
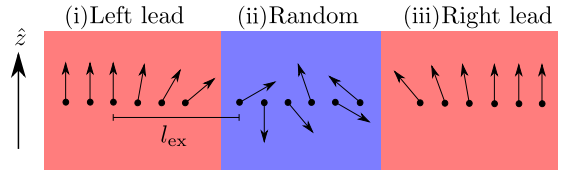

FIG. 1. Disordered magnet (blue) is sandwiched between two ferromagnets (red). In regions (*i*) and (*iii*), $\mathbf{n}_i = \hat{z}$, while in region (*ii*) $\mathbf{n}_i$ is uniformly distributed on the unit sphere. Consequently, the spins in region (*ii*) point in random directions, while the spins deep inside regions (*i*) and (*iii*) point in the z direction. The spins close to the two interfaces rotate similar to the spins in a domain wall. The length of the domain-wall-like region is illustrated and given by the exchange length $l_{\mathrm{ex}} = \sqrt{J/K}d$.

for the RFM and the RAM, and introduce the geometry. We conclude this section by presenting a method to calculate the classical metastable states.

A. Hamiltonian

To investigate the transport properties of one-dimensional disordered noncollinear spin chains, we use the Hamiltonian

$$H^\kappa = -J \sum_i \mathbf{S}_i \cdot \mathbf{S}_{i+1} - K \sum_i (\mathbf{S}_i \cdot \mathbf{n}_i)^{\kappa+1}, \qquad (1)$$

where $\kappa = 0$ and $\kappa = 1$ represent the RFM and the RAM, respectively.

The dimensionless spins $\mathbf{S}_i$ are attached to a one-dimensional lattice with lattice spacing d. The exchange interaction with $J > 0$ attempts to align the spins. The terms proportional to K encapsulate the quenched disorder of the system, and we choose $K > 0$ without loss of generality. Each spin $\mathbf{S}_i$ is coupled to a local random vector $\mathbf{n}_i$. The competition between the exchange and the random interactions in Eq. (1) results in a noncollinear disordered ground state. We use the parameter K/J to characterize the strength of disorder.

B. Geometry

We consider a one-dimensional chain with N lattice sites. The chain is split into three regions that we call (*i*) the left lead, (*ii*) the random region, and (*iii*) the right lead; see Fig. 1.

In regions (*i*) and (*iii*), we let the number of spins be equal to N_{L} and N_{R}, respectively. In addition, we let $\mathbf{n}_i$ point in the $\hat{z}$ direction. In region (*ii*), we let the number of spins be equal to N_{rand} and $\mathbf{n}_i$ point in some random direction uniformly distributed on the unit sphere. Note that far away from the random region (deep inside of the leads), the spins point in the $\hat{z}$ direction, while in the random region, the spins are oriented randomly. In the regions close to the interface, the spins are rotating in a domain-wall-like fashion. The length of this domain-wall region is given by the exchange length $l_{\mathrm{ex}} = \sqrt{J/K}d$.

The scattering problem that we are interested in studying can now be realized by exciting coherent spin waves in the left lead propagating towards the random region. As the spin wave approaches the random region, it will be scattered either back into the left lead (reflection) or into the right lead

(transmission). We assume semi-infinite leads such that N_L and $N_R \to \infty$.

C. Ground state

Determining the true ground state of a disordered magnet (collinear or noncollinear) is a very challenging problem. The primary reason is that the randomness results in free energy with many nearly degenerate minima, separated by high energy barriers. The problem of determining the exact ground state of disordered systems is its own research field, and we do not wish to address that problem here [83–94]. However, due to the high energy barriers, the probability of tunneling between different metastable states is small. Hence, in an experiment, the disordered magnet becomes trapped in a state that may differ from the exact ground state when the system is cooled down, depending on the history. Thus, in this paper, we study the transport properties of disordered magnets around classical metastable states.

We can find a classical metastable state of the system by treating the spins as classical vectors obeying the LLG equation of the form

$$\frac{d\mathbf{S}_i}{dt} = -\gamma \mathbf{S}_i \times \mathcal{H}_i^\kappa - \lambda \mathbf{S}_i \times (\mathbf{S}_i \times \mathcal{H}_i^\kappa). \quad (2)$$

Here, the first term with $\gamma > 0$ describes the spin $\mathbf{S}_i$ precessing around its instantaneous effective field $\mathcal{H}_i^\kappa = -\delta H^\kappa / \delta \mathbf{S}_i$, while the second term describes the damping towards the direction of the instantaneous effective field. The metastable state is then obtained by specifying some arbitrary initial configuration and allowing the spins to evolve according to this equation for sufficiently long times $t \to \infty$.

III. SCATTERING THEORY

In this section we outline the theoretical approach that we will use to determine the transport properties of the RFM and the RAM. We start by determining the linearized equations of motion, and formulate the scattering problem. Finally, we derive the expressions for the spin current and spin conductance in the linear response regime.

A. Hamiltonian in terms of spin-wave operators

To study the transport properties of the system, we can perform a Holstein-Primakoff expansion around one of the metastable states. Let us at each site i define a local coordinate system $\{\hat{e}_x(i), \hat{e}_y(i), \hat{e}_z(i)\}$ such that $\hat{e}_z(i)$ is parallel to the spin at site i in the ground state. The spin operator in a low-lying excited state can then be written as

$$\mathbf{S}_i = \hat{e}_z(i)S_i^z + \hat{e}_x(i)S_i^x + \hat{e}_y(i)S_i^y. \quad (3)$$

We perform a Holstein-Primakoff transformation of the form

$$S_i^x \approx \sqrt{\frac{S}{2}}(a_i + a_i^\dagger), \quad (4a)$$

$$S_i^y \approx -i\sqrt{\frac{S}{2}}(a_i - a_i^\dagger), \quad (4b)$$

$$S_i^z = S - a_i^\dagger a_i. \quad (4c)$$

In Eq. (4), we have only included the lowest-order terms because we are not interested in studying the interactions between the spin waves. If we substitute Eqs. (3) and (4) into Eq. (1) and introduce the notations $\hat{e}_\pm(i) = \hat{e}_x(i) \pm i\,\hat{e}_y(i)$ and $n_i^\pm = n_i^x \pm in_i^y$, we obtain a Hamiltonian of the form

$$H^\kappa = \sum_{ij} A_{ij}^\kappa a_i^\dagger a_j + B_{ij}^\kappa a_i a_j + \text{H.c.}, \quad (5)$$

where

$$
\begin{aligned}
A_{ij}^\kappa = \delta_{i,j} \Bigg\{ & JS\,\hat{e}_z(i)\hat{e}_z(i+1) + \frac{1}{2}Kn_i^z \\
& + \kappa \left[KS(n_i^z)^2 - \frac{1}{2}KSn_i^- n_i^+ - \frac{1}{2}Kn_i^z \right] \Bigg\} \\
& - \frac{JS}{2}\delta_{i,j+1}\hat{e}_-(i)\hat{e}_+(j),
\end{aligned}
$$

$$B_{ij}^\kappa = -\kappa\frac{KS}{2}(n_i^-)^2\delta_{i,j} - \frac{JS}{2}\hat{e}_-(i)\hat{e}_-(i+1)\delta_{i,j+1}. \quad (6)$$

In the following, we will study the spin waves associated with the Hamiltonian of Eq. (5).

B. Equations of motion

The equations of motion for the spin-wave operators can now be calculated from the Heisenberg equation

$$\frac{d}{dt}a_i^\pm = \frac{i}{\hbar}[H^\kappa, a_i^\pm]. \quad (7)$$

For clarity, we reinstate the spin operators $\{S_i^x, S_i^y\}$ using Eq. (4) and cast the equation of motion in the form

$$
\begin{aligned}
\hbar\frac{dS_j^x}{dt} = JS\Big\{ & \hat{e}_z(j)[\hat{e}_z(j+1) + \hat{e}_z(j-1)]S_j^y \\
& - \hat{e}_y(j-1)\hat{e}_y(j)S_{j-1}^y - \hat{e}_x(j-1)\hat{e}_y(j)S_{j-1}^x \\
& - \hat{e}_y(j)\hat{e}_y(j+1)S_{j+1}^y - \hat{e}_y(j)\hat{e}_x(j+1)S_{j+1}^x \Big\} \\
& + Kn_j^z S_j^y + \kappa\big\{2KS(n_j^z)^2 S_j^y - 2KS(n_j^y)^2 S_j^y \\
& - 2KSn_j^x n_j^y S_j^x - Kn_j^z S_j^y \big\},
\end{aligned} \quad (8)
$$

$$
\begin{aligned}
\hbar\frac{dS_j^y}{dt} = JS\Big\{ & -\hat{e}_z(j)[\hat{e}_z(j+1) + \hat{e}_z(j-1)]S_j^x \\
& + \hat{e}_x(j-1)\hat{e}_x(j)S_{j-1}^x + \hat{e}_y(j-1)\hat{e}_x(j)S_{j-1}^y \\
& + \hat{e}_x(j)\hat{e}_x(j+1)S_{j+1}^x + \hat{e}_x(j)\hat{e}_y(j+1)S_{j+1}^y \Big\} \\
& - Kn_j^z S_j^x - \kappa\big\{2KS(n_j^z)^2 S_j^x \\
& - 2KS(n_j^x)^2 S_j^y - 2KSn_j^x n_j^y S_j^y + Kn_j^z S_j^y \big\}.
\end{aligned} \quad (9)
$$

Equations (8) and (9) are identical to the linearized classical Landau-Lifshitz equations expressed in the local coordinate system $\{\hat{e}_x(j), \hat{e}_y(j), \hat{e}_z(j)\}$. Since we are only interested in studying how the intrinsic disorder affects the transport properties of the system, we have not included a Gilbert damping term.

C. Scattering problem and solution Ansatz

Equations (8) and (9) can be solved numerically in the classical regime, where we treat the spin operators as classical vectors. The spin-wave solutions are the normal modes of the system and precess with the same frequency ω. Therefore, we can factorize out the time dependence of the spin operators as $e^{-i\omega t}$.

Deep inside the leads, the spins at neighboring sites are pointing in the z direction; see Fig. 1. This considerably simplifies the equations of motion in the leads:

$$
\begin{aligned}
-i\hbar\omega S_j^x &= JS\left(2S_j^y - S_{j-1}^y - S_{j+1}^y\right) \\
&\quad + K[1 + \kappa(2S-1)]S_j^y, \\
-i\hbar\omega S_j^y &= JS\left(-2S_j^x + S_{j-1}^x + S_{j+1}^x\right) \\
&\quad - K[1 + \kappa(2S-1)]S_j^x.
\end{aligned}
\tag{10}
$$

The system behaves as a ferromagnet with an external field or intrinsic anisotropy in the z direction. The solutions are therefore circularly polarized plane waves traveling with a fixed wave number q and frequency ω. The dispersion relation can be determined by substituting the *Ansätze* $S_x^j = e^{iqjd}$ and $S_y^j = -i\,e^{iqjd}$ into Eq. (10). The result is

$$
\epsilon = \hbar\omega = 2JS(1 - \cos qd) + K[1 + \kappa(2S-1)].
\tag{11}
$$

Let us now formulate the scattering problem. Deep inside the regions (*i*) and (*iii*) in Fig. 1, we know that the solution must have the form

$$
S_j^x = e^{iqjd} + r_x e^{-iqjd}, \quad S_j^y = -i(e^{iqjd} + r_y e^{-iqjd})
\tag{12}
$$

and

$$
S_j^x = t_x e^{iqjd}, \quad S_j^y = -it_y e^{-iqjd},
\tag{13}
$$

respectively. Inside region (*ii*), we know that the spin components must satisfy Eqs. (8) and (9). Using the *Ansätze* as boundary conditions, we have found a finite set of algebraic equations that we can solve numerically to determine the reflection and transmission amplitudes $\{r_x, r_y, t_x, t_y\}$ as functions of ϵ.

D. Spin current and conductance

Once we know the reflection and transmission amplitude, we can calculate the spin conductance of the disordered magnet utilizing the Landauer-Büttiker formalism in the linear response regime. In this section, we derive the expression for spin conductance.

In the leads, the Hamiltonian in Eq. (5) simplifies to

$$
\begin{aligned}
H^\kappa &= \sum_i \{2JS + K[1 + \kappa(2S-1)]\}a_i^\dagger a_i \\
&\quad - JS(a_j a_{j+1}^\dagger + a_j^\dagger a_{j+1}).
\end{aligned}
\tag{14}
$$

From the equation of motion,

$$
\begin{aligned}
\frac{d}{dt}N_i &= \frac{i}{\hbar}[N_i, H^\kappa] \\
&= -iJS\{(a_{j+1}^\dagger a_j - a_j^\dagger a_{j+1}) + (a_{j-1}^\dagger a_j - a_j^\dagger a_{j-1})\},
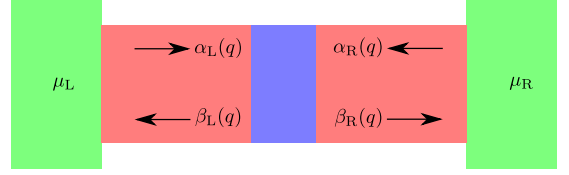\end{aligned}
\tag{15}
$$

FIG. 2. Disordered magnet (blue) is sandwiched between two ferromagnetic leads (red). The leads are connected to two spin reservoirs (green) with spin accumulations μ_L and μ_R. The reservoirs are in thermodynamic equilibrium such that the magnon population is characterized by the Bose-Einstein distribution. A spin current is induced when there is a nonzero spin bias $\delta\mu = \mu_L - \mu_R$.

where $N_i = a_i^\dagger a_i$ is the number operator, and we can extract the spin current from site j to $j + 1$ as

$$
I_{j,j+1} = iJS(a_{j+1}^\dagger a_j - a_j^\dagger a_{j+1}).
\tag{16}
$$

Now consider the situation in Fig. 2, where two reservoirs in thermodynamic equilibrium are attached to two leads with a scattering region between them. If the spin accumulation in the left reservoir μ_L is greater than the spin accumulation in the right reservoir μ_R, the spin current in Eq. (16) will flow from the left to the right reservoir. We define the operators $\alpha_{L,R}(q)$ and $\beta_{L,R}(q)$ injecting and removing magnons with wave numbers q into the leads, respectively. The relationship between these operators is given by the scattering matrix

$$
\begin{pmatrix} \beta_L(q) \\ \beta_R(q) \end{pmatrix} = \begin{pmatrix} r & t' \\ t & r' \end{pmatrix} \begin{pmatrix} \alpha_L(q) \\ \alpha_R(q) \end{pmatrix},
\tag{17}
$$

where r (r') and t (t') are the reflection and transmission amplitudes, respectively, for a spin wave originating from the left (right) lead.

In the left lead, we can express a_j as [95]

$$
a_j = \int_0^{\pi/d} \frac{dq}{2\pi/d}[e^{iqjd}\alpha_L(q) + e^{iqjd}\beta_L(q)].
\tag{18}
$$

If we substitute Eq. (18) and its complex conjugate into Eq. (16) and utilize that the leads are in thermal equilibrium with the reservoirs such that $\langle \alpha_{L,R}^\dagger(q_1)\alpha_{L,R}(q_2)\rangle = \frac{2\pi}{d}\delta(q_1 - q_2)f_{L,R}(q_1)$, we find that

$$
\langle I_{j,j+1}\rangle = \frac{1}{2\pi}\int_{\epsilon_{\min}}^{\epsilon_{\max}} d\epsilon\, T(\epsilon)[f_L(\epsilon) - f_R(\epsilon)].
\tag{19}
$$

In this expression, $f_{L,R}(\epsilon)$ represents the Bose-Einstein distributions in the left and right reservoirs, respectively, and $T(\epsilon) = |t|^2$. The integration limits are obtained from Eq. (11).

Assume that the spin accumulation in the left lead is $\mu_L = \mu + \delta\mu$ and that the spin accumulation in the right lead is $\mu_R = \mu$, where $\delta\mu/\mu \ll 1$. We find that, in the linear response, the spin conductance is given by

$$
G = \frac{1}{2\pi}\int_{\tilde\epsilon_{\min}}^{\tilde\epsilon_{\max}} d\tilde\epsilon\, T(\tilde\epsilon)\left(-\frac{df}{d\tilde\epsilon}\right).
\tag{20}
$$

This result can also be derived using Green's functions [96]. In Eq. (20), we are integrating over the dimensionless energies $\tilde\epsilon = \epsilon/J$. Energies outside of the integration interval result in
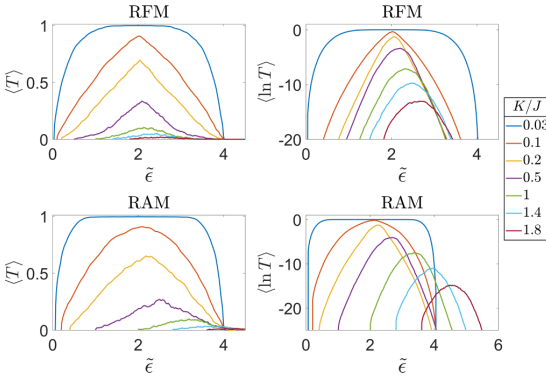
FIG. 3. Behaviors of $\langle T \rangle$ and $\langle \ln T \rangle$ as a function of $\tilde{\epsilon}$ and K/J.

the spin waves in Eqs. (12) and (13) becoming evanescent waves that do not contribute to the spin conductance.

IV. RESULTS AND DISCUSSION

For each realization of the system, we find that $r_x = r_y \equiv r$ and that $t_x = t_y \equiv t$, reflecting the fact that, inside the leads, the spin waves are circularly polarized. Furthermore, we define $R = |r|^2$ and $T = |t|^2$ as the reflection and transmission probabilities, respectively, and find that $R + T = 1$. Since R and T depend on the realization of the system, we must perform an ensemble average $\langle \ldots \rangle$ to obtain physically meaningful quantities. In our calculations, we used 10^3 different realizations for the random vectors $\mathbf{n}_i$. In Fig. 3, we plotted $\langle T \rangle$ and $\langle \ln T \rangle$ as a function of $\tilde{\epsilon}$ for different values of K/J and a fixed system length $L = N_{\text{rand}} d$. In the remainder of this paper we set $d = 1$ for convenience.

A. Transmission probability

As the system becomes more disordered, the transmission probability decreases for both the RFM and the RAM. However, Fig. 3 demonstrates that the quantitative behavior of the localization is significantly different in the two models. In both models, as K/J increases, the maxima $\langle T \rangle_{\text{max}}$ and $\langle \ln T \rangle_{\text{max}}$ shift towards higher $\tilde{\epsilon}$, but in the RAM, this shift is greater than that in the RFM. In addition, the peak in the transmission probability is wider in the RAM compared to the RFM for small K/J. Thus a broader range of spin waves can pass through the RAM compared to the RFM in the limit of weak disorder.

We can understand the difference in width from the Hamiltonian in Eq. (1). In the RAM, the term causing disorder is $(\mathbf{S}_i \cdot \mathbf{n}_i)^2$; thus the spin $\mathbf{S}_i$ wants to point either parallel or antiparallel to $\mathbf{n}_i$. The spin is also coupled to its neighbors through the exchange interaction. Therefore, in the RAM, whether the spin $\mathbf{S}_i$ chooses to point parallel or antiparallel to $\mathbf{n}_i$ depends on the neighboring spins. Meanwhile, in the RFM, the term causing disorder is $\mathbf{S}_i \cdot \mathbf{n}_i$, and the spin wants to only point parallel to $\mathbf{n}_i$. The ability to select whether to point parallel or antiparallel to $\mathbf{n}_i$ leads to the spin chains in the RAM being less disordered than the spin chains in the
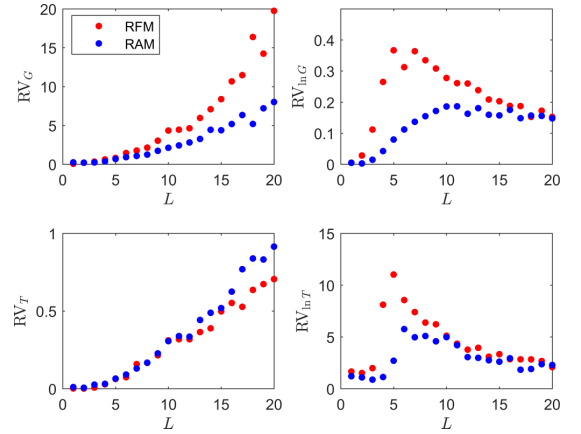
RFM, which in turn leads to a broader peak in the transmission probability.

FIG. 4. Length dependence of the relative variances RV_G, $\text{RV}_{\ln G}$, RV_T, and $\text{RV}_{\ln T}$ for the RFM and the RAM. The strength of disorder is $K/J = 0.4$.

B. Self-averaging

In disordered systems, certain quantities are not self-averaging in the thermodynamic limit. This is well known in disordered fermionic systems and is expected to be a general feature of a broad spectrum of disordered systems [97]. A test to determine whether a quantity O is self-averaging is to check whether the relative variance $\text{RV}_O = \text{Var}(O)/\langle O \rangle^2$ vanishes (or is sufficiently small) in the limit $L \to \infty$. For the fermionic 1D Anderson model with on-site disorder, one finds that the transmission probability and hence the conductance are not self-averaging [98]. In two and three dimensions, one finds that the logarithms $\ln(T)$, $\ln(G)$ are self-averaging such that $\text{RV}_{\ln G} \sim L^{-D}$ ($D = 2, 3$) [97,99]. In one dimension at finite temperature, one finds that $\ln G$ is only marginally self-averaging because $\text{RV}_{\ln G}$ decays logarithmically with L [99–101].

As expected, we find similar results in this work. Figure 4 shows that the relative variances RV_T and RV_G increase with the length of the system. In addition, the relative variances $\text{RV}_{\ln T}$ and $\text{RV}_{\ln G}$ decrease with the length of the system. Hence, as the length of the system increases, the fluctuations in T and G become much greater than the corresponding expectation values, meaning that they are not representative variables in the thermodynamic limit. Therefore, we use $\{\ln(T), \ln(G)\}$, rather than $\{T, G\}$, to calculate the localization lengths of the system.

C. Localization length

In this work, it is natural to define two types of localization lengths. The first is based on the maximum of the transmission amplitude $\langle \ln T \rangle_{\text{max}}$ in Fig. 3. The second is based on the conductance $\langle \ln G \rangle$. We refer to these localization lengths as $\tilde{L}_{\ln T}$ and $\tilde{L}_{\ln G}$, respectively.
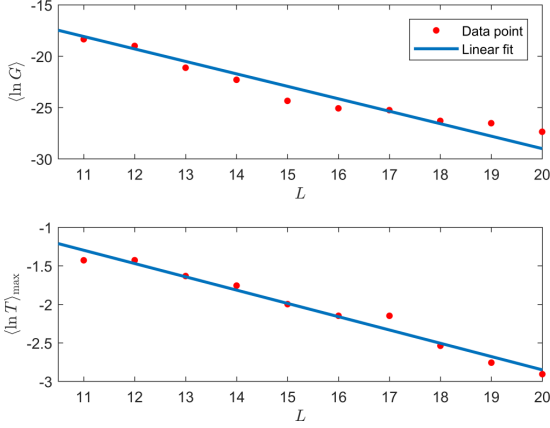
FIG. 5. Length dependence of $\langle \ln G \rangle$ and $\langle \ln T \rangle_{\max}$ for the RFM can be approximated with a linear fit. The strength of disorder is $K/J = 0.4$ and the temperature is $\tilde{T} = 0.05$.

In Fig. 5, we plotted $\langle \ln T \rangle_{\max}$ and $\langle \ln G \rangle$ as a function of the system length L for a fixed K/J and temperature $\tilde{T} = kT/J$. We have performed a curve fit with the functions

$$\langle \ln T \rangle_{\max} = \frac{L}{\tilde{L}_{\ln T}} + A \tag{21}$$

and

$$\langle \ln G \rangle = \frac{L}{\tilde{L}_{\ln G}} + B \tag{22}$$

such that the localization length can be extracted as the gradient of the straight lines in Fig. 5. In this particular case, we found a coefficient of determination R^2 with the value $R^2 = 0.95$ indicating a good fit. To determine the localization lengths as a function of K/J, we performed straight line curve fits for graphs such as those found in Fig. 5 but with different K/J and $\tilde{T}$. In all cases, we found that the coefficient of determination was in the range $(0.9,1)$ and that the average coefficient was $\langle R^2 \rangle = 0.95$, indicating reasonably good straight-line fits. By then calculating the gradient of these straight lines, we can estimate the localization lengths as a function of K/J.

1. Localization length from transmission

In Fig. 6, we plot the localization length $\tilde{L}_{\ln T}$ and the 95%-confidence interval for the RAM and RFM, respectively. In both cases, we have performed a curve fit with the function

$$\tilde{L}_{\ln T} = \eta \left(\frac{K}{J} \right)^{\nu} + \xi. \tag{23}$$

The parameters (with confidence intervals) are displayed in Table I. Similar to fermionic systems [102], we find that the localization length decays monotonically as a power law as we increase the strength of disorder. Our result can be made more universal by introducing the exchange length such that

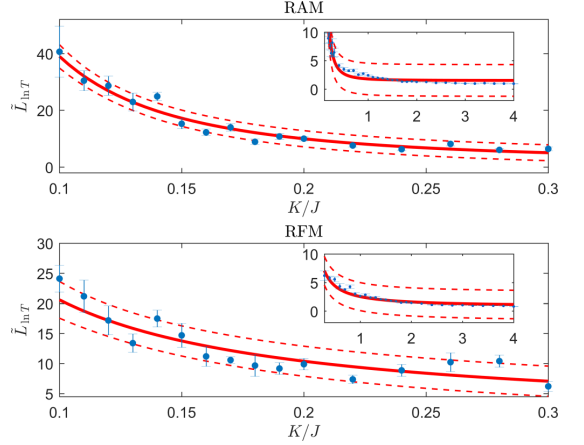$$\tilde{L}_{\ln T} = \eta (l_{\text{ex}})^{-2\nu} + \xi. \tag{24}$$

FIG. 6. Behavior of $\tilde{L}_{\ln T}$ as a function of K/J for the RAM and the RFM, respectively. The line represents the numerical fit in Eq. (23), the dashed lines represent the 95% confidence interval, and the points with error bars represent the localization length calculated from Eqs. (8) and (9) with standard error.

Note that, for weak disorder, the localization length is greater in the RAM than in the RFM. This is a consequence of the fact that the spin chains are less disordered in the RAM compared to the RFM, as we discussed at the end of Sec. IV A.

2. Localization length from conductance

In Fig. 7, we plot $\tilde{L}_{\ln G}$ as a function of K/J for different temperatures $\tilde{T}$. There is an interval $K/J \approx (0.5, 2)$ where the localization length increases for small $\tilde{T}$. Furthermore, for sufficiently large $\tilde{T}$, this interval vanishes such that the localization length decays monotonically for all K/J. This nontrivial behavior arises because there is a competition between the temperature dependence of the broadening function $-df/d\tilde{\epsilon}$ and the disorder dependence of the transmission probability $T(\tilde{\epsilon})$ in Eq. (20). As the temperature increases, the broadening function excites an increasing number of magnons, which in turn leads to a greater conductance. Meanwhile, as the system becomes more disordered, the transmission probability $T(\tilde{\epsilon})$ decreases, resulting in a smaller conductance. On the interval $K/J \approx (0.5, 2)$, the increase in conductance due to temperature is greater than the decrease in conductance due to disorder, which results in an increase in localization length. Furthermore, in this interval, the localization length is comparable to the lattice spacing d, which means that there

TABLE I. Numerical values of the parameters in Eq. (23) for the RFM and the RAM. The brackets $(\dots)$ give the 95% confidence interval.

	RFM	RAM
η	1.3 (0.7, 2.0)	0.2 (0.1, 0.3)
ν	−1.2 (−1.4, −1.0)	−2.2 (−2.4, −2.0)
ξ	1.1 (0.3, 1.9)	1.6 (1.0, 2.1)
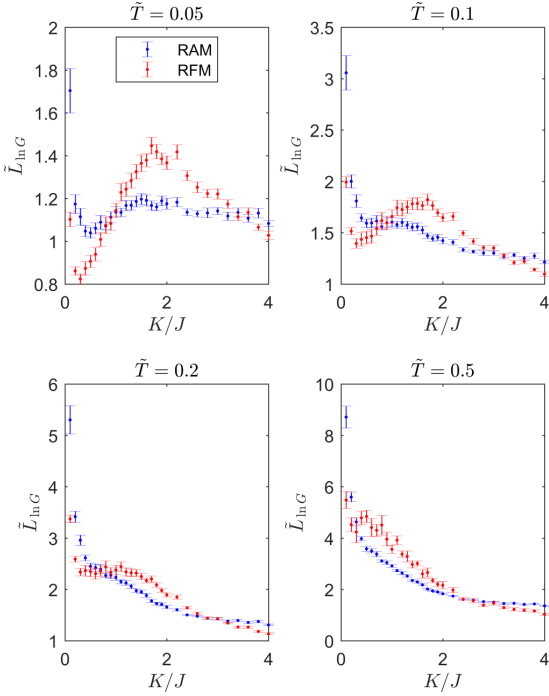
FIG. 7. Temperature dependence of $\tilde{L}_{\ln G}$ for strongly disordered magnetic insulators.

FIG. 8. Temperature dependence of $\tilde{L}_{\ln G}$ in the limit of weak disorder $K/J \to 0$.

may be complicated microscopic details of the model that may further enhance this effect.

Due to the complicated temperature and disorder dependence, it is numerically challenging to determine a closed formula such as the one in Eq. (23) for the localization length $\tilde{L}_{\ln G}$. However, in the weak-disorder limit $K/J \to 0$, it is reasonable to assume that the localization length decays as a power law of the form

$$L_{\ln G} \sim \left(\frac{K}{J}\right)^{\gamma} = (l_{\mathrm{ex}})^{-2\gamma}, \tag{25}$$

where γ is the critical exponent. Figure 8 shows the result of such a curve fit for the RFM and the RAM for different temperatures. The corresponding critical exponents γ_{RFM} and γ_{RAM} are given in Table II.

In our simulations, we kept the temperature below the Curie temperature $\tilde{T} = 1$, where the temperature fluctuations

TABLE II. Numerical values of the critical exponent for the RFM and the RAM for different temperatures. The brackets (. . .) provide the 95% confidence interval.

$\tilde{T}$	γ_{RFM}	γ_{RAM}
0.05	$-3.8\,(-4.3, -3.4)$	$-1.9\,(-2.3, -1.6)$
0.1	$-3.7\,(-4.2, -3.2)$	$-1.7\,(-2.0, -1.4)$
0.2	$-3.6\,(-4.1, -3.1)$	$-1.3\,(-1.6, -1.0)$
0.5	$-3.3\,(-3.8, -2.8)$	$-0.7\,(-1.0, -0.4)$

of the spins are negligible. For temperatures $\tilde{T} \approx 1$, there will be additional temperature-induced disorder. This issue has previously been investigated [73,103,104] by including a temperature-dependent stochastic field in the effective field $\mathcal{H}_i^{\kappa}$ in Eq. (2), and it was found that temperature fluctuations shorten the localization length and enhance the Anderson localization.

V. SUMMARY AND CONCLUSIONS

In this paper, we have applied the Landauer-Büttiker formalism to noncollinear disordered magnetic insulators. We have considered both amorphous magnets and magnets with spin disorder modeled by the RAM and the RFM, respectively. We calculated the self-averaging quantities $\langle \ln T \rangle$ and $\langle \ln G \rangle$ as a function of system length L for a broad range of disorder strengths K/J. Consistent with the literature, we found evidence for Anderson localization such that $\langle \ln T \rangle$ and $\langle \ln G \rangle$ were linear functions of the system length L. This allowed us to define two localization lengths $\tilde{L}_{\ln G}$ and $\tilde{L}_{\ln T}$ based on the conductance and the maximum transmission probability, respectively. In the limit of weak disorder, the localization lengths obeyed power laws, and we calculated the relevant critical exponents. We expect our results to be general because they are expressed through the universal exchange length l_{ex}.

We found that the Anderson localization is more prominent in the RFM than in the RAM. The reason for this result is that the competition between the exchange interaction and the disorder term leads to more disordered spin chains in the RFM

than in the RAM. The spin chains in the RAM are less disordered because the disorder arises from a random anisotropy, where the spin can point either parallel or antiparallel to the anisotropy with the same energy cost. Whether the spin points parallel or antiparallel to the anisotropy is determined by the neighboring spins through the exchange interaction and, consequently, the configuration with the least disorder will be chosen by the system.

The results obtained here are valid in the limit of quenched disorder, i.e., $\tilde{T} \ll 1$, where the random field and anisotropy are temperature independent. If the temperature is close to the Curie temperature of the system, one must include temperature fluctuations in the Landau-Lifshitz equations. Such effects have been considered in other works, and it has been shown that temperature fluctuations decrease the localization length.

To experimentally verify the critical exponents obtained in this paper, we propose a setup in which a disordered magnetic nanowire is sandwiched between two normal metals. Similar setups for ordered magnets have been considered in other works [11–25]. By applying a charge current in the left metal, the spin-Hall effect generates a spin current through the disordered nanowire and into the right metal. This will give rise to a spin wave propagating through the hybrid structure and into the right metal, where the spin current is converted into a charge current via the inverse spin-Hall effect.

Alternatively, we can instead sandwich a disordered magnet between two ferromagnetic leads. We can excite spin waves in the left ferromagnet by applying a microwave with the ferromagnet resonance frequency. This spin wave will then propagate through the disordered insulator and into the right ferromagnet, where the resulting spin current can be measured. By measuring the spin current propagating through the disordered region, one should be able to characterize the localization length in terms of the critical exponents of the system.

[1] V. V. Kruglyak, S. O. Demokritov, and D. Grundler, J. Phys. D: Appl. Phys. **43**, 264001 (2010).

[2] A. V. Chumak, V. I. Vasyuchka, A. A. Serga, and B. Hillebrands, Nat. Phys. **11**, 453 (2015).

[3] A. A. Serga, A. V. Chumak, and B. Hillebrands, J. Phys. D: Appl. Phys. **43**, 264002 (2010).

[4] V. Kruglyak and R. Hicken, J. Magn. Magn. Mater. **306**, 191 (2006).

[5] A. Qaiumzadeh, L. A. Kristiansen, and A. Brataas, Phys. Rev. B **97**, 020402(R) (2018).

[6] E. G. Tveten, A. Qaiumzadeh, and A. Brataas, Phys. Rev. Lett. **112**, 147204 (2014).

[7] S. Neusser and D. Grundler, Adv. Mater. **21**, 2927 (2009).

[8] Y. Tserkovnyak, A. Brataas, and G. E. W. Bauer, Phys. Rev. Lett. **88**, 117601 (2002).

[9] G. E. W. Bauer, E. Saitoh, and B. J. van Wees, Nat. Mater. **11**, 391 (2012).

[10] J. Sinova, S. O. Valenzuela, J. Wunderlich, C. H. Back, and T. Jungwirth, Rev. Mod. Phys. **87**, 1213 (2015).

[11] R. Karplus and J. M. Luttinger, Phys. Rev. **95**, 1154 (1954).

[12] M. Dyakonov and V. Perel, Phys. Lett. A **35**, 459 (1971).

[13] S. Zhang, Phys. Rev. Lett. **85**, 393 (2000).

[14] S. Murakami, N. Nagaosa, and S.-C. Zhang, Science **301**, 1348 (2003).

[15] J. Sinova, D. Culcer, Q. Niu, N. A. Sinitsyn, T. Jungwirth, and A. H. MacDonald, Phys. Rev. Lett. **92**, 126603 (2004).

[16] T. Jungwirth, J. Wunderlich, and K. Olejník, Nat. Mater. **11**, 382 (2012).

[17] Y. Kajiwara, K. Harii, S. Takahashi, J. Ohe, K. Uchida, M. Mizuguchi, H. Umezawa, H. Kawai, K. Ando, K. Takanashi, S. Maekawa, and E. Saitoh, Nature (London) **464**, 262 (2010).

[18] E. Saitoh, M. Ueda, H. Miyajima, and G. Tatara, Appl. Phys. Lett. **88**, 182509 (2006).

[19] S. O. Valenzuela and M. Tinkham, Nature (London) **442**, 176 (2006).

[20] T. Kimura, Y. Otani, T. Sato, S. Takahashi, and S. Maekawa, Phys. Rev. Lett. **98**, 156601 (2007).

[21] J.-i. Ohe, A. Takeuchi, and G. Tatara, Phys. Rev. Lett. **99**, 266603 (2007).

[22] T. Seki, Y. Hasegawa, S. Mitani, S. Takahashi, H. Imamura, S. Maekawa, J. Nitta, and K. Takanashi, Nat. Mater. **7**, 125 (2008).

[23] K. Ando, Y. Kajiwara, S. Takahashi, S. Maekawa, K. Takemoto, M. Takatsu, and E. Saitoh, Phys. Rev. B **78**, 014413 (2008).

[24] K. Ando, M. Morikawa, T. Trypiniotis, Y. Fujikawa, C. H. W. Barnes, and E. Saitoh, Appl. Phys. Lett. **96**, 082502 (2010).

[25] L. J. Cornelissen, J. Liu, R. A. Duine, J. B. Youssef, and B. J. van Wees, Nat. Phys. **11**, 1022 (2015).

[26] H. Ochoa, R. Zarzuela, and Y. Tserkovnyak, Phys. Rev. B **98**, 054424 (2018).

[27] Y. Tserkovnyak and H. Ochoa, Phys. Rev. B **96**, 100402(R) (2017).

[28] N. Arakawa and J.-i. Ohe, Phys. Rev. B **98**, 014421 (2018).

[29] M. Evers, C. A. Müller, and U. Nowak, Phys. Rev. B **97**, 184423 (2018).

[30] H. V. Gomonay, R. V. Kunitsyn, and V. M. Loktev, Phys. Rev. B **85**, 134446 (2012).

[31] P. Buczek, S. Thomas, A. Marmodoro, N. Buczek, X. Zubizarreta, M. Hoffmann, T. Balashov, W. Wulfhekel, K. Zakeri, and A. Ernst, J. Phys.: Condens. Matter **30**, 423001 (2018).

[32] D. Wesenberg, T. Liu, D. Balzar, M. Wu, and B. L. Zink, Nat. Phys. **13**, 987 (2017).

[33] R. Lebrun, A. Ross, S. A. Bender, A. Qaiumzadeh, L. Baldrati, J. Cramer, A. Brataas, R. A. Duine, and M. Kläui, Nature (London) **561**, 222 (2018).

[34] B. I. Halperin and W. M. Saslow, Phys. Rev. B **16**, 2154 (1977).

[35] C. L. Henley, H. Sompolinsky, and B. I. Halperin, Phys. Rev. B **25**, 5849 (1982).

[36] P. W. Anderson, B. I. Halperin, and C. M. Varma, Philos. Mag. **25**, 1 (1972).

[37] P. Anderson, Mater. Res. Bull. **5**, 549 (1970).

[38] I. Y. Korenblit and E. F. Shender, Sov. Phys. Usp. **21**, 832 (1978).

[39] R. N. Costa Filho and M. G. Cottam, J. Appl. Phys. **81**, 5749 (1997).

[40] R. Bhargava and D. Kumar, Phys. Rev. B **19**, 2764 (1979).

[41] R. Weber, Z. Phys. A **223**, 299 (1969).

[42] S. E. Barnes, J. Phys. F: Met. Phys. **11**, L249 (1981) .

[43] N. Arakawa and J.-i. Ohe, Phys. Rev. B **97**, 020407(R) (2018).

[44] C. De Dominicis and I. Giardina, *Random Fields and Spin Glasses: A Field Theory Approach* (Cambridge University Press, Cambridge, UK, 2006).

[45] G. Herzer, in *Properties and Applications of Nanocrystalline Alloys from Amorphous Precursors*, edited by B. Idzikowski, P. Švec, and M. Miglierini (Springer Netherlands, Dordrecht, 2005), pp. 15–34.

[46] R. Alben, J. J. Becker, and M. C. Chi, J. Appl. Phys. **49**, 1653 (1978).

[47] R. Harris, M. Plischke, and M. J. Zuckermann, Phys. Rev. Lett. **31**, 160 (1973).

[48] J. Herbrych and J. Kokalj, Phys. Rev. B **95**, 125129 (2017).

[49] A. A. Fedorenko, Phys. Rev. E **86**, 021131 (2012).

[50] S. F. Edwards and P. W. Anderson, J. Phys. F: Met. Phys. **5**, 965 (1975).

[51] D. Sherrington and S. Kirkpatrick, Phys. Rev. Lett. **35**, 1792 (1975).

[52] D. Mattis, Phys. Lett. A **56**, 421 (1976).

[53] A. P. Young, *Spin Glasses and Random Fields* (World Scientific, Singapore, 1997).

[54] G. Parisi, Phys. Rev. Lett. **50**, 1946 (1983).

[55] J. Smith, A. Lee, P. Richerme, B. Neyenhuis, P. W. Hess, P. Hauke, M. Heyl, D. A. Huse, and C. Monroe, Nat. Phys. **12**, 907 (2016).

[56] D. Belanger and A. Young, J. Magn. Magn. Mater. **100**, 272 (1991).

[57] N. G. Fytas, V. Martín-Mayor, M. Picco, and N. Sourlas, Phys. Rev. Lett. **116**, 227201 (2016).

[58] G. Tarjus and M. Tissier, Phys. Rev. Lett. **93**, 267008 (2004).

[59] J. Z. Imbrie, Phys. Rev. Lett. **53**, 1747 (1984).

[60] A. Malakis and N. G. Fytas, Phys. Rev. E **73**, 016109 (2006).

[61] S. Fishman and A. Aharony, J. Phys. C: Solid State Phys. **12**, L729 (1979).

[62] J. L. Cardy, Phys. Rev. B **29**, 505 (1984).

[63] D. J. Luitz, N. Laflorencie, and F. Alet, Phys. Rev. B **91**, 081103(R) (2015).

[64] A. Pal and D. A. Huse, Phys. Rev. B **82**, 174411 (2010).

[65] A. D. Luca and A. Scardicchio, Eur. Phys. Lett. **101**, 37003 (2013).

[66] A. Nanduri, H. Kim, and D. A. Huse, Phys. Rev. B **90**, 064201 (2014).

[67] M. Žnidarič, T. Prosen, and P. Prelovšek, Phys. Rev. B **77**, 064426 (2008).

[68] I. Khait, S. Gazit, N. Y. Yao, and A. Auerbach, Phys. Rev. B **93**, 224205 (2016).

[69] P. W. Anderson, Phys. Rev. **109**, 1492 (1958).

[70] D. Vollhardt and P. Wölfle, Phys. Rev. Lett. **48**, 699 (1982).

[71] A. J. Bray and M. A. Moore, Phys. Rev. Lett. **41**, 1068 (1978).

[72] G. Parisi, Phys. Rev. Lett. **43**, 1754 (1979).

[73] M. Evers, C. A. Müller, and U. Nowak, Phys. Rev. B **92**, 014411 (2015).

[74] E. Abrahams, P. W. Anderson, D. C. Licciardello, and T. V. Ramakrishnan, Phys. Rev. Lett. **42**, 673 (1979).

[75] V. Cannella and J. A. Mydosh, Phys. Rev. B **6**, 4220 (1972).

[76] R. Landauer, IBM J. Res. Dev. **1**, 223 (1957).

[77] C. W. J. Beenakker, Rev. Mod. Phys. **69**, 731 (1997).

[78] K. R. Sapkota, R. Dulal, B. R. Dahal, I. L. Pegg, and J. Philip, J. Vac. Sci. Technol. B **33**, 051807 (2015).

[79] R. R. Galazka, S. Nagata, and P. H. Keesom, Phys. Rev. B **22**, 3344 (1980).

[80] S. Venugopalan, A. Petrou, R. R. Galazka, A. K. Ramdas, and S. Rodriguez, Phys. Rev. B **25**, 2681 (1982).

[81] T. Giebultowicz, B. Lebech, B. Buras, W. Minor, H. Kepa, and R. R. Galazka, J. Appl. Phys. **55**, 2305 (1984).

[82] T. Kaneyoshi, Phys. B (Amsterdam, Neth.) **462**, 34 (2015).

[83] S. F. Edwards and F. Tanaka, J. Phys. F: Met. Phys. **10**, 2471 (1980).

[84] B. Drossel and M. A. Moore, Phys. Rev. B **70**, 064412 (2004).

[85] Z. Ma, J. Wang, Z.-Y. Dong, J. Zhang, S. Li, S.-H. Zheng, Y. Yu, W. Wang, L. Che, K. Ran, S. Bao, Z. Cai, P. Čermák, A. Schneidewind, S. Yano, J. S. Gardner, X. Lu, S.-L. Yu, J.-M. Liu, S. Li, J.-X. Li, and J. Wen, Phys. Rev. Lett. **120**, 087201 (2018).

[86] T. Castellani and A. Cavagna, J. Stat. Mech. (2005) P05012.

[87] M. Mezard, G. Parisi, and M. Virasoro, *Spin Glass Theory and Beyond* (World Scientific, Singapore, 1986).

[88] A. J. Bray and M. A. Moore, J. Phys. C: Solid State Phys. **14**, 1313 (1981).

[89] T. Li, Phys. Rev. B **24**, 6579 (1981).

[90] C. M. Newman and D. L. Stein, Phys. Rev. E **60**, 5244 (1999).

[91] Z. Burda, A. Krzywicki, O. C. Martin, and Z. Tabor, Phys. Rev. E **73**, 036110 (2006).

[92] Z. Burda, A. Krzywicki, and O. C. Martin, Phys. Rev. E **76**, 051107 (2007).

[93] B. Waclaw and Z. Burda, Phys. Rev. E **77**, 041114 (2008).

[94] A. Heuer, J. Phys.: Condens. Matter **20**, 373101 (2008).

[95] An analogous expression can be used for the right lead.

[96] B. Wang, J. Wang, J. Wang, and D. Y. Xing, Phys. Rev. B **69**, 174403 (2004).

[97] A. Aharony and A. B. Harris, Phys. Rev. Lett. **77**, 3700 (1996).

[98] E. Abrahams, *50 Years of Anderson Localization* (World Scientific, Singapore, 2010).

[99] R. A. Serota, R. K. Kalia, and P. A. Lee, Phys. Rev. B **33**, 8441 (1986).

[100] Md. A. Aamir, P. Karnatak, A. Jayaraman, T. P. Sai, T. V. Ramakrishnan, R. Sensarma, and A. Ghosh, Phys. Rev. Lett. **121**, 136806 (2018).

[101] P. A. Lee, Phys. Rev. Lett. **53**, 2042 (1984).

[102] J. Billy, V. Josse, Z. Zuo, A. Bernard, B. Hambrecht, P. Lugan, D. Clément, L. Sanchez-Palencia, P. Bouyer, and A. Aspect, Nature (London) **453**, 891 (2008).

[103] U. Ritzmann, D. Hinzke, and U. Nowak, Phys. Rev. B **89**, 024409 (2014).

[104] A. A. Starikov, Y. Liu, Z. Yuan, and P. J. Kelly, Phys. Rev. B **97**, 214415 (2018).

Paper [2]

Martin F. Jakobsen, Kristian B. Naess, Paramita Dutta, Arne Brataas, and Alireza Qaiumzadeh

"Electrical and thermal transport in antiferromagnet-superconductor junctions"

Electrical and thermal transport in antiferromagnet-superconductor junctions

Martin F. Jakobsen [1], Kristian B. Naess,[1] Paramita Dutta,[2,3] Arne Brataas [1], and Alireza Qaiumzadeh [1]

[1]*Center for Quantum Spintronics, Department of Physics, Norwegian University of Science and Technology, NO-7491 Trondheim, Norway*
[2]*Department of Physics and Astronomy, Uppsala University, Box 516, S-751 20 Uppsala, Sweden*
[3]*Institute of Physics, Sachivalaya Marg, Bhubaneswar 751005, India*

We demonstrate that antiferromagnet-superconductor (AF-S) junctions show qualitatively different transport properties than normal metal–superconductor (N-S) and ferromagnet-superconductor (F-S) junctions. We attribute these transport features to the presence of two different scattering processes in AF-S junctions, i.e., specular reflection of holes and retroreflection of electrons. Using the Blonder-Tinkham-Klapwijk formalism, we find that the electrical and thermal conductances depend nontrivially on antiferromagnetic exchange strength, voltage, and temperature bias. Furthermore, we show that the interplay between the Néel vector direction and the interfacial Rashba spin-orbit coupling leads to a large anisotropic magnetoresistance. The unusual transport properties make AF-S interfaces unique among the traditional condensed-matter-system-based superconducting junctions.

Introduction. Heterostructures composed of superconductors and nonsuperconducting materials exhibit technologically relevant quantum phenomena [1–8]. Examples include superconducting qubits [9–11], microwave resonators [12], single-photon detectors [13], and AC Josephson junction lasers [14]. Superconducting heterostructures also form the basis for experimental methods such as point-contact spectroscopy [15–17] and scanning tunneling spectroscopy [18,19], enabling the determination of the superconducting gap and investigations of the phase diagram in unconventional superconductors [20–22].

The simplest superconducting heterostructure is a normal metal (N)–superconductor (S) junction. The low-bias transport is dominated by Andreev reflection (AR) [8,23,24]. In conventional AR, an incident electron is retroreflected as a hole of the opposite spin, and a Cooper pair is transmitted into the S layer. Since the Cooper pair carries a charge of $2e$ and zero heat, AR enhances electrical conductance and suppresses thermal conductance [25–27]. In a Josephson junction (S-N-S) [28], AR can occur repeatedly, resulting in Andreev bound states that carry a supercurrent across the junction. Josephson junctions enable technologies such as electrical and thermal interferometers [29,30].

The spin dependence of AR at superconducting interfaces causes the transport properties to change drastically when ferromagnetic (F) layers are introduced [31]. The exchange interaction splits the majority- and minority-spin bands in the F layer, which reduces the AR amplitude and consequently the conductance in a F-S junction [21,32]. However, finite spin-orbit coupling (SOC) at the interface enables tunable anisotropic spin-flipped AR, which can increase the electric and thermal conductance [33–36]. S-F-S Josephson junctions have been shown to exhibit spin-triplet pairing, potentially enabling superconducting spin currents and qubits [2,3,37–

41]. However, the finite net magnetization of ferromagnets in superconducting spintronics presents a significant drawback for applications in nanoscale devices.

Antiferromagnets (AFs) are magnetically ordered materials with zero net magnetization and negligible stray fields, as well as intrinsic high-frequency dynamics. Thus, AFs are promising candidates for novel high-density and ultrafast spintronic-based nanodevices [42]. Based on these characteristics and recent experimental developments, the emerging field of antiferromagnetic spintronics has attracted intensive interest [43–52]. Additionally, the possible coexistence of antiferromagnetism with superconductivity [53–55] shows the great potential of antiferromagnetic materials for application in superconducting spintronics [31].

AF-S junctions have been theoretically shown to exhibit additional scattering processes that differ from those in N(F)-S junctions [56]. In Josephson junctions, these scattering processes create low-energy bound states [57] that lead to anomalous phase shifts [58] and atomic-scale 0-π transitions [59–62]. However, although the existence of Josephson supercurrents in S-AF-S junctions has been experimentally reported [63–68], other theoretical predictions have yet to be explored.

To our knowledge, the effect of these additional scattering processes on the electrical and thermal transport in AF-S bilayers remains an open question. In this Rapid Communication, we address this issue and point out unique experimental signatures in the electrical and thermal conductance.

Model. We consider a collinear, two-sublattice AF metal on a cubic lattice attached to a conventional *s*-wave superconductor. The AF and S are both semi-infinite and occupy the regions $z < 0$ and $z > 0$, respectively. We assume a compensated interface at $z = 0$.

To investigate the electrical and thermal transport, we use the Blonder-Tinkham-Klapwijk (BTK) scattering formalism

[25], where the conductances are determined by the reflection coefficients of the scattering matrix. We obtain the reflection coefficients by solving the Bogoliubov–de Gennes (BdG) equation.

The BdG Hamiltonian of an AF-S junction in the continuum limit consists of a Hamiltonian for itinerant charge carriers H_e, an antiferromagnetic exchange coupling H_{AF}, an interfacial barrier potential H_I, and a Hamiltonian modeling the S layer H_S,

$$H = H_e + H_{AF} + H_I + H_S. \tag{1}$$

The Pauli matrices $\mathbf{s}$, $\boldsymbol{\sigma}$, and $\boldsymbol{\tau}$ denote the spin, sublattice, and charge degrees of freedom, respectively. We also define $\tau_4^{\pm} = \mathrm{diag}(1, \pm K)$, where K represents complex conjugation, and $\tau_{\pm} = (\tau_x \pm i\tau_y)/2$.

The Hamiltonian governing the motion of the itinerant charge carriers is [48,69,70]

$$H_e = \gamma(\mathbf{p})\,\tau_z \otimes \sigma_x \otimes s_0 - \mu\,\tau_z \otimes \sigma_0 \otimes s_0, \tag{2}$$

where $\gamma(\mathbf{p}) = (\mathbf{p}^2 - \hbar^2 k_0^2)/2m$ is the kinetic energy, $\mathbf{p} = -i\hbar\nabla$ is the momentum operator, m is the effective mass of the charge carriers, $\boldsymbol{k}_0$ is the wave vector at which $\gamma(\hbar\mathbf{k}_0) = 0$, and $\hbar$ is the reduced Planck constant. The chemical potential is $\mu = \mu_{AF}\Theta(-z) + \mu_S\Theta(z)$, where $\Theta(\cdot)$ is the Heaviside step function.

The s-d exchange interaction between localized antiferromagnetic moments and itinerant spins reads [48,69,70]

$$H_{AF} = J\,\tau_4^{-} \otimes \sigma_z \otimes (\mathbf{n} \cdot \mathbf{s}), \tag{3}$$

where $J = J_0\Theta(-z)$ denotes the interaction strength and $\mathbf{n} = (\sin\theta\cos\phi, \sin\theta\sin\phi, \cos\theta)$ is the uniform Néel vector. We assume strong anisotropy sets the direction of spins and suppresses quantum fluctuations. The interfacial potential is

$$H_I = V\,\tau_z \otimes \sigma_0 \otimes s_0 + \lambda_R\,\tau_4^{+} \otimes \sigma_x \otimes [(\mathbf{s} \times \mathbf{q}) \cdot \hat{z}], \tag{4}$$

where $V = V_0\delta(z)$ is the strength of the spin-independent potential barrier and $\lambda_R = \lambda_0\delta(z)$ is the strength of the Rashba SOC (RSOC) [71] due to the inversion symmetry breaking in the z direction. These terms permit spin-conserving and spin-flipped reflection processes, respectively. AR and spin-flipped AR result in spin-singlet and spin-triplet Cooper pairs in S, respectively.

Finally, we model the S layer using a mean-field BCS Hamiltonian,

$$H_S = \Delta(T)\,\tau_{+} \otimes (\sigma_0 \otimes is_y) + \mathrm{H.c.}, \tag{5}$$

where $\Delta(T) = \Delta_0 \tanh[1.74\sqrt{(T_c/T) - 1}]\Theta(z)$ is an interpolation formula for the temperature-dependent gap of an s-wave superconductor with a critical temperature T_c [72–74]. Δ_0 is the constant bulk value of the gap [57].

To determine the reflection coefficients, we solve the BdG eigenvalue problem,

$$H\psi = E\psi, \tag{6}$$

where ψ is an eigenvector with eigenvalue $E > 0$ (see the Supplemental Material [75]). The x and y directions are translationally invariant. Hence, the eigenvector takes the form $\psi = \chi e^{i\mathbf{q}_\parallel \cdot \mathbf{r}} e^{iq_z z}$, where $\mathbf{q}_\parallel = (q_x, q_y, 0)$ is the conserved component of the wave vector parallel to the interface and q_z is the
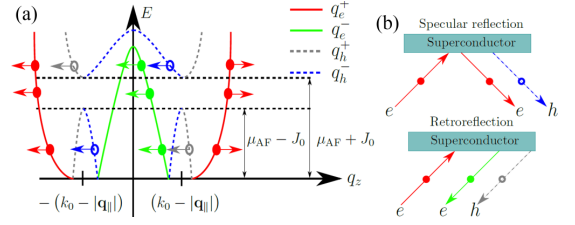

FIG. 1. (a) The allowed scattering processes [see Eq. (8)]. Electrons (holes) are drawn as solid (open) circles. Incoming (reflected) particles are represented by rightward (leftward) arrows. (b) A sketch of the possible scattering processes that can occur at an AF-S junction.

wave-vector component normal to the interface. The spinor χ is expressed in the basis [75]

$$\chi = (A_{e\uparrow}, A_{e\downarrow}, B_{e\uparrow}, B_{e\downarrow}, A_{h\uparrow}, A_{h\downarrow}, B_{h\uparrow}, B_{h\downarrow}). \tag{7}$$

Here, A (B), $\uparrow$ ($\downarrow$), and e (h) refer to sublattice, spin, and charge degrees of freedom, respectively. Substituting the eigenvector into Eq. (6) for $z < 0$, gives the wave vectors $q_z = q_{e(h)}^{\pm}$ in the AF layer,

$$q_{e(h)}^{\pm} = \sqrt{k_0^2 - \mathbf{q}_\parallel^2 \pm \frac{2m}{\hbar^2}\sqrt{[E + (-)\mu_{AF}]^2 - J^2}}. \tag{8}$$

Figure 1 shows a plot of the dispersion relations of the AF layer given in Eq. (8), where the possible scattering processes are identified. In contrast to an N(F)-S junction, an AF-S junction permits both specular AR and retro normal reflection (NR) [56–58].

In the following, we show how these two scattering mechanisms, i.e., retro NR and specular AR, affect the transport properties of AF-S junctions.

Thermoelectric coefficients. To study electrical and thermal transport, we assume the AF is in contact with a biased reservoir, and that the S is in contact with a reference reservoir. Applying a bias voltage U or a temperature difference ΔT through the junction induces an electric current or a heat current, respectively. In the BTK formalism [25,26,76], the differential charge ($G_C = dI/dU$) and heat ($L_Q = dI/d\Delta T$) conductances read

$$G_C = \frac{Ae^2}{4\pi^3\hbar} \int dE\, d^2\mathbf{q}_\parallel \frac{1 - R_e + R_h}{4k_B T \cosh^2\left(\frac{E - eU}{2k_B T}\right)}, \tag{9a}$$

$$L_Q = \frac{Ak_B}{4\pi^3\hbar} \int dE\, d^2\mathbf{q}_\parallel \frac{E^2(1 - R_e - R_h)}{[2k_B(T + \Delta T)]^2 \cosh^2\left[\frac{E}{2k_B(T + \Delta T)}\right]}, \tag{9b}$$

where A and T are the interfacial area and the thermal equilibrium temperature, respectively. The total reflection probabilities for electrons (e) and holes (h) are

$$R_{e(h)} = \sum_s (R_{e(h),s}^{+} + R_{e(h),s}^{-}). \tag{10}$$

Here, $R_{c,s}^{\pm}$ is the reflection probability for particles with wave vector $q_c^{\pm}$, where $c = e, h$ and $s = \uparrow, \downarrow$ [75]. AR results in a net charge transfer of $2e$, but zero heat transfer [77–79] across
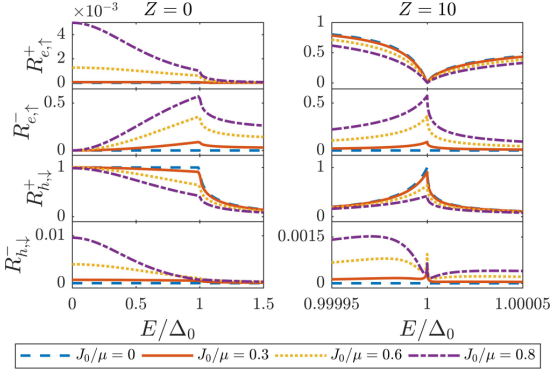
FIG. 2. The reflection probabilities as functions of the energy E/Δ_0, the barrier strength Z, and the exchange strength J_0/μ. The scattering processes associated with $R_{e,h}^-$ are absent at an N(F)-S junction; they are the result of the additional degrees of freedom in an AF. R_e^- and R_h^- correspond to retro NR and specular AR, respectively.

FIG. 3. The electrical conductance $\tilde{G}_C$ and the thermal conductance $\tilde{L}_Q$ as functions of the dimensionless voltage eU/Δ_0 and dimensionless temperature bias $\Delta T/T_c$, respectively, for different spin-independent barrier strengths Z and exchange strengths J_0/μ. The insets show the peak in the electrical conductance, and the percentage increase in the conductances as a function J_0/μ, respectively.

the interface; thus, AR increases the electrical conductance and decreases the thermal conductance.

Numerical parameters. Before presenting our numerical results, we introduce our dimensionless parameters: The spin-independent barrier strength $Z = V_0 m/\hbar^2 q_*$, the Rashba strength $\lambda = 2\lambda_0 m/\hbar^2 q_*$, and the exchange strength J_0/μ. Here, $q_*^2 = k_0^2 + q_F^2$, where $q_F^2 = 2m\mu/\hbar^2$. For simplicity, we set $\mu_{AF} = \mu_S = \mu$ and normalize the electrical and thermal conductance with respect to the corresponding Sharvin conductance [8]: $\tilde{G}_C = G_C/G_C^{Sh}$ and $\tilde{L}_Q = L_Q/L_Q^{Sh}$. The Sharvin electrical (thermal) conductance is the electrical (thermal) conductance evaluated in the limit $\Delta_0 = J_0 = Z = 0$, i.e., the response functions of a normal metal with perfect transmission: $G_C^{Sh} = e^2 q_*^2 A/4\pi^2\hbar$ and $L_Q^{Sh} = Ak_B^2 T_c q_*^2/12\hbar$.

In our calculations, we estimate the effective mass to be $\hbar^2/2m = 0.5 \text{ eV nm}^2$ based on a tight-binding model with typical material parameters [48,69,70]. Furthermore, the superconducting gap Δ_0 is several orders of magnitude smaller than the chemical potential μ. For concreteness, we set $\mu = 2$ eV and allow the exchange strength to lie in the interval $0 < J_0/\mu < 1$, where the system is conducting. As $J_0/\mu \to 1$, the AF material becomes an insulator, and the transport properties vanish. We consider the temperature range $0 < T/T_c < 1$ so that superconductivity does not break down.

Calculation of reflection probabilities. Figure 2 shows the behavior of the reflection probabilities as functions of energy for different exchange strengths in both the transparent $(Z = 0)$ and tunneling $(Z \gg 1)$ regimes in the absence of RSOC.

For simplicity, we first consider a transparent interface $(Z = 0)$ and the subgap regime $(E < \Delta_0)$. In the normal metal limit $(J_0 = 0)$, we find that retro AR is the dominant scattering process [25]. Retro NR and specular AR increase as the exchange interaction J_0 increases, because with the onset of J_0, the new scattering channels associated with the sublattice degrees of freedom become available. In the supergap regime $(E > \Delta_0)$, electronlike and holelike charge carriers can propagate in the S layer.
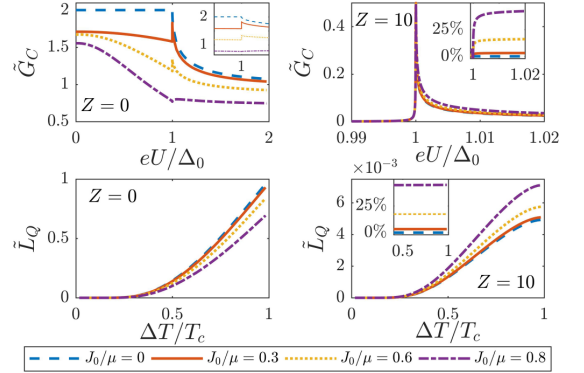
If the interface is not transparent $(Z \neq 0)$, AR is suppressed while NR is enhanced, because fewer electrons are allowed to enter the S layer to form Cooper pairs. Increasing J_0 leads to an increase in retro NR and a decrease in specular NR (see Fig. 2).

Electrical and thermal conductance. In the following, we elucidate experimental signatures in the response functions of the system. To simplify the discussion, we only consider the low-temperature limit $T \to 0$ in Eqs. (9a) and (9b) in the rest of this Rapid Communication. In Fig. 3, we plot the electrical conductance and the thermal conductance as functions of the voltage and temperature bias, respectively, for different exchange and barrier strengths in the absence of SOC.

First, we focus on the electrical conductance shown in Fig. 3. In the absence of a barrier and exchange interaction, the system behaves as a transparent N-S junction. In this case, each electron incident from the N layer enters the S layer and forms a Cooper pair, resulting in 100% retro AR; consequently, the electrical conductance is $\tilde{G}_C = 2$. As the exchange strength increases, retro NR eventually becomes the dominant scattering process. Thus, with increasing J_0, less total charge is transported across the junction and the electrical conductance decreases. In contrast to a F-S junction, we find a sharp finite peak in the electrical conductance at $eU/\Delta_0 = 1$.

In the tunneling limit $(Z = 10)$, the electrical conductance is singular at $eU/\Delta_0 = 1$, which originates from the singularity in the density of states (DOS) in the S layer.

In contrast to the electrical conductance, the thermal conductance is suppressed by AR. The physical reason is that Cooper pairs carry finite charge but zero heat across the junction. Therefore, for the thermal conductance to be finite, the temperature must be so high that electronlike and holelike particles can be transmitted into the S layer. Since higher temperatures result in a greater transmission of particles, the thermal conductance increases with increasing temperature bias, as shown in Fig. 3.
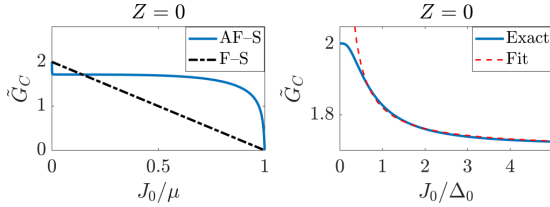
FIG. 4. Left: Zero-temperature electrical conductance $\tilde{G}_C$ of the system as a function of the exchange strength J_0/μ. The dashed-dotted line represents the electrical conductance of a F-S junction [32]. Right: The behavior of $\tilde{G}_C$ as a function J_0/Δ_0. The dashed red line represents a numerical fit of the electrical conductance, $\tilde{G}_C \sim (J/\Delta_0)^{-1.0}$.

FIG. 5. The electrical AMR in an AF-S junction as a function of the orientation θ of the Néel vector and the exchange strength J_0/μ. The inset show the dependence of the AMR maxima on the RSOC strength λ.

In the transparent limit ($Z = 0$), the retro NR increases with increasing exchange strength. Since less particles are transmitted into the S layer, the thermal conductance decreases with increasing exchange strength. As the barrier strength increases, even fewer particles are transmitted into the S layer. In the tunneling limit ($Z = 10$), the thermal conductance is strongly suppressed.

Figure 3 shows that, in the transparent limit, the increase of exchange strength reduces both the electrical and thermal conductance; by contrast, in the tunneling regime, the increase in exchange strength increases both of them. This behavior occurs due to the interplay between the exchange interaction and the barrier in the supergap regime ($E > \Delta_0$), where tunneling into the S layer is also allowed. In the tunneling limit, the exchange interaction enhances the transmission of both electronlike and holelike particles into the S layer, consequently increasing the electrical and thermal conductance.

To compare the AF-S junction with the F-S junction, we plot the electrical conductance as a function of the exchange strength in Fig. 4. In the F-S junction, the electrical conductance decreases linearly with increasing exchange strength, $\tilde{G}_C \approx 2(1 - J_0/\mu)$ [32]. However, in the AF-S junction, the relationship between the electrical conductance and the exchange strength is more subtle. The electrical conductance decays rapidly at small J_0/μ, is almost constant for intermediate J_0/μ, and decays as $J_0/\mu \to 1$. We have checked that these features are robust by varying m, μ, and Δ_0 within the experimentally relevant intervals. The right panel of Fig. 4 shows that the electrical conductance decays rapidly with increasing exchange strength on an energy scale set by the superconducting gap. In the regime where $J_0 \ll \Delta_0$, the system behaves as an N-S junction, such that $\tilde{G}_C = 2$. In the regime $J_0 \sim \Delta_0$, we find that the reflection probabilities become dependent on the angle of incidence [75]. For electrons close to normal incidence, we find that retro AR dominates transport. For electrons with an angle of incidence nearly parallel to the interface, we find that retro AR is suppressed and specular NR is enhanced. This sudden enhancement of specular NR leads to the sharp decay of the electrical conductance observed in Fig. 4. Numerically, we find that $\tilde{G}_c \sim (J_0/\Delta_0)^{-1.0}$ [75].

In the regime $\Delta_0 \ll J_0 \ll \mu$, the DOS in the AF layer is approximately constant, and consequently, so is the electrical conductance [75]. As $J_0/\mu \to 1$, the AF layer starts to behave as an insulator, suppressing all transport properties.
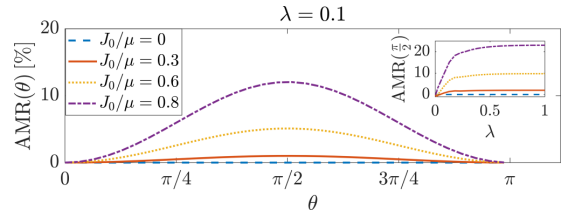
Anisotropic magnetoresistance. So far, we have not considered the effect of finite interfacial RSOC, resulting from the inversion symmetry breaking at the interface. For finite interfacial RSOC, additional scattering channels are opened in which spin-flip scattering is allowed. Spin-flipped AR allows for the formation of spin-triplet Cooper pairs in the S layer [33,36,80]. Recently, it has been found that in F-S junctions, interfacial RSOC leads to a large anisotropic magnetoresistance (AMR) [33,81], while there is no AMR in N-S junctions.

In the AF layer, the spin quantization axis is determined by the Néel vector. Consequently, a finite interfacial RSOC leads to anisotropy in the electrical and thermal conductance for an AF-S junction. Since we consider only an interfacial RSOC with an inversion-breaking axis in the z direction, this AMR depends only on the Néel vector's polar angle θ.

Figure 5 shows electrical $\text{AMR}(\theta) = 1 - \tilde{G}(0)/\tilde{G}(\theta)$ as a function of the Néel vector direction for a fixed RSOC strength. We find that the minima and maxima occur at $\theta = \{0, \pi\}$ and $\theta = \pi/2$, respectively. The inset shows that the maximum AMR increases with λ. The qualitative features of the electrical and thermal AMR is identical. Thus, similar to F-S junctions and in contrast to N-S junctions, AF-S junctions show a strong AMR. In an AF-N junction ($\Delta_0 \to 0$), the electrical (thermal) AMR is approximately 75% smaller (50% larger) than that in an AF-S junction. The simultaneous enhancement of the electrical AMR and diminution of the thermal AMR in an AF-S junction can be attributed to the finite AR in the presence of the S layer.

Concluding remarks. We demonstrate that the electrical and thermal conductance of AF-S junctions are qualitatively different from those of N(F)-S junctions due to the emergence of two scattering processes: Specular AR and retro NR. Furthermore, we show that there is a large AMR in the presence of a finite interfacial RSOC.

Our results reveal that superconducting spintronics based on antiferromagnetic materials, opens a fascinating playground for intriguing physical phenomena. We hope that this theoretical study will inspire further experimental work on AF-S heterostructures.

[1] R. Yan, G. Khalsa, S. Vishwanath, Y. Han, J. Wright, S. Rouvimov, D. S. Katzer, N. Nepal, B. P. Downey, D. A. Muller, H. G. Xing, D. J. Meyer, and D. Jena, Nature (London) **555**, 183 (2018).

[2] V. V. Ryazanov, V. A. Oboznov, A. Y. Rusanov, A. V. Veretennikov, A. A. Golubov, and J. Aarts, Phys. Rev. Lett. **86**, 2427 (2001).

[3] J. W. A. Robinson, J. D. S. Witt, and M. G. Blamire, Science **329**, 59 (2010).

[4] M. Eschrig, J. Kopu, J. C. Cuevas, and G. Schön, Phys. Rev. Lett. **90**, 137003 (2003).

[5] R. M. Lutchyn, J. D. Sau, and S. Das Sarma, Phys. Rev. Lett. **105**, 077001 (2010).

[6] B. Baek, W. H. Rippard, S. P. Benz, S. E. Russek, and P. D. Dresselhaus, Nat. Commun. **5**, 3888 (2014).

[7] M. Eschrig, Rep. Prog. Phys. **78**, 104501 (2015).

[8] I. Žutić, J. Fabian, and S. Das Sarma, Rev. Mod. Phys. **76**, 323 (2004).

[9] L. DiCarlo, J. M. Chow, J. M. Gambetta, L. S. Bishop, B. R. Johnson, D. I. Schuster, J. Majer, A. Blais, L. Frunzio, S. M. Girvin, and R. J. Schoelkopf, Nature (London) **460**, 240 (2009).

[10] J. E. Mooij, T. P. Orlando, L. Levitov, L. Tian, C. H. van der Wal, and S. Lloyd, Science **285**, 1036 (1999).

[11] F. Arute, K. Arya, R. Babbush, D. Bacon, J. C. Bardin, R. Barends, R. Biswas, S. Boixo, F. G. S. L. Brandao, D. A. Buell, B. Burkett, Y. Chen, Z. Chen, B. Chiaro, R. Collins, W. Courtney, A. Dunsworth, E. Farhi, B. Foxen, A. Fowler *et al.*, Nature (London) **574**, 505 (2019).

[12] M. J. Lancaster, T. S. M. Maclean, Z. Wu, A. Porch, P. Woodall, and N. N. Alford, IEE Proc., Part H: Microwaves, Antennas Propag. **139**, 149 (1992).

[13] G. N. Gol'tsman, O. Okunev, G. Chulkova, A. Lipatov, A. Semenov, K. Smirnov, B. Voronov, A. Dzardanov, C. Williams, and R. Sobolewski, Appl. Phys. Lett. **79**, 705 (2001).

[14] M. C. Cassidy, A. Bruno, S. Rubbert, M. Irfan, J. Kammhuber, R. N. Schouten, A. R. Akhmerov, and L. P. Kouwenhoven, Science **355**, 939 (2017).

[15] S. K. Upadhyay, A. Palanisami, R. N. Louie, and R. A. Buhrman, Phys. Rev. Lett. **81**, 3247 (1998).

[16] R. J. Soulen, J. M. Byers, M. S. Osofsky, B. Nadgorny, T. Ambrose, S. F. Cheng, P. R. Broussard, C. T. Tanaka, J. Nowak, J. S. Moodera, A. Barry, and J. M. D. Coey, Science **282**, 85 (1998).

[17] I. I. Mazin, Phys. Rev. Lett. **83**, 1427 (1999).

[18] R. Meservey and P. Tedrow, Phys. Rep. **238**, 173 (1994).

[19] M. Bode, Rep. Prog. Phys. **66**, 523 (2003).

[20] R. Gonnelli, D. Daghero, and M. Tortello, Curr. Opin. Solid State Mater. Sci. **17**, 72 (2013).

[21] G. Annunziata, M. Cuoco, P. Gentile, A. Romano, and C. Noce, Phys. Rev. B **83**, 094507 (2011).

[22] D. Daghero, M. Tortello, G. A. Ummarino, and R. S. Gonnelli, Rep. Prog. Phys. **74**, 124509 (2011).

[23] D. Daghero and R. S. Gonnelli, Supercond. Sci. Technol. **23**, 043001 (2010).

[24] W.-C. Lee and L. H. Greene, Rep. Prog. Phys. **79**, 094502 (2016).

[25] G. E. Blonder, M. Tinkham, and T. M. Klapwijk, Phys. Rev. B **25**, 4515 (1982).

[26] R. A. Riedel and P. F. Bagwell, Phys. Rev. B **48**, 15198 (1993).

[27] S. Lee, V. Stanev, X. Zhang, D. Stasak, J. Flowers, J. S. Higgins, S. Dai, T. Blum, X. Pan, V. M. Yakovenko, J. Paglione, R. L. Greene, V. Galitski, and I. Takeuchi, Nature (London) **570**, 344 (2019).

[28] B. Josephson, Phys. Lett. **1**, 251 (1962).

[29] F. Giazotto and M. J. Martínez-Pérez, Nature (London) **492**, 401 (2012).

[30] G. D. Guttman, B. Nathanson, E. Ben-Jacob, and D. J. Bergman, Phys. Rev. B **55**, 3849 (1997).

[31] J. Linder and J. W. A. Robinson, Nat. Phys. **11**, 307 (2015).

[32] M. J. M. de Jong and C. W. J. Beenakker, Phys. Rev. Lett. **74**, 1657 (1995).

[33] P. Högl, A. Matos-Abiague, I. Žutić, and J. Fabian, Phys. Rev. Lett. **115**, 116601 (2015).

[34] A. Costa, A. Matos-Abiague, and J. Fabian, Phys. Rev. B **100**, 060507(R) (2019).

[35] P. Dutta, A. Saha, and A. M. Jayannavar, Phys. Rev. B **96**, 115404 (2017).

[36] P. Dutta, K. R. Alves, and A. M. Black-Schaffer, Phys. Rev. B **102**, 094513 (2020).

[37] T. S. Khaire, M. A. Khasawneh, W. P. Pratt, and N. O. Birge, Phys. Rev. Lett. **104**, 137002 (2010).

[38] D. Sprungmann, K. Westerholt, H. Zabel, M. Weides, and H. Kohlstedt, Phys. Rev. B **82**, 060505(R) (2010).

[39] T. Yamashita, K. Tanikawa, S. Takahashi, and S. Maekawa, Phys. Rev. Lett. **95**, 097001 (2005).

[40] A. I. Buzdin, Rev. Mod. Phys. **77**, 935 (2005).

[41] A. I. Buzdin, L. N. Bulaevskii, and S. V. Panyukov, Pis'ma Zh. Eksp. Teor. Fiz. **35**, 147 (1982) [JETP Lett. **35**, 178 (1982)].

[42] V. Baltz, A. Manchon, M. Tsoi, T. Moriyama, T. Ono, and Y. Tserkovnyak, Rev. Mod. Phys. **90**, 015005 (2018).

[43] S. A. Siddiqui, J. Sklenar, K. Kang, M. J. Gilbert, A. Schleife, N. Mason, and A. Hoffmann, Metallic antiferromagnets, J. Appl. Phys. **128**, 040904 (2020).

[44] T. Jungwirth, X. Marti, P. Wadley, and J. Wunderlich, Nat. Nanotechnol. **11**, 231 (2016).

[45] B. G. Park, J. Wunderlich, X. Martí, V. Holý, Y. Kurosaki, M. Yamada, H. Yamamoto, A. Nishide, J. Hayakawa, H. Takahashi, A. B. Shick, and T. Jungwirth, Nat. Mater. **10**, 347 (2011).

[46] X. Martí, B. G. Park, J. Wunderlich, H. Reichlová, Y. Kurosaki, M. Yamada, H. Yamamoto, A. Nishide, J. Hayakawa, H.

Takahashi, and T. Jungwirth, Phys. Rev. Lett. **108**, 017201 (2012).

[47] H. Wang, C. Du, P. C. Hammel, and F. Yang, Phys. Rev. Lett. **113**, 097202 (2014).

[48] J. Železný, H. Gao, K. Výborný, J. Zemen, J. Mašek, A. Manchon, J. Wunderlich, J. Sinova, and T. Jungwirth, Phys. Rev. Lett. **113**, 157201 (2014).

[49] P. Wadley, B. Howells, J. Železný, C. Andrews, V. Hills, R. P. Campion, V. Novák, K. Olejník, F. Maccherozzi, S. S. Dhesi, S. Y. Martin, T. Wagner, J. Wunderlich, F. Freimuth, Y. Mokrousov, J. Kuneš, J. S. Chauhan, M. J. Grzybowski, A. W. Rushforth, K. W. Edmonds *et al.*, Science **351**, 587 (2016).

[50] R. Lebrun, A. Ross, S. A. Bender, A. Qaiumzadeh, L. Baldrati, J. Cramer, A. Brataas, R. A. Duine, and M. Kläui, Nature (London) **561**, 222 (2018).

[51] J. Li, C. B. Wilson, R. Cheng, M. Lohmann, M. Kavand, W. Yuan, M. Aldosary, N. Agladze, P. Wei, M. S. Sherwin, and J. Shi, Nature (London) **578**, 70 (2020).

[52] P. Vaidya, S. A. Morley, J. van Tol, Y. Liu, R. Cheng, A. Brataas, D. Lederman, and E. del Barco, Science **368**, 160 (2020).

[53] M. Feldbacher, F. F. Assaad, F. Hébert, and G. G. Batrouni, Phys. Rev. Lett. **91**, 056401 (2003).

[54] E. Demler, W. Hanke, and S.-C. Zhang, Rev. Mod. Phys. **76**, 909 (2004).

[55] J. Kaczmarczyk and J. Spałek, Phys. Rev. B **84**, 125140 (2011).

[56] I. V. Bobkova, P. J. Hirschfeld, and Y. S. Barash, Phys. Rev. Lett. **94**, 037005 (2005).

[57] B. M. Andersen, I. V. Bobkova, P. J. Hirschfeld, and Y. S. Barash, Phys. Rev. B **72**, 184510 (2005).

[58] D. S. Rabinovich, I. V. Bobkova, and A. M. Bobkov, Phys. Rev. Research **1**, 033095 (2019).

[59] B. M. Andersen, I. V. Bobkova, P. J. Hirschfeld, and Y. S. Barash, Phys. Rev. Lett. **96**, 117005 (2006).

[60] X. Zhou, M. Lan, Y. Ye, Y. Feng, X. Zhai, L. Gong, H. Wang, J. Zhao, and Y. Xu, Europhys. Lett. **125**, 37001 (2019).

[61] L. Bulaevskii, R. Eneias, and A. Ferraz, Phys. Rev. B **95**, 104513 (2017).

[62] H. Enoksen, J. Linder, and A. Sudbø, Phys. Rev. B **88**, 214512 (2013).

[63] C. Bell, E. J. Tarte, G. Burnell, C. W. Leung, D.-J. Kang, and M. G. Blamire, Phys. Rev. B **68**, 144517 (2003).

[64] P. Komissinskiy, G. A. Ovsyannikov, I. V. Borisenko, Y. V. Kislinskii, K. Y. Constantinian, A. V. Zaitsev, and D. Winkler, Phys. Rev. Lett. **99**, 017004 (2007).

[65] M. H. Bener, D. Tikhonov, I. A. Garifullin, K. Westerholt, and H. Zabel, J. Phys: Condens. Matter **14**, 8687 (2002).

[66] K. Y. Constantinian, Y. V. Kislinskii, G. A. Ovsyannikov, A. V. Shadrin, A. E. Sheyerman, A. L. Vasil'ev, M. Y. Presnyakov, and P. V. Komissinskiy, Phys. Solid State **55**, 461 (2013).

[67] B. L. Wu, B. M. Yang, Z. B. Guo, Y. H. Wu, and J. J. Qiu, Appl. Phys. Lett. **103**, 152602 (2013).

[68] J. J. Hauser, H. C. Theuerer, and N. R. Werthamer, Phys. Rev. **142**, 118 (1966).

[69] A. Qaiumzadeh, I. A. Ado, R. A. Duine, M. Titov, and A. Brataas, Phys. Rev. Lett. **120**, 197202 (2018).

[70] J. Železný, H. Gao, A. Manchon, F. Freimuth, Y. Mokrousov, J. Zemen, J. Mašek, J. Sinova, and T. Jungwirth, Phys. Rev. B **95**, 014403 (2017).

[71] Y. A. Bychkov and E. I. Rashba, J. Phys. C: Solid State Phys. **17**, 6039 (1984).

[72] K. Senapati, M. G. Blamire, and Z. H. Barber, Nat. Mater. **10**, 849 (2011).

[73] D. Guterding, S. Diehl, M. Altmeyer, T. Methfessel, U. Tutsch, H. Schubert, M. Lang, J. Müller, M. Huth, H. O. Jeschke, R. Valentí, M. Jourdan, and H.-J. Elmers, Phys. Rev. Lett. **116**, 237001 (2016).

[74] In this Rapid Communication, we have neglected the dependence of T_c on the direction of the order parameter, typically originating from the strong SOC present in, e.g., F–heavy metal–S structures and the proximity effects [82]. We expect that T_c can depend on the orientation of **n** in AF–heavy metal–S trilayers.

[75] See Supplemental Material at http://link.aps.org/supplemental/10.1103/PhysRevB.102.140504 for additional details on wave functions in the AF, calculation of reflection amplitudes, normal metal limit, electrical conductance, and DOS in the AF.

[76] S. Chaudhuri and P. F. Bagwell, Phys. Rev. B **51**, 16936 (1995).

[77] E. V. Bezuglyi and V. Vinokur, Phys. Rev. Lett. **91**, 137002 (2003).

[78] J. A. Sauls, Philos. Trans. R. Soc., A **376**, 20180140 (2018).

[79] T. Yokoyama, J. Linder, and A. Sudbø, Phys. Rev. B **77**, 132503 (2008).

[80] T. Vezin, C. Shen, J. E. Han, and I. Žutić, Phys. Rev. B **101**, 014515 (2020).

[81] I. Martínez, P. Högl, C. González-Ruano, J. P. Cascales, C. Tiusan, Y. Lu, M. Hehn, A. Matos-Abiague, J. Fabian, I. Žutić, and F. G. Aliev, Phys. Rev. Applied **13**, 014030 (2020).

[82] C. González-Ruano, L. G. Johnsen, D. Caso, C. Tiusan, M. Hehn, N. Banerjee, J. Linder, and F. G. Aliev, Phys. Rev. B **102**, 020405(R) (2020).

Martin F. Jakobsen,[1] Kristian B. Naess,[1] Paramita Dutta,[2,3] Arne Brataas,[1] and Alireza Qaiumzadeh[1]

[1] *Center for Quantum Spintronics, Department of Physics,*
Norwegian University of Science and Technology, NO-7491 Trondheim, Norway
[2] *Department of Physics and Astronomy, Uppsala University, Box 516, S-751 20 Uppsala, Sweden**
[3] *Institute of Physics, Sachivalaya Marg, Bhubaneswar 751005, India*

WAVEFUNCTION IN THE ANTIFERROMAGNET

The AF–S junction is governed by the Bogoliubov de-Gennes (BdG) equation

$$H\psi = E\psi, \tag{1}$$

as given in the main text. Since the system is translationally invariant in the xy–plane the bulk eigenstates must be of the form

$$\psi = \chi e^{i(q_x x + q_y y)} e^{iq_z z}, \tag{2}$$

where q_x and q_y are unchanged upon reflection or transmission at the interface. By substitution of Eq. (2) into Eq. (1) for $z < 0$ we obtain

$$q_z = q_e^{\pm} = \sqrt{k_0^2 - \mathbf{q}_\parallel^2 \pm \frac{2m}{\hbar^2}\sqrt{(E + \mu_{\mathrm{AF}})^2 - J^2}}, \tag{3a}$$

$$q_z = q_h^{\pm} = \sqrt{k_0^2 - \mathbf{q}_\parallel^2 \pm \frac{2m}{\hbar^2}\sqrt{(E - \mu_{\mathrm{AF}})^2 - J^2}}, \tag{3b}$$

where $\mathbf{q}_\parallel = (q_x, q_y)$, and

$$
\begin{aligned}
&\underline{q_z = q_e^+ :}\\
&\chi = \chi_{e,\uparrow}^+ = \left(E + \mu_{\mathrm{AF}} + b, a, \sqrt{(\mu_{\mathrm{AF}} + E)^2 - J_0^2}, 0, 0, 0, 0, 0\right),\\
&\chi = \chi_{e,\downarrow}^+ = \left(a^*, \mu_{\mathrm{AF}} + E - b, 0, \sqrt{(\mu_{\mathrm{AF}} + E)^2 - J_0^2}, 0, 0, 0, 0\right),
\end{aligned}
\tag{4}
$$

$$
\begin{aligned}
&\underline{q_z = q_e^- :}\\
&\chi = \chi_{e,\uparrow}^- = \left(-(E + \mu_{\mathrm{AF}} + b), -a, \sqrt{(\mu_{\mathrm{AF}} + E)^2 - J_0^2}, 0, 0, 0, 0, 0\right),\\
&\chi = \chi_{e,\downarrow}^- = \left(-a^*, -(\mu_{\mathrm{AF}} + E - b), 0, \sqrt{(\mu_{\mathrm{AF}} + E)^2 - J_0^2}, 0, 0, 0, 0\right),
\end{aligned}
\tag{5}
$$

$$
\begin{aligned}
&\underline{q_z = q_h^+ :}\\
&\chi = \chi_{h,\uparrow}^+ = \left(0, 0, 0, 0, \mu_{\mathrm{AF}} - E + b, a^*, \sqrt{(\mu_{\mathrm{AF}} - E)^2 - J_0^2}, 0\right),\\
&\chi = \chi_{h,\downarrow}^+ = \left(0, 0, 0, 0, a, \mu_{\mathrm{AF}} - E - b, 0, \sqrt{(\mu_{\mathrm{AF}} - E)^2 - J_0^2}\right),
\end{aligned}
\tag{6}
$$

$$
\begin{aligned}
&\underline{q_z = q_h^- :}\\
&\chi = \chi_{h,\uparrow}^- = \left(0, 0, 0, 0, -(\mu_{\mathrm{AF}} - E + b), -a^*, \sqrt{(\mu_{\mathrm{AF}} - E)^2 - J_0^2}, 0\right),\\
&\chi = \chi_{h,\downarrow}^- = \left(0, 0, 0, 0, -a, -(\mu_{\mathrm{AF}} - E - b), 0, \sqrt{(\mu_{\mathrm{AF}} - E)^2 - J_0^2}\right).
\end{aligned}
\tag{7}
$$

Here $a = e^{i\phi} J_0 \sin\theta$ and $b = J_0 \cos\theta$. Unlike the eigenvectors of F in the F-S junctions the eigenvectors depend on the energy E, the chemical potential μ_{AF}, and the exchange interaction J_0 [1–3]. In Fig. 1 we have plotted the branches $q_{e,h}^{\pm}$, and the scattering processes we are considering.
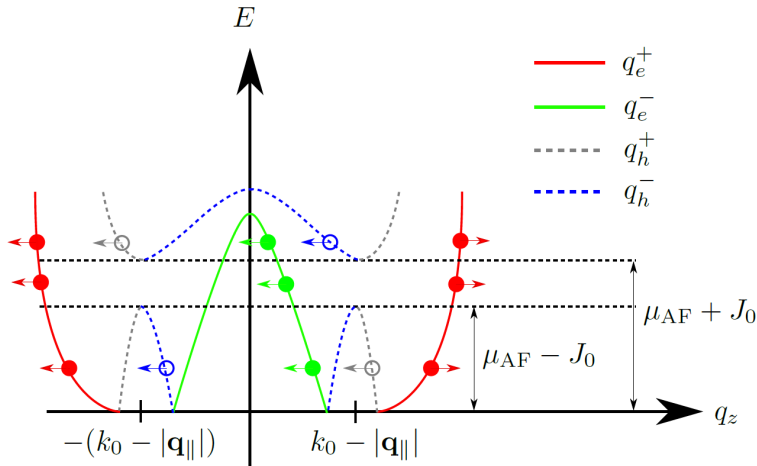

FIG. 1. The dispersion relation and the allowed scattering processes in the AF. Electrons (holes) are drawn as filled (empty) circles. The branches are parameterized as given in the figure. Incoming (reflected) particles are represented with a right (left) arrow. The new scattering processes not present in N(F)-S junctions are the ones labelled by $q_{e,h}^{-}$. The processes contributing to the conductances are the ones where $E \ll \mu_{\mathrm{AF}} - J_0$. Higher energies are suppressed by the Fermi-Dirac distribution.

The wavefunction describing an incident electron from the AF is

$$
\psi_{\mathrm{AF}} = \begin{cases} e^{iq_e^+ z}\chi_{e,\uparrow}^+ + \sum_\sigma e^{-iq_e^+ z} r_{e,\sigma}^+ \chi_{e,\sigma}^+ + r_{e,\sigma}^- e^{iq_e^- z}\chi_{e,\sigma}^- + e^{iq_h^+ z} r_{h,\sigma}^+ \chi_{h,\sigma}^+ + r_{h,\sigma}^- e^{-iq_h^- z}\chi_{h,\sigma}^-, & E < \mu_{\mathrm{AF}} - J_0 \\ e^{iq_e^+ z}\chi_{e,\uparrow}^+ + \sum_\sigma e^{-iq_e^+ z} r_{e,\sigma}^+ \chi_{e,\sigma}^+ + r_{e,\sigma}^- e^{iq_e^- z}\chi_{e,\sigma}^- + e^{-iq_h^+ z} r_{h,\sigma}^+ \chi_{h,\sigma}^+ + r_{h,\sigma}^- e^{iq_h^- z}\chi_{h,\sigma}^-, & E > \mu_{\mathrm{AF}} - J_0 \end{cases} \tag{8}
$$

where $r_i^{\pm}$ represents the reflection amplitude for a particle being reflected to the branch $q_i^{\pm}$ with $i = e, h$. For small temperatures $T < T_c$ the Fermi-Dirac distribution makes sure that only the scattering processes with $E \ll \mu_{\mathrm{AF}} - J_0$ contributes to the electrical and thermal conductance. The sign in the exponents are determined by the z–component of the group velocity $v_z = \partial E/\partial q_z$ of the corresponding branch in Fig. 1.

CALCULATING THE REFLECTION AMPLITUDES

By requiring that the wavefunction is continuous and integrating the BdG equation from $z = 0^-$ to $z = 0^+$ we obtain the matching conditions

$$
\begin{aligned}
&\psi_{\mathrm{AF}}\big|_{z=0} = \psi_S\big|_{z=0}, \\
&\frac{\hbar^2}{2m} \tau_z \otimes \sigma_x \otimes s_0 \left(\frac{d\psi_{\mathrm{AF}}}{dz}\bigg|_{z=0} - \frac{d\psi_S}{dz}\bigg|_{z=0} \right) = \left(V\tau_z \otimes \sigma_0 \otimes s_0 + \lambda_0 \tau_4^+ \otimes \sigma_x \otimes [(\boldsymbol{s} \times \boldsymbol{q}) \cdot \hat{z}] \right) \psi_S(0).
\end{aligned} \tag{9}
$$

Here ψ_{AF} and ψ_S denotes the wavefunction in the AF and S respectively. We use these equations to calculate the reflection amplitudes in Eq. (8).

PROBABILITY AND CHARGE CURRENT

Let Φ be an arbitrary eigenvector of the Hamiltonian. By defining the probability and charge density as $\rho_p = \Phi^\dagger \Phi$ and $\rho_C = e(|\Phi_1|^2 + |\Phi_2|^2 + |\Phi_3|^2 + |\Phi_4|^2 - |\Phi_5|^2 - |\Phi_6|^2 - |\Phi_7|^2 - |\Phi_8|^2)$ we evaluate $d\rho_{p,Q}/dt$ using the BdG equation

to obtain the probability and charge currents

$$J_p = \frac{\hbar}{m} \sum_{i=1,2} \text{Im}\left(\Phi_i^* \partial_z \Phi_{i+2} + \Phi_{i+2}^* \partial_z \Phi_i\right) - \frac{\hbar}{m} \sum_{j=5,6} \text{Im}\left(\Phi_j^* \partial_z \Phi_{j+2} + \Phi_{j+2}^* \partial_z \Phi_j\right),$$

$$J_C = \frac{e\hbar}{m} \sum_{i=1,2} \text{Im}\left(\Phi_i^* \partial_z \Phi_{i+2} + \Phi_{i+2}^* \partial_z \Phi_i\right) + \frac{e\hbar}{m} \sum_{j=5,6} \text{Im}\left(\Phi_j^* \partial_z \Phi_{j+2} + \Phi_{j+2}^* \partial_z \Phi_j\right). \tag{10}$$

We use J_p to evaluate the reflection probabilities $R_{i,\sigma}^{\pm}$ in the main text. The heat current is identical to the probability current except it includes a prefactor of $E - \mu$, for a detailed discussion see [4]. The charge and heat conductances in the main text are obtained from the charge and heat current by utilizing the BTK formalism [4, 5].

THE NORMAL METAL LIMIT

A crucial difference between the the N-S and AF-S junctions in our work is that the former has one physical lattice, while the latter has two physical sublattices. This results in that taking the limit $J_0 \to 0$ can be subtle.

In Fig. 2 a) we have plotted the dispersion $\epsilon_N = \frac{\hbar^2}{2m}(q^2 - k_0^2)$ which is valid in N. From the band diagram we can see that there are only two reflection processes that are possible: NR (red) and AR (gray).

In Fig. 2 b) we have plotted the dispersions $\epsilon_{AF} = \pm\sqrt{\left(\frac{\hbar}{2m}(q^2 - k_0^2)\right)^2 + J_0^2}$ in the AF, where there are two sublattices. The gap is given by $2J_0$. From the band diagram we see that we obtain two additonal reflection processes indicated by the empty blue and filled green circles.

When we naively take the limit $J_0 \to 0$ we obtain the two bands $\epsilon_{AF} = \pm\frac{\hbar^2}{2m}(q^2 - k_0^2)$ shown in Fig. 2 c). However, since the physics in Fig. 2 a) and c) should be the same it is clear that the band $\epsilon_{AF} = -\frac{\hbar^2}{2m}(q^2 - k_0^2)$ is unphysical. We confirm in the main text that the additional AR and NR associated with the unphysical band is zero in the limit $J_0 \to 0$.
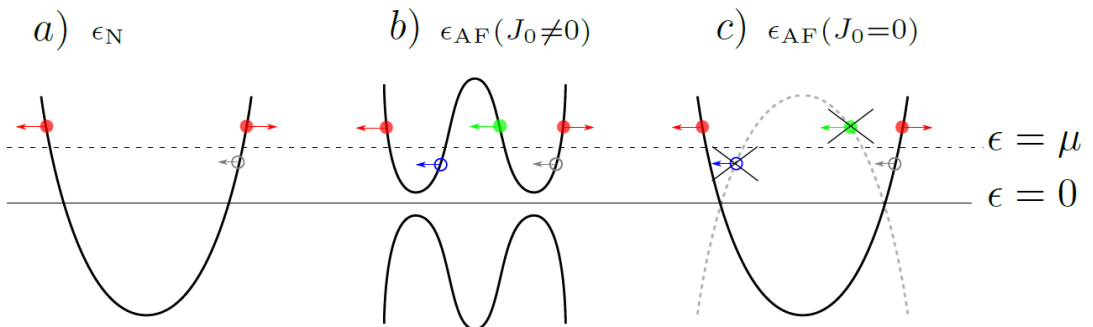

FIG. 2. The filled (empty) circles represents particles (holes). Incident (reflected) particles are represented by a right (left) arrow. a) The dispersion relation $\epsilon_N = \frac{\hbar^2}{2m}(q^2 - k_0^2)$ in N. Here only specular NR and retro AR is possible. b) The dispersion relation $\epsilon_{AF} = \pm\sqrt{\left(\frac{\hbar}{2m}(q^2 - k_0^2)\right)^2 + J_0^2}$ in AF, with two sublattices. In this case the additional scattering processes (green and blue) are allowed, because there are no redundancies in the degrees of freedom associated with the lattice. Physically the green and blue circles correspond to retro NR and specular AR. c) Naively taking the limit $J_0 \to 0$ gives the dispersion relations $\epsilon_{AF} = \pm\frac{\hbar^2}{2m}(q^2 - k_0^2)$ in the AF. Note that there is an additional band, due to the two sublattices compared to a). The crossed out green (filled) and blue (empty) circles represents the scattering processes that are allowed in the AF-S junction but absent in the N-S junction.

THE BEHAVIOR OF THE ELECTRICAL CONDUCTANCE

In order to understand the dependence of the angle of incidence it is useful to employ the Andreev approximation, which utilizes that E and Δ_0 typically is much smaller than μ and J_0. In the AF the Andreev approximation reads

$q_e^\pm \approx q_h^\pm \approx q_\pm$, where

$$q_\pm = \sqrt{k_0^2 - \mathbf{q}_\parallel^2 \pm \frac{2m}{\hbar^2}\sqrt{\mu_{\mathrm{AF}}^2 - J_0^2}}. \tag{11}$$

This equation result in two critical angles defined implicitly by the inequality

$$\mathbf{q}_\parallel^2 < k_0^2 \pm \frac{2m}{\hbar^2}\sqrt{\mu^2 - J_0^2} \equiv k_\pm^2. \tag{12}$$

We stress that the critical angle corresponding to k_- plays no role in the N(F)-S junction because it originates from the unphysical dispersion $\epsilon_{\mathrm{AF}}(J_0 = 0) = -\frac{\hbar^2}{2m}(q^2 - k_0^2)$, as discussed in the previous section. To elucidate the importance of the additional critical angle we have plotted the reflection coefficients as function of $q_\parallel$ and J_0/Δ_0 in Fig. 3 for $Z = 0$.
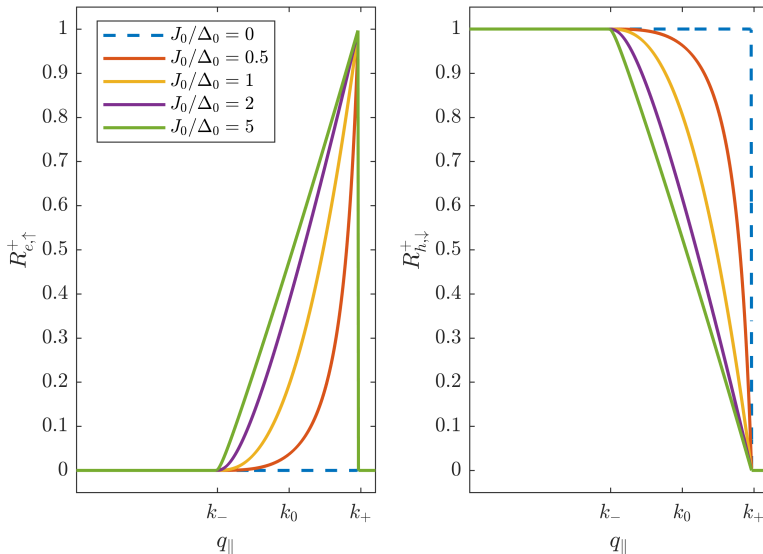

FIG. 3. Specular NR and retro AR as a function of $q_\parallel$. Note that in the regime $k_- < q_\parallel < k_+$, specular NR is enhanced and retro AR is suppressed when $J_0/\Delta_0 \neq 0$, even in the transparent limit $Z = 0$.

Note that as soon as $q_\parallel > k_-$ and $J_0 \neq 0$ the retro AR decays, while the specular NR increases. This behaviour results in the rapid decay of the electrical conductance shown in Fig. 4 in the main text. When $Z \neq 0$ this effect vanishes because the barrier enhances specular NR and suppresses retro AR. In the case $J_0 = 0$ the critical angle defined by k_- plays no role in the scattering problem, and we obtain perfect retro AR.

Note that in the regime where $\Delta_0 \lesssim J_0 \ll \mu$ we can approximate the retro AR as

$$R_h^+ = 1 - R_e^+ \approx \begin{cases} 1, & \text{if } q_\parallel < k_- \\ \frac{k_+ - q_\parallel}{k_+ - k_-}, & \text{if } q_\parallel \geq k_-. \end{cases} \tag{13}$$

This allows us to estimate the constant value of the zero-temperature conductance discussed in Fig. 4 in the main text. In this regime we obtain

$$\tilde{G}_C \approx \frac{2}{3}\left\{ 1 + \left(\frac{k_-}{k_+}\right) + \left(\frac{k_-}{k_+}\right)^2 \right\} \approx 1.71 \tag{14}$$

where we made the approximation $J_0 \ll \mu$ such that $k_\pm \approx k_0^2 \pm k_{\mathrm{F}}^2$. We also provide an estimate for how quickly $\tilde{G}_c$ decays as a function of J/Δ_0, by performing a curve fit with the function

$$\tilde{G}_C \approx \alpha \left(J_0/\Delta_0\right)^\beta + \zeta. \tag{15}$$

The results are provided in Tab. I.

TABLE I. The numerical values of the parameters in Eq. (15) for $\tilde{G}_C$. The brackets $(\dots)$ give the 95% confidence interval.

Parameter	Value	95%-Interval
α	0.118	$(0.117, 0.119)$
β	-1.013	$(-1.025, -1.001)$
ζ	1.703	$(1.702, 1.703)$

DENSITY OF STATES

The density of states (DOS) in the AF is defined as

$$D(\epsilon) = \int \frac{d^3q}{(2\pi)^3} \delta(\epsilon - \epsilon_{\mathrm{AF}}(q)). \tag{16}$$

In the AF $\epsilon_{\mathrm{AF}}(q) = \pm\sqrt{\left(\frac{\hbar^2}{2m}\left(q^2 - k_0^2\right)\right)^2 + J_0^2}$ which gives

$$D(\epsilon, J_0) = \frac{\Theta(|\epsilon| - J_0)}{2\pi^2} \frac{m}{\hbar^2} \frac{|\epsilon|}{\sqrt{\epsilon^2 - J_0^2}} \left[\sqrt{k_0^2 + \frac{2m}{\hbar^2}\sqrt{\epsilon^2 - J_0^2}} + \sqrt{k_0^2 - \frac{2m}{\hbar^2}\sqrt{\epsilon^2 - J_0^2}} \right]. \tag{17}$$

In Fig. 4 we have plotted the DOS in N and AF for $J_0/\mu = 0.75$. Note that the divergence at $\epsilon = J_0 \neq 0$ induces a strong asymmetry around the chemical potential, which increases with J_0, in the DOS. The asymmetry comes from the additional curvature of the dispersion in the AF, that we have sketched in Fig. 2 b). This growing asymmetry results in that AR is reduced when J_0 increases. We emphasize that the asymmetry present in the AF is fundamentally different from the one present in F, which is induced by the exchange spin-splitting of the energy bands. For energies $\epsilon < J_0$ the system behaves as a AF insulator, and no carriers are allowed to move.
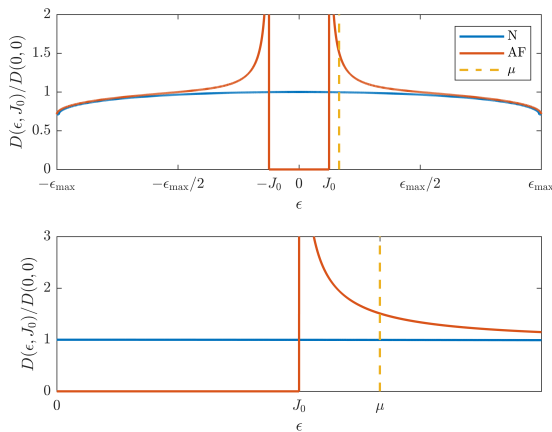

FIG. 4. DOS in N and AF. The maximum energy is $\epsilon_{\max} = \sqrt{(\hbar^2 k_0^2/2m)^2 + J_0^2}$. We have normalized the DOS with respect to its value in the normal metal at $\epsilon = 0$. When $J_0 \neq 0$ there is a strong asymmetry caused by the non-parabolic band in the AF.

INDIVIDUAL AMR CONTRIBUTIONS

In Fig. 5 we have resolved the total AMR, given in the main text, into its individual contributions. The specular
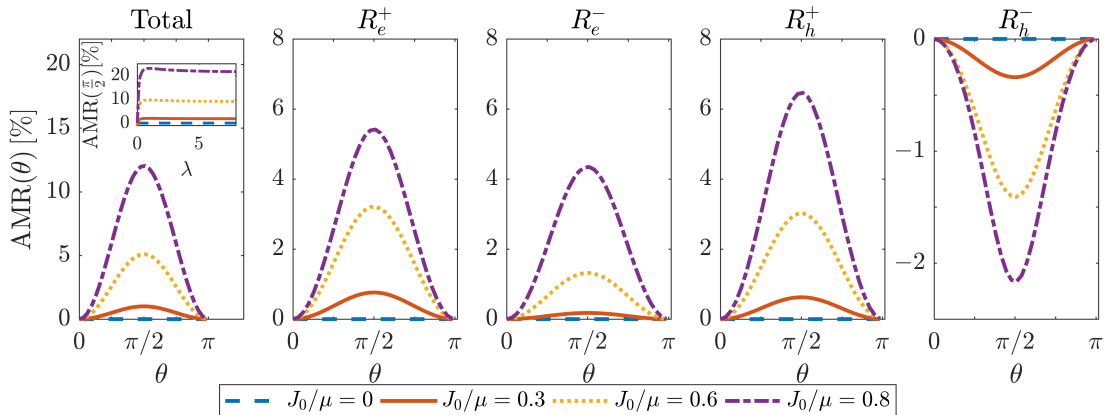

FIG. 5. The total and individual contributions to electrical AMR in an AF–S junction as a function of the orientation θ of the Néel vector and the exchange strength J_0/μ. The inset show the dependence of the AMR maxima on the RSOC strength λ.

NR and retro AR increases the AMR. The additional scattering processes retro NR and specular AR increases and decreases the AMR respectively. The AMR occurs due to the complicated interplay between the interfacial Rashba spin-orbit coupling and the direction of the Néel vector in the AF.

We find that the the new scattering processes $R_{e,h}^-$ suppresses the conductance. This is another essential difference when compared to the AMR in F–S junctions, and might lead to experimentally well-distinct variations of the AMR amplitudes.

---

* Present address
[1] M. J. M. de Jong and C. W. J. Beenakker, Phys. Rev. Lett. **74**, 1657 (1995).
[2] P. Högl, A. Matos-Abiague, I. Žutić, and J. Fabian, Phys. Rev. Lett. **115**, 116601 (2015).
[3] P. Dutta, A. Saha, and A. M. Jayannavar, Phys. Rev. B **96**, 115404 (2017).
[4] R. A. Riedel and P. F. Bagwell, Phys. Rev. B **48**, 15198 (1993).
[5] G. E. Blonder, M. Tinkham, and T. M. Klapwijk, Phys. Rev. B **25**, 4515 (1982).

Paper [3]

Martin F. Jakobsen, Arne Brataas, and Alireza Qaiumzadeh

"Electrically controlled crossed Andreev reflection in two-dimensional antiferromagnets"

Electrically Controlled Crossed Andreev Reflection in Two-Dimensional Antiferromagnets

Martin F. Jakobsen©, Arne Brataas, and Alireza Qaiumzadeh©

Center for Quantum Spintronics, Department of Physics, Norwegian University of Science and Technology, NO-7491 Trondheim, Norway

We report generic and tunable crossed Andreev reflection (CAR) in a superconductor sandwiched between two antiferromagnetic layers. We consider recent examples of two-dimensional magnets with hexagonal lattices, where gate voltages control the carrier type and density, and predict a robust signature of perfect CAR in the nonlocal differential conductance with one electron-doped and one hole-doped antiferromagnetic lead. The magnetic field-free and spin-degenerate CAR signal is electrically controlled and visible over a large voltage range, showing promise for solid-state quantum entanglement applications.

Introduction.—In quantum mechanics, identical particles can form entangled pairs sharing a common wave function: a measurement performed on one particle predetermines the state of the other. Entanglement is a unique quantum effect and was first experimentally verified using pairs of linearly polarized photons [1,2]. Currently, entangled states play a vital role in quantum computing, communication, and cryptography technologies [3,4]. Nevertheless, large-scale societal implementation requires entanglement in solid-state devices over long distances.

Electrons in a Cooper pair can be spatially separated, but remain spin and momentum entangled via a process called Cooper pair splitting [5–7]. The time-reversed process is called crossed Andreev reflection (CAR) or nonlocal Andreev reflection. CAR is the nonlocal process of converting an incoming electron from one voltage-biased lead into an outgoing hole in another grounded lead via Cooper pair formation in a grounded superconductor [8,9]. This process requires the distance between the two leads to be comparable to or shorter than the superconducting coherence length. A significant disadvantage in current state-of-the-art technology is that two detrimental processes often mask the CAR signal: (i) nonlocal electron cotunneling (CT) between the two leads and (ii) local Andreev reflection (AR) in the voltage-biased lead. The optimal solution, is to design a system that suppresses CT and AR signals while enhancing CAR signals.

Presently, numerous superconducting heterostructures have been proposed to enhance CAR signals utilizing different leads, such as normal metals (NMs) [10–13], ferromagnetic (FM) metals [9,14–17], two-dimensional (2D) graphene [18,19], and topological insulators [20–25]. Conclusive experimental detection of CAR signals remains challenging, but progress has been made by utilizing NM leads [26–31], FM leads [32–36], quantum dots [37–43], and very recently, graphene-based systems with opposite doping

levels in the two leads [5,44]. Nevertheless, most proposals require fine-tuning of the electronic structure and bias voltage. Furthermore, there are two additional disadvantages associated with FM leads: First, stray fields limit the potential use of FM systems in high-density applications. Second, although in FM half metal leads, it is possible to enhance the CAR signal when the magnetization of two leads is antiparallel, the spin entanglement of the electrons is simultaneously lost [14,19].

In this Letter, we propose utilizing 2D metallic antiferromagnetic leads, to overcome these issues. Although antiferromagnetic systems are magnetically staggered ordered systems, they have negligible stray fields and their degenerate spin states preserve entanglement.

Recently, antiferromagnets have revealed potential in superconducting spintronics. For instance, at the antiferromagnet-superconductor interface, normal electron reflection (NR) and AR have been demonstrated to be both specular and retroreflective [45–59]. In heterostructures, these anomalous processes fundamentally change the behavior of the electrical and thermal conductance [45]. In Josephson junctions, atomic-scale 0-π transitions [47–52] are predicted to occur. The existence of Josephson effects has been experimentally verified [53–59], but the remaining theoretical predictions have yet to be explored.

Herein, we investigate the suitability of an antiferromagnet-superconductor-antiferromagnet (AF-S-AF) junction with a 2D hexagonal lattice as a platform for experimental detection and quantum applications of CAR signals. Our model is general and applicable to systems in which antiferromagnetism and superconductivity are either intrinsic to the material or induced by proximity. We find a gate-controllable window in parameter space, wherein both CT and AR signals can be completely suppressed in favor of the CAR signal. This robust experimental signature is expected to be directly measurable over a wide range of applied bias

voltages. Our prediction of enhanced CAR signals in antiferromagnetic-based devices combined with recent experimental advances in graphene-based junctions [5,44] open a unique opportunity to realize efficient large-scale Cooper pair splitters with immediate applications in solid-state quantum entanglement technology.

Model.—We consider a superconductor of length L_S sandwiched between two semi-infinite 2D antiferromagnetic metals with hexagonal lattices, forming a 2D AF-S-AF junction along the x direction, as shown in Fig. 1. The left lead (AF$_0$), the superconductor (S), and the right lead (AF$_1$) occupy the regions $x < -L_S/2$, $-L_S/2 < x < L_S/2$, and $x > L_S/2$, respectively. The dynamics of charge carriers around the K point in the Brillouin zone are governed by an eigenvalue problem $H(x)\Psi(x) = E\Psi(x)$, where

$$H(x) = \begin{bmatrix} H_{AF}^e(x) - E_F(x) & \tilde{\Delta}(x) \\ \tilde{\Delta}^\dagger(x) & H_{AF}^h(x) + E_F(x) \end{bmatrix} \quad (1)$$

is the mean-field Bogoliubov–de Gennes (BdG) Hamiltonian [60,61], and $E_F(x)$ is the local Fermi energy. In 2D systems, $E_F(x)$ may be tuned by a gate voltage.

In the BdG Hamiltonian, the dynamics of low-energy itinerant charge carriers in the hexagonal antiferromagnetic leads around the K point are described by an effective Dirac-like Hamiltonian for the electron subsector

FIG. 1. The scattering processes in the AF-S-AF junction. We assume that AF$_0$ is biased with voltage V, while S and AF$_1$ are grounded. An incoming electron in AF$_0$ may undergo (i) NR, (ii) AR, (iii) CT, or (iv) CAR. NR and AR contribute to the local conductance measured in AF$_0$, and CT and CAR contribute to the nonlocal conductance measured in AF$_1$.

$H_{AF}^e = H_p + H_{sd}$ and the hole subsector $H_{AF}^h = -H_p - H_{sd}^T$, where T denotes the transpose operator. The kinetic Hamiltonian of the antiferromagnet is

$$H_p(x) = v_F s_0 \otimes (\boldsymbol{\sigma} \cdot \boldsymbol{p}), \quad (2)$$

where v_F, $\boldsymbol{p} = -i\hbar(\partial_x, \partial_y)$, and $\hbar$ denote the Fermi velocity, 2D momentum operator, and reduced Planck constant, respectively. In our notation, $\boldsymbol{\sigma}$ and s denote the Pauli matrices in sublattice and spin space, respectively. The antiferromagnetic s-d exchange interactions between localized magnetic moments and itinerant electron spins are described by

$$H_{sd}(x) = J(x)[\boldsymbol{n}(x) \cdot \boldsymbol{s}] \otimes \sigma_z. \quad (3)$$

Here, $J(x)$ and $\boldsymbol{n}(x)$ denote the exchange strength and staggered Néel vector direction, respectively. We consider single-domain and collinear AFs with a uniform Néel vector in each lead, $\boldsymbol{n}(x) = \boldsymbol{n}_j$, where the index $j = \{0,1\}$ refers to the lead AF$_j$. The misalignment angle between the Néel vectors is $\delta\gamma = \arccos(\boldsymbol{n}_0 \cdot \boldsymbol{n}_1)$. The eigenenergies of the 2D antiferromagnetic hexagonal Hamiltonian $H_{AF}^{e(h)}$ are $E_{AF} = \pm\sqrt{(\hbar v_F \boldsymbol{k})^2 + J^2}$, where $\boldsymbol{k}$ is the 2D wave vector and $+$ and $-$ refer to the conduction and valence bands, respectively. Thus, the itinerant charge carriers around the K point behave like massive Dirac particles with a band gap of magnitude $2J$ induced by the antiferromagnetic s-d exchange interaction (see Fig. 2).

We consider an s-wave superconductor described by BCS theory where the superconducting gap in the two-sublattice space is

$$\tilde{\Delta}(x) = i s_y \otimes \Delta(x)\sigma_0. \quad (4)$$

The superconducting coherence length is given by $\xi = \hbar v_F/\Delta$, which estimates the Cooper pair size. The mean-field requirement of superconductivity is that the local Fermi energy in the superconductor, E_{FS}, is much larger than the superconducting gap.

To illustrate the main concepts, and for clarity and simplicity, we assume that all energy scales exhibit the step-function behavior:

$$\{J(x), E_F(x), \Delta(x)\} = \begin{cases} \{J_0, E_{F0}, 0\}, & x < -\frac{L_S}{2}, \\ \{0, E_{FS}, \Delta_0\}, & -\frac{L_S}{2} < x < \frac{L_S}{2}, \\ \{J_1, E_{F1}, 0\}, & x > \frac{L_S}{2}, \end{cases}$$

$$(5)$$

where $\{J_j, E_{Fj}, E_{FS}, \Delta_0\}$ are constants and $j = \{0,1\}$ refers to the lead AF$_j$. We also assume that $E_{FS} \gg E_{Fj}$, and that the interfaces are magnetically compensated and

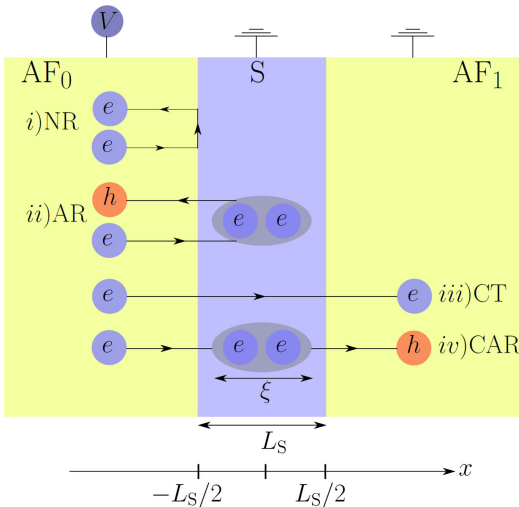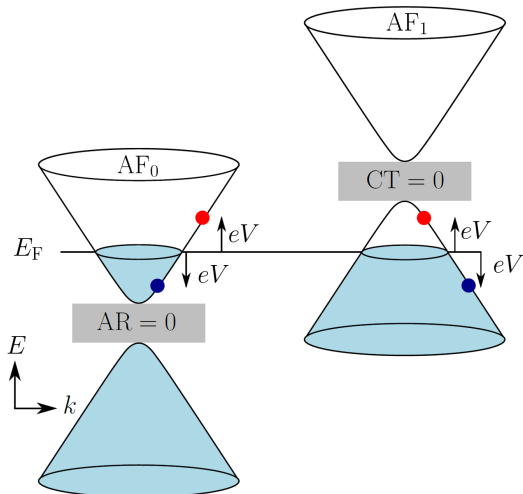FIG. 2. The "relativistic" dispersions of itinerant electrons in 2D antiferromagnetic hexagonal lattices in the leads AF_0 and AF_1 are shown to the left and right, respectively. Electrons (holes) are denoted by red (blue) circles. It is possible to block both AR and CT signals to favor CAR signals by tuning the local Fermi energy close to the gap induced by the antiferromagnetic exchange interaction (gray region).

ideal. Interface effects are discussed in the Supplemental Material (SM) [62].

Local and nonlocal conductance.—We consider that AF_0 is biased with voltage V, while S and AF_1 are grounded. Consequently, a local and nonlocal conductance can be measured in AF_0 and AF_1, respectively. To determine the local and nonlocal conductance, we consider a scattering problem with an incident electron from AF_0. In general, the allowed scattering processes are (i) local NR, (ii) local AR, (iii) nonlocal CT, and (iv) nonlocal CAR, as shown schematically in Fig. 1. Using the Blonder-Tinkham-Klapwijk formalism [63], the local conductance

$$G_L = \sum_{s=\uparrow,\downarrow} \int_{-\infty}^{\infty} d\varepsilon \left(-\frac{\partial f}{\partial \varepsilon}\right) G_0^s (2 - G_{NR}^s + G_{AR}^s) \quad (6)$$

is determined by NR and AR, while the nonlocal conductance

$$G_{NL} = \sum_{s=\uparrow,\downarrow} \int_{-\infty}^{\infty} d\varepsilon \left(-\frac{\partial f}{\partial \varepsilon}\right) G_1^s (G_{CT}^s - G_{CAR}^s) \quad (7)$$

is determined by CT and CAR. Note that CT and CAR contribute with opposite signs in Eq. (7). Herein, s denotes the spin degree of freedom, and G_j^s is the intrinsic conductance of the lead AF_j. The Fermi-Dirac distribution of incident electrons in AF_0 at temperature T is denoted by

$f = (e^{\beta(\varepsilon - eV)} + 1)^{-1}$, where β is the thermodynamic beta and e is the elementary charge. Explicitly,

$$G_{NR(AR)}^s = \int_{-\pi/2}^{\pi/2} d\theta \cos\theta R_{e(h)}^s,$$

$$G_{CT(CAR)}^s = \int_{-\pi/2}^{\pi/2} d\theta \cos\theta T_{e(h)}^s, \quad (8)$$

where $R_{e(h)}^s$ and $T_{e(h)}^s$ are the spin-dependent probabilities of NR (AR) and CT (CAR), respectively, and θ is the angle of incidence for the incoming electron (see SM [62]). In the following, we consider the zero temperature limit.

CAR enhancement.—As mentioned above, the antiferromagnetic s-d exchange interaction induces a band gap of $2J_j$ in each lead AF_j. When a gate voltage is used to tune the local Fermi energy E_{Fj}, it is possible to control the contributions of different scattering processes to the total nonlocal conductance. As an example, consider the case in which $E_{F0} = -E_{F1} = E_F > J_j > 0$, where AF_0 is electron doped and AF_1 is hole doped, as depicted in Fig. 2. In this case, CT is completely suppressed for bias voltages in the interval $E_F - J_1 < eV < E_F + J_1$. Furthermore, if we set $J_0 = J_1 = E_F$ and $E_F/\Delta_0 > 1/2$, then the CAR signal becomes dominant for all voltages in the subgap regime, $eV/\Delta_0 < 1$.

To study the CAR-dominant regime, we set $J_0 = J_1 = J = E_F > 0$, where both AR and CT processes are suppressed simultaneously. For concreteness, we fix the length of the superconductor to its coherence length $L_S = \xi$ and assume that the Néel vectors in the two leads are parallel $\mathbf{n}_0 = \mathbf{n}_1$. In Fig. 3(a), we plot the normalized nonlocal conductance $\mathcal{G}_{NL} = G_{NL}/\sum_s G_1^s$ at zero temperature as a function of the voltage bias eV/Δ_0 for the AF-S-AF junction. If the applied voltage is less than the superconducting gap, that is, $eV/\Delta_0 < 1$, both the CT and AR signals are completely suppressed due to the antiferromagnetic exchange gap. In this regime, the nonlocal conductance is negative, and thus, the CAR signal is dominant. The amplitude of the nonlocal conductance depends strongly on L_S/ξ; see the SM [62].

Thus far, we have considered the Néel vectors to be parallel. We show in the inset in Fig. 3(a) that the amplitude of the total nonlocal conductance varies with the misalignment angle between the two Néel vectors, while its sign remains unchanged. We attribute this anisotropic CAR signal to the opening of spin-flip channels during the scattering processes.

For completeness, we compare our result for 2D antiferromagnetic hexagonal leads, as shown in Fig. 3(a), with those of nonmagnetic graphene and 2D ferromagnetic hexagonal leads, which have previously been reported in the literature [14,18].

In Fig. 3(b), we plot the nonlocal conductance of an NM-S-NM heterostructure, where NM is a graphene layer,
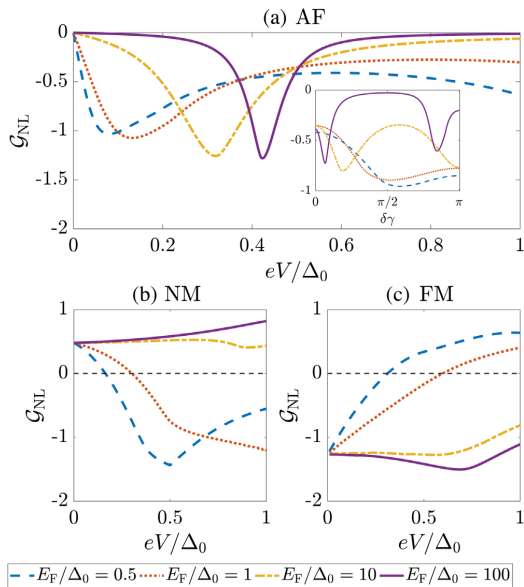
FIG. 3. The total nonlocal conductance in CAR-dominant configurations as a function of the applied voltage bias for different 2D hexagonal heterostructures. (a) An AF-S-AF system with parallel Néel vectors and opposite charge doping in the leads, (b) an NM-S-NM system with opposite charge doping in the leads, and (c) an FM-S-FM system with antiparallel magnetization vectors and the same charge doping in the leads. The inset in (a) shows the angular dependence of the nonlocal conductance versus the misalignment between the Néel vectors in the two leads $\delta\gamma = \arccos(n_0 \cdot n_1)$, with an applied voltage bias $eV/\Delta_0 = 0.5$. In all figures, we have set the AF (FM) s-d exchange interaction equal to the Fermi energy in both leads.

by setting $J = 0$ in the BdG Hamiltonian (1). In this case, AR and CT are completely suppressed only at $eV = E_F < \Delta_0$ [18]. For other bias voltages, competition among the AR, CT, and CAR signals occurs, which, for certain parameters, can lead to a negative nonlocal conductance, as shown in Fig. 3(b). In contrast, the nonlocal conductance in the AF-S-AF junction is negative for all subgap voltages under the conditions $E_F = J$ and $E_F/\Delta_0 > 1/2$. In the NM-S-NM junction, the CAR dominant signal is predicted only when the local Fermi energy is smaller than the superconducting gap. In this regime, inevitable spatial fluctuations in the carrier density, and consequently, the local Fermi energy, in graphene layers are larger than the superconducting gap and hinder experimental detection of CAR signals [44,64]. In sharp contrast, in the AF-S-AF junction, a CAR-dominant signal can be observed when the local Fermi energy is larger than the superconducting gap. We therefore expect experimental detection of the CAR-dominant signal to be considerably easier in AF-S-AF junctions than in 2D NM-S-NM junctions.

In 2D hexagonal FM-S-FM junctions, when the magnetization vectors in the two leads are parallel (antiparallel) and both leads have the same charge doping, the CT (CAR) signal dominates the total nonlocal conductance only if the ferromagnetic exchange energy is equal to the local Fermi energy and much larger than the superconducting gap [14]. These features are demonstrated in Fig. 3(c), where we plot the nonlocal conductance of a 2D FM-S-FM junction in the antiparallel configuration. As shown in the SM [62], the sign of the total nonlocal conductance in FM-S-FM junctions is very sensitive to the angle between two magnetization vectors in the leads, in contrast to the robustness of the sign of the total nonlocal conductance in the antiferromagnetic case. We also emphasize that in 2D hexagonal FM-S-FM junctions, a CAR-dominant regime is only achieved when the exchange interaction is fine-tuned to the Fermi energy of the ferromagnetic lead. However, in this regime, the density of states for minority spins is negligible, and thus, the electron spins in the two ferromagnetic leads cannot be totally entangled. In the antiferromagnetic leads, the spins are degenerate and truly spin-entangled particles can be generated in two spatially separated leads.

Finally, we comment on the CAR-dominated signal in the AF-S-AF junction when we relax the conditions $E_F = J$ and $E_F/\Delta_0 > 1/2$ but still maintain $J_0 = J_1 = J$ such that both AR and CT are simultaneously nonzero. Figure 4 shows a sketch of the regions in the parameter space (E_F, J), where CT and CAR contribute to the nonlocal
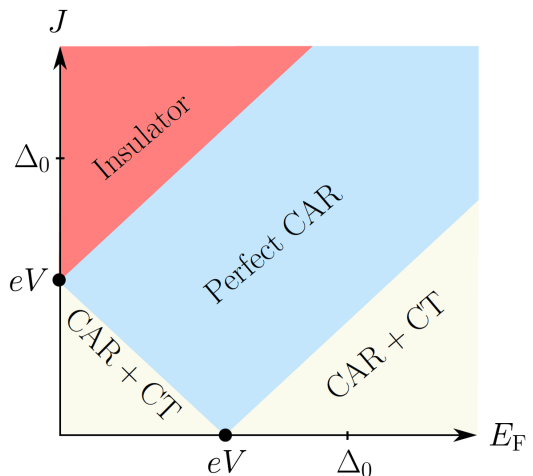

FIG. 4. Plot of the parameter space (E_F, J) of the total nonlocal conductance. In the blue region, the CAR signal dominates. In the beige regions, the CAR signal competes with CT. In the red region, the antiferromagnetic leads are insulating, and the conductance vanishes. $J = 0$ and $E_F = 0$ represent limits in which the leads are nonmagnetic graphene and undoped AFs, respectively.

conductance in the subgap regime $eV/\Delta_0 < 1$. We can achieve perfect CAR if the deviation of the gate-controlled local Fermi energy E_F from the antiferromagnetic exchange energy J is smaller than the voltage bias, as shown in the light blue region. For larger deviations, as shown in the beige region, competition between CT and CAR determines the sign of the nonlocal conductance. Gradually, CT dominates, resulting in positive nonlocal conductance for large deviations. If the exchange interaction is significantly larger than both the local Fermi energy and the voltage bias, then the system behaves as an insulator with zero conductance, as demonstrated by the red region. In the SM [62], we plot the nonlocal conductance for specific material parameters, demonstrating the general behavior shown in Fig. 4.

Concluding remarks.—We develop a general framework for nonlocal transport in a 2D AF-S-AF heterostructure. Perfect CAR is possible using a gate voltage to tune the local Fermi energy close to the exchange strength, while the two antiferromagnetic leads have opposite charge doping. Our finding is quite generic for an important class of collinear two-sublattice AF materials with either hexagonal or square lattice structure. We propose a concrete experimental requirement: the local Fermi energy deviation from the antiferromagnetic exchange strength should be smaller than the voltage bias. Typical values for the s-d exchange interaction can vary from meV to eV [65,66], the superconducting gap is typically on the meV scale [44,67], and the Fermi energy can be tuned by a gate voltage. Hence, 2D antiferromagnetic-based heterostructures exhibit highly electrically controllable Cooper pair splitting in a spin-degenerate system and enable the production of truly entangled electron pairs in solid-state quantum entanglement devices.

[1] A. Aspect, J. Dalibard, and G. Roger, Experimental Test of Bell's Inequalities Using Time-Varying Analyzers, Phys. Rev. Lett. **49**, 1804 (1982).

[2] R. Ursin, F. Tiefenbacher, T. Schmitt-Manderbach, H. Weier, T. Scheidl, M. Lindenthal, B. Blauensteiner, T. Jennewein, J. Perdigues, P. Trojek, B. Ömer, M. Fürst, M. Meyenburg, J. Rarity, Z. Sodnik, C. Barbieri, H. Weinfurter, and A. Zeilinger, Entanglement-based quantum communication over 144 km, Nat. Phys. **3**, 481 (2007).

[3] D. Loss and D. P. DiVincenzo, Quantum computation with quantum dots, Phys. Rev. A **57**, 120 (1998).

[4] R. Horodecki, P. Horodecki, M. Horodecki, and K. Horodecki, Quantum entanglement, Rev. Mod. Phys. **81**, 865 (2009).

[5] P. Pandey, R. Danneau, and D. Beckmann, Ballistic Graphene Cooper Pair Splitter, Phys. Rev. Lett. **126**, 147701 (2021).

[6] J. Fuchs, M. Barth, C. Gorini, nan Adagideli, and K. Richter, Crossed Andreev reflection in topological insulator nanowire T-junctions, arXiv:2011.01265.

[7] K. Zhang and Q. Cheng, Electrically tunable crossed Andreev reflection in a ferromagnet—superconductor—ferromagnet junction on a topological insulator, Supercond. Sci. Technol. **31**, 075001 (2018).

[8] J. M. Byers and M. E. Flatté, Probing Spatial Correlations with Nanoscale Two-Contact Tunneling, Phys. Rev. Lett. **74**, 306 (1995).

[9] G. Deutscher and D. Feinberg, Coupling superconducting-ferromagnetic point contacts by Andreev reflections, Appl. Phys. Lett. **76**, 487 (2000).

[10] G. Falci, D. Feinberg, and F. W. J. Hekking, Correlated tunneling into a superconductor in a multiprobe hybrid structure, Europhys. Lett. **54**, 255 (2001).

[11] M. S. Kalenkov and A. D. Zaikin, Nonlocal Andreev reflection at high transmissions, Phys. Rev. B **75**, 172503 (2007).

[12] J. P. Morten, D. Huertas-Hernando, W. Belzig, and A. Brataas, Full counting statistics of crossed Andreev reflection, Phys. Rev. B **78**, 224515 (2008).

[13] H. Cheraghchi, H. Esmailzadeh, and A. G. Moghaddam, Superconducting electron and hole lenses, Phys. Rev. B **93**, 214508 (2016).

[14] J. Linder, M. Zareyan, and A. Sudbø, Spin-switch effect from crossed Andreev reflection in superconducting graphene spin valves, Phys. Rev. B **80**, 014513 (2009).

[15] K. Li and Y.-Y. Zhang, Spin-filtered and spatially distinguishable crossed Andreev reflection in a silicene-superconductor junction, Phys. Rev. B **94**, 165441 (2016).

[16] R. Beiranvand, H. Hamzehpour, and M. Alidoust, Nonlocal Andreev entanglements and triplet correlations in graphene with spin-orbit coupling, Phys. Rev. B **96**, 161403(R) (2017).

[17] F. Giazotto, F. Taddei, F. Beltram, and R. Fazio, Crossed Andreev Reflection-Induced Magnetoresistance, Phys. Rev. Lett. **97**, 087001 (2006).

[18] J. Cayssol, Crossed Andreev Reflection in a Graphene Bipolar Transistor, Phys. Rev. Lett. **100**, 147001 (2008).

[19] M. Veldhorst and A. Brinkman, Nonlocal Cooper Pair Splitting in a pSn Junction, Phys. Rev. Lett. **105**, 107002 (2010).

[20] J. Nilsson, A. R. Akhmerov, and C. W. J. Beenakker, Splitting of a Cooper Pair by a Pair of Majorana Bound States, Phys. Rev. Lett. **101**, 120403 (2008).

[21] W. Chen, R. Shen, L. Sheng, B. G. Wang, and D. Y. Xing, Electron Entanglement Detected by Quantum Spin Hall Systems, Phys. Rev. Lett. **109**, 036802 (2012).

[22] W. Chen, R. Shen, L. Sheng, B. G. Wang, and D. Y. Xing, Resonant nonlocal Andreev reflection in a narrow quantum spin Hall system, Phys. Rev. B **84**, 115420 (2011).

[23] R. W. Reinthaler, P. Recher, and E. M. Hankiewicz, Proposal for an All-Electrical Detection of Crossed Andreev Reflection in Topological Insulators, Phys. Rev. Lett. **110**, 226802 (2013).

[24] J. J. He, J. Wu, T.-P. Choy, X.-J. Liu, Y. Tanaka, and K. T. Law, Correlated spin currents generated by resonant-crossed Andreev reflections in topological superconductors, Nat. Commun. **5**, 3232 (2014).

[25] J. Wang, L. Hao, and K. S. Chan, Quantized crossed-Andreev reflection in spin-valley topological insulators, Phys. Rev. B **91**, 085415 (2015).

[26] A. Kleine, A. Baumgartner, J. Trbovic, and C. Schnenberger, Contact resistance dependence of crossed Andreev reflection, Europhys. Lett. **87**, 27011 (2009).

[27] S. Russo, M. Kroug, T. M. Klapwijk, and A. F. Morpurgo, Experimental Observation of Bias-Dependent Nonlocal Andreev Reflection, Phys. Rev. Lett. **95**, 027002 (2005).

[28] P. Cadden-Zimansky and V. Chandrasekhar, Nonlocal Correlations in Normal-Metal Superconducting Systems, Phys. Rev. Lett. **97**, 237003 (2006).

[29] P. Cadden-Zimansky, J. Wei, and V. Chandrasekhar, Cooper-pair-mediated coherence between two normal metals, Nat. Phys. **5**, 393 (2009).

[30] J. Wei and V. Chandrasekhar, Positive noise cross-correlation in hybrid superconducting and normal-metal three-terminal devices, Nat. Phys. **6**, 494 (2010).

[31] A. Das, Y. Ronen, M. Heiblum, D. Mahalu, A. V. Kretinin, and H. Shtrikman, High-efficiency cooper pair splitting demonstrated by two-particle conductance resonance and positive noise cross-correlation, Nat. Commun. **3**, 1165 (2012).

[32] D. Beckmann, H. B. Weber, and H. V. Löhneysen, Evidence for Crossed Andreev Reflection in Superconductor-Ferromagnet Hybrid Structures, Phys. Rev. Lett. **93**, 197003 (2004).

[33] I. Asulin, O. Yuli, G. Koren, and O. Millo, Evidence for crossed Andreev reflections in bilayers of (100) YBa$_2$Cu$_3$O$_{7-\delta}$ and the itinerant ferromagnet SrRuO$_3$, Phys. Rev. B **74**, 092501 (2006).

[34] D. Beckmann and H. V. Löhneysen, Negative four-terminal resistance as a probe of crossed Andreev reflection, Appl. Phys. A **89**, 603 (2007).

[35] H. V. Lhneysen, D. Beckmann, F. Prez-Willard, M. Schck, C. Strunk, and C. Srgers, Proximity effect between superconductors and ferromagnets: From thin films to nanostructures, Ann. Phys. (Amsterdam) **14**, 591 (2005).

[36] P. Aronov and G. Koren, Signature of a crossed Andreev reflection effect in the magnetic response of YBa$_2$Cu$_3$O$_{7-\delta}$ junctions with the itinerant ferromagnet SrRuO$_3$, Phys. Rev. B **72**, 184515 (2005).

[37] Z. B. Tan, D. Cox, T. Nieminen, P. Lähteenmäki, D. Golubev, G. B. Lesovik, and P. J. Hakonen, Cooper Pair Splitting by Means of Graphene Quantum Dots, Phys. Rev. Lett. **114**, 096602 (2015).

[38] G. Fülöp, F. Domínguez, S. d'Hollosy, A. Baumgartner, P. Makk, M. H. Madsen, V. A. Guzenko, J. Nygård, C. Schönenberger, A. Levy Yeyati, and S. Csonka, Magnetic Field Tuning and Quantum Interference in a Cooper Pair Splitter, Phys. Rev. Lett. **115**, 227003 (2015).

[39] L. Hofstetter, S. Csonka, J. Nygård, and C. Schönenberger, Cooper pair splitter realized in a two-quantum-dot Y-junction, Nature (London) **461**, 960 (2009).

[40] L. Hofstetter, S. Csonka, A. Baumgartner, G. Fülöp, S. d'Hollosy, J. Nygård, and C. Schönenberger, Finite-Bias Cooper Pair Splitting, Phys. Rev. Lett. **107**, 136801 (2011).

[41] J. Schindele, A. Baumgartner, and C. Schönenberger, Near-Unity Cooper Pair Splitting Efficiency, Phys. Rev. Lett. **109**, 157002 (2012).

[42] L. G. Herrmann, F. Portier, P. Roche, A. L. Yeyati, T. Kontos, and C. Strunk, Carbon Nanotubes as Cooper-Pair Beam Splitters, Phys. Rev. Lett. **104**, 026801 (2010).

[43] I. V. Borzenets, Y. Shimazaki, G. F. Jones, M. F. Craciun, S. Russo, M. Yamamoto, and S. Tarucha, High efficiency CVD graphene-lead (Pb) cooper pair splitter, Sci. Rep. **6**, 23051 (2016).

[44] G.-H. Park, K. Watanabe, T. Taniguchi, G.-H. Lee, and H.-J. Lee, Engineering crossed Andreev reflection in double-bilayer graphene, Nano Lett. **19**, 9002 (2019).

[45] M. F. Jakobsen, K. B. Naess, P. Dutta, A. Brataas, and A. Qaiumzadeh, Electrical and thermal transport in antiferromagnet-superconductor junctions, Phys. Rev. B **102**, 140504(R) (2020).

[46] I. V. Bobkova, P. J. Hirschfeld, and Yu. S. Barash, Spin-Dependent Quasiparticle Reflection and Bound States at Interfaces with Itinerant Antiferromagnets, Phys. Rev. Lett. **94**, 037005 (2005).

[47] B. M. Andersen, I. V. Bobkova, P. J. Hirschfeld, and Y. S. Barash, $0 - \pi$ Transitions in Josephson Junctions with Antiferromagnetic Interlayers, Phys. Rev. Lett. **96**, 117005 (2006).

[48] X. Zhou, M. Lan, Y. Ye, Y. Feng, X. Zhai, L. Gong, H. Wang, J. Zhao, and Y. Xu, Andreev reflection and $0 - \pi$ transition in graphene-based antiferromagnetic superconducting junctions, Europhys. Lett. **125**, 37001 (2019).

[49] L. Bulaevskii, R. Eneias, and A. Ferraz, Superconductor-antiferromagnet-superconductor π Josephson junction based on an antiferromagnetic barrier, Phys. Rev. B **95**, 104513 (2017).

[50] H. Enoksen, J. Linder, and A. Sudbø, Pressure-induced $0 - \pi$ transitions and supercurrent crossover in antiferromagnetic weak links, Phys. Rev. B **88**, 214512 (2013).

[51] B. M. Andersen, I. V. Bobkova, P. J. Hirschfeld, and Y. S. Barash, Bound states at the interface between antiferromagnets and superconductors, Phys. Rev. B **72**, 184510 (2005).

[52] D. S. Rabinovich, I. V. Bobkova, and A. M. Bobkov, Anomalous phase shift in a Josephson junction via an antiferromagnetic interlayer, Phys. Rev. Research **1**, 033095 (2019).

[53] C. Bell, E. J. Tarte, G. Burnell, C. W. Leung, D.-J. Kang, and M. G. Blamire, Proximity and josephson effects in superconductor/antiferromagnetic Nb/γ − Fe$_{50}$Mn$_{50}$ heterostructures, Phys. Rev. B **68**, 144517 (2003).

[54] P. Komissinskiy, G. A. Ovsyannikov, I. V. Borisenko, Y. V. Kislinskii, K. Y. Constantinian, A. V. Zaitsev, and D. Winkler, Josephson Effect in Hybrid Oxide Heterostructures with an Antiferromagnetic Layer, Phys. Rev. Lett. **99**, 017004 (2007).

[55] M. Hübener, D. Tikhonov, I. A. Garifullin, K. Westerholt, and H. Zabel, The antiferromagnet/superconductor proximity effect in Cr/V/Cr trilayers, J. Phys. **14**, 8687 (2002).

[56] K. Y. Constantinian, Y. V. Kislinskii, G. A. Ovsyannikov, A. V. Shadrin, A. E. Sheyerman, A. L. Vasil'ev, M. Yu. Presnyakov, and P. V. Komissinskiy, Interfaces in superconducting hybrid heterostructures with an antiferromagnetic interlayer, Phys. Solid State **55**, 461 (2013).

Electrically controlled crossed Andreev reflection in two-dimensional antiferromagnets

Martin F. Jakobsen, Arne Brataas, and Alireza Qaiumzadeh

Center for Quantum Spintronics, Department of Physics,
Norwegian University of Science and Technology, NO-7491 Trondheim, Norway

SCATTERING PROCESSES AND SNELL'S LAW

The local and nonlocal conductance in the main text is determined by the possible scattering processes available in the junction. For brevity, we here consider only the antiferromagnet–superconductor–antiferromagnet (AF–S–AF) junction where the spin is degenerate. The left (right) AF will be referred to as lead 0 (1).

Consider an incident electron (e) with angle of incidence θ in lead 0. The possible scattering processes are:

1. Reflected electron into lead 0 (NR) with angle of reflection θ_e^0.

2. Reflected hole into lead 0 (AR) with angle of reflection θ_h^0.

3. Transmitted electron into lead 1 (CT) with angle of transmission θ_e^1.

4. Transmitted hole into lead 1 (CAR) with angle of transmission θ_h^1.

Due to the translational invariance in the y-direction we can write down Snell's law for the possible scattering processes,

$$k_e^0 \sin\theta = k_e^0 \sin\theta_e^0 = k_h^0 \sin\theta_h^0 = k_e^1 \sin\theta_e^1 = k_h^1 \sin\theta_h^1. \tag{1}$$

Here the wavenumbers are

$$\hbar v_{\mathrm{F}} k_{e(h)}^j = \sqrt{(E_{\mathrm{F}j} \pm E)^2 - J_j^2}, \tag{2}$$

and the index $j = \{0, 1\}$ labels the lead. Equations (1) and (2) are used to determine the angles of reflection $\theta_{e(h)}^0$ and transmission $\theta_{e(h)}^1$, for a given angle of incidence θ. Furthermore, the scattering processes AR, CT, and CAR have the corresponding critical angles

$$\theta_{c,h}^0 = \arcsin\frac{k_h^0}{k_e^0}, \quad \theta_{c,e}^1 = \arcsin\frac{k_e^1}{k_e^0}, \quad \text{and} \quad \theta_{c,h}^1 = \arcsin\frac{k_h^1}{k_e^0}, \tag{3}$$

respectively. For angles of incidence θ greater (smaller) than a given critical angle the corresponding scattering processes is an evanescent (propagating) state, giving zero (finite) contribution to the relevant conductance.

SOLUTION ANSATZ OF THE BDG EQUATION

We can express the wavefunctions in lead 0, the superconductor, and lead 1 as

$$\Psi_0 = \Psi_{\mathrm{In}} + \sum_{s=\{\mathrm{P,AP}\}} \left(r_{e,s} \Psi_{r_{e,s}} + r_{h,s} \Psi_{r_{h,s}} \right),$$

$$\Psi_{\mathrm{S}} = \sum_{i=1}^{8} a_i \Phi_i, \tag{4}$$

$$\Psi_1 = \sum_{s=\{\mathrm{P,AP}\}} \left(t_{e,s} \Psi_{t_{e,s}} + t_{h,s} \Psi_{t_{h,s}} \right),$$

respectively. Here $\Psi_{r_{e(h),s}}$ and $\Psi_{t_{e(h),s}}$ are the eigenstates corresponding to the scattering processes NR (AR) and CT (CAR) in the leads. The eigenstates in the superconductor is denoted by Φ_i. The spin-index $s = (\mathrm{A})\mathrm{P}$ refers to the spin polarization being (anti)parallel to the Néel vector. The reflection $r_{e(h),s}$ and transmission $t_{e(h),s}$ amplitudes are then determined by requiring continuity of the wavefunction

$$\Psi_0 \left(x = -L_{\mathrm{S}}/2 \right) = \Psi_S \left(x = -L_{\mathrm{S}}/2 \right) \text{ and } \Psi_S \left(x = L_{\mathrm{S}}/2 \right) = \Psi_1 \left(x = L_{\mathrm{S}}/2 \right) \tag{5}$$

at the AF–S interfaces.

ROBUSTNESS OF THE CAR DOMINATED SIGNAL

In the main text we argued that a perfect CAR dominated signal can be obtained on the voltage interval $(0, \Delta_0)$ if the gate voltage is tuned such that $E_F = J$, and $E_F/\Delta_0 > 1/2$. We also discussed the robustness of deviations from these assumptions. If the deviation of E_F from J is greater than the voltage bias then CT dominates the sign of the nonlocal conductance. In this section, we quantitatively demonstrate the competition between CT and CAR.

In Fig. 1 we have plotted the nonlocal conductance as a function of the parameters J and E_F. Fig. 1 exhibits the general behaviour of Fig. 4 in the main text. The system is insulating when $J > eV + E_F$, and exhibits perfect CAR when $J > \pm (eV - E_F)$. When these inequalities are not satisfied there is a competition between CAR and CT, that determines the sign of the nonlocal conductance.
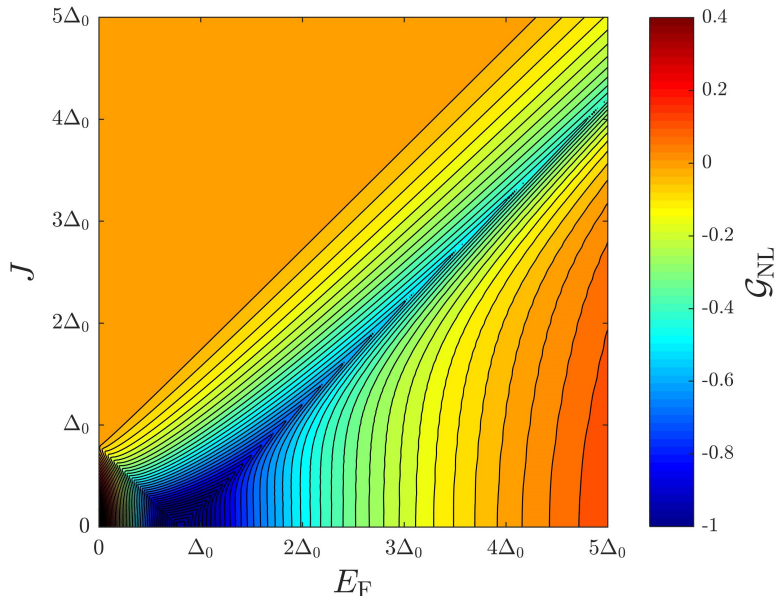

FIG. 1. Nonlocal conductance as a function of J and E_F. The figure is an example of the general behaviour discussed in Fig. 4 of the main text. We have used the concrete parameters $L_S/\xi = 1$ and $eV/\Delta_0 = 0.8$.

We can understand the general features of Fig. 1 analytically by considering the band structures of lead 1 and the superconductor in the subgap regime $eV/\Delta_0 < 1$ shown in Fig. 2. There are in total four cases to consider:

1. For $\Delta_0 < E_F - J$, CT and CAR competes for all $eV < \Delta_0$.

2. For $E_F - J < \Delta_0 < E_F + J$, we find perfect CAR if $E_F - J < eV < \Delta_0$, and competition between CT and CAR if $eV < E_F - J$.

3. For $\Delta_0 > E_F + J$, we find perfect CAR if $E_F - J < eV < E_F + J$, and competition between CT and CAR on the intervals $eV < E_F - J$ and $E_F + J < eV < \Delta_0$.

4. For $E_F < J$ and $eV < J - E_F$ the system is insulating.

By solving these inequalities in terms of J we obtain Fig. 4 in the main text.

In Fig. 3 we have plotted the contributions from CT, CAR, and the total nonlocal conductance $\mathcal{G}_{NL}$ as a function of eV/Δ_0. We have parameterized the exchange interaction as

$$J = E_F - l\,\Delta_0. \tag{6}$$

Here l is a numerical parameter that determines the deviation between E_F and J in terms of Δ_0. In Fig. 3 we have performed a parameter sweep over l. Concretely we have let l be on the interval $(0, 2)$. The figure shows that as
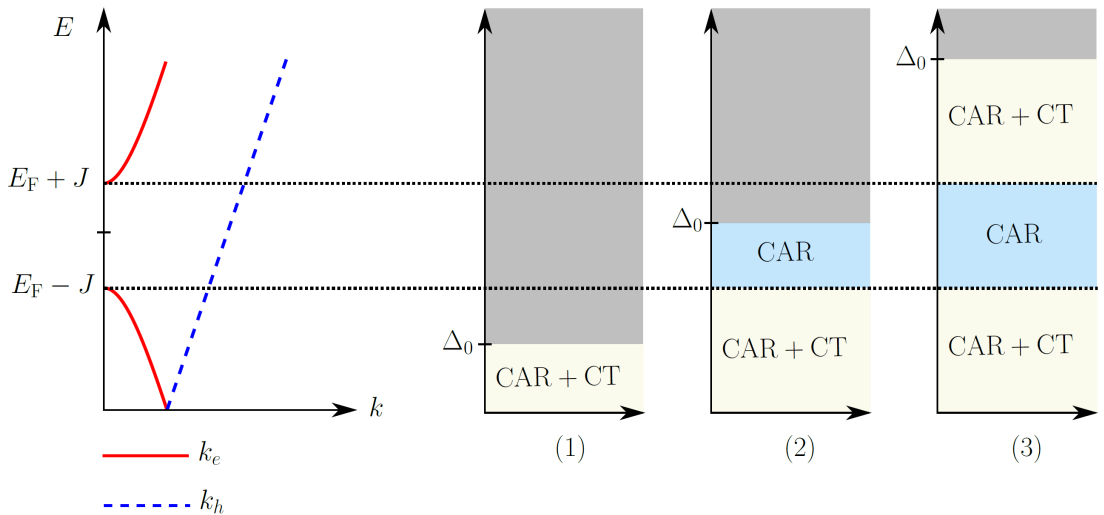
FIG. 2. The possible scattering processes allowed in lead 1, depending on the relative values of J, E_{F}, and Δ_0.

the deviation parameter increases, CT gradually starts to dominate CAR resulting in a sign change of the nonlocal conductance.
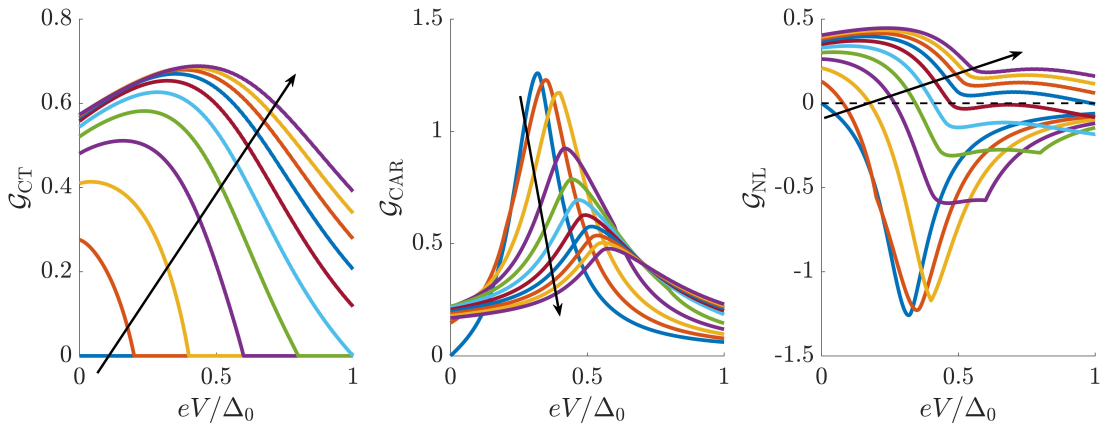

FIG. 3. A parameter sweep over the deviation parameter l. In the figure we have used the values $l = \{0, 0.2, 0.4, 0.6, 0.8, 1, 1.2, 1.4, 1.6, 1.8, 2\}$, and fixed $E_{\mathrm{F}} = 10\Delta_0$. The arrows indicate curves with increasing deviation parameter l. As the deviation parameter increases CT starts to gradually dominate CAR. Other choices of E_{F} result in the same qualitative behaviour.

OSCILLATIONS IN THE NONLOCAL CONDUCTANCE

In Fig. 4 we have plotted the nonlocal conductance $\mathcal{G}_{\mathrm{NL}}$ as a function of the length of the superconductor L_{S}/ξ, for $eV/\Delta_0 = 0.5$. We observe rapid oscillations, due to the formation of resonant transmission levels inside the superconductor. The oscillation frequency is determined by the ratio Δ_0/E_{FS}. The oscillating behaviour is also present in NM–S–NM and FM–S–FM junctions, as confirmed by previous studies referenced in the main text. Importantly, CT is suppressed for all lengths L_{S}/ξ, when $E_{\mathrm{F}} = J$ and $E_{\mathrm{F}}/\Delta_0 > 1/2$, resulting in a CAR dominant signal. The nonlocal conductance is exponentially suppressed in the limit $L_{\mathrm{S}}/\xi \to \infty$, where the spatial separation of the electrons in lead 0 and lead 1 is greater than the approximate length of a corresponding Cooper pair.
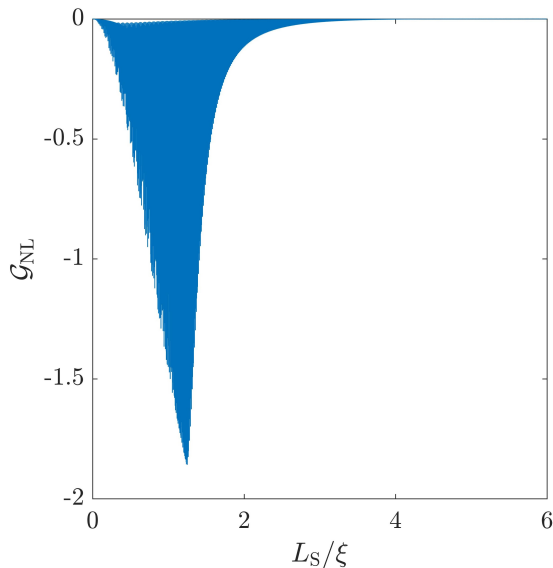

FIG. 4. Normalized nonlocal conductance $\mathcal{G}_{\mathrm{NL}}$ as a function of the length of the superconductor L_{S}/ξ. Here $\xi = \hbar v_{\mathrm{F}}/\Delta$ is the approximate length of a Cooper pair. We have set $eV/\Delta_0 = 0.5$, $E_{\mathrm{F}}/\Delta_0 = J/\Delta_0 = 10$, and $E_{\mathrm{FS}}/\Delta_0 = 1000$.

ANISOTROPY IN CONDUCTANCE

In Fig. 5 we have plotted the normalized nonlocal conductance $\mathcal{G}_{\text{NL}}$ as a function of the angle of misalignment $\delta\gamma = \arccos\left(\boldsymbol{n}_0 \cdot \boldsymbol{n}_1\right)$ between the order parameters $\boldsymbol{n}_0$ and $\boldsymbol{n}_1$ in lead 0 and lead 1 respectively. We have considered the cases where lead 1 can be: electron (hole) doped (anti)ferromagnets. We have fixed $J = E_{\text{F}} = E_{\text{F0}} = -E_{\text{F1}}$, $L_{\text{S}}/\xi = 1$, and $eV/\Delta_0 = 0.5$. In accordance with the literature mentioned in the main text we find a sign-change effect for the electron doped FM_1. Since, the energy bands are spin-degenerate in AF_1 no sign-change effect is observed. However, all magnetic junctions exhibit an anisotropy as a consequence of the misalignment between the order parameters in lead 0 and lead 1. Notice that for the hole doped AF_1 the nonlocal conductance is negative for any misalignment.
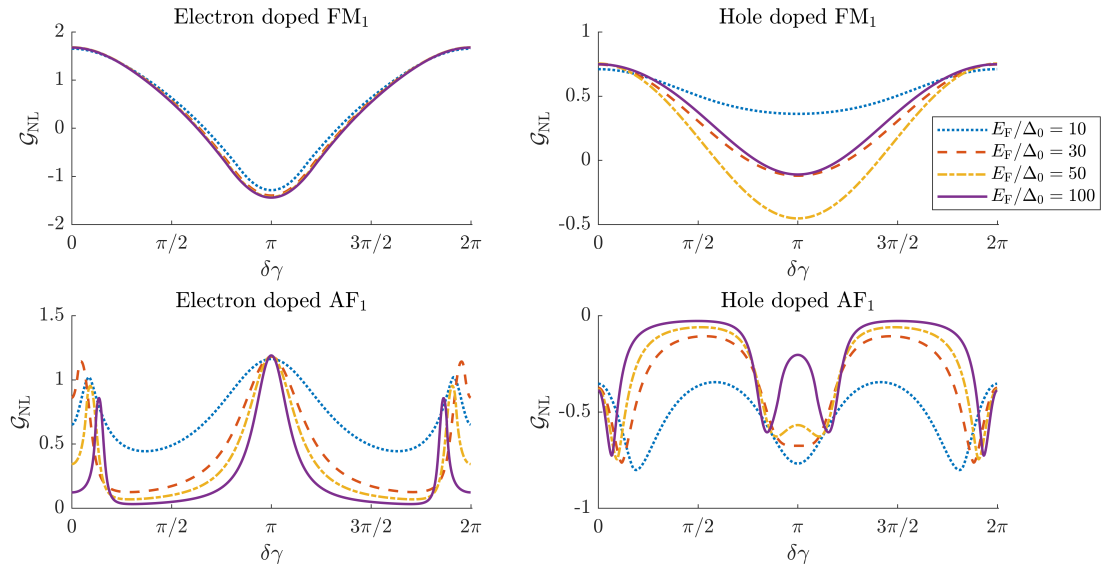

FIG. 5. Normalized nonlocal conductance $\mathcal{G}_{\text{NL}}$ as a function of the misalignment angle $\delta\gamma$ between the order parameter vectors. In all cases lead 0 is electron doped. These plots clearly show that the sign of the total nonlocal conductance is very sensitive to the order parameter direction in FM leads, while it remains unchanged in AF leads.

INTERFACE EFFECTS

In the main text, we have assumed that the interface is i) ideal and ii) magnetically compensated. We here want to investigate the effect of lifting these assumptions quantitatively. In the BdG Hamiltonian, interface effects can be modelled by a delta-function-like potential. The interface Hamiltonian, incorporating i) and ii) is

$$H_{\text{I}} = \begin{bmatrix} H_V + H_h & 0 \\ 0 & -H_V - H_h^T \end{bmatrix} \delta(x - x_0), \tag{7}$$

where x_0 is the position of the interface. We model a non–ideal interface with a spin-independent potential barrier of strength $V > 0$,

$$H_V = V s_0 \otimes \sigma_0. \tag{8}$$

To incorporate the effect of an uncompensated interface, we introduce the following spin-dependent potential

$$H_h = \frac{h}{2} \left(\mathbf{n}(x) \cdot \mathbf{s}\right) \otimes \left(\sigma_0 + \sigma_z\right), \tag{9}$$

modelling a net magnetization with strength h. The Pauli matrices s and σ denote spin and sublattice degrees of freedom.

Adding the interface potential, Eq. (7), to the BdG Hamiltonian of the main text, and integrating over the interface at x_0, we obtain the following continuity condition

$$i\hbar v_\mathrm{F}\,\tau_z \otimes s_0 \otimes \sigma_x \left[\psi(x_0^+) - \psi(x_0^-)\right] = \left[V\tau_z \otimes s_0 \otimes \sigma_0 + \frac{h}{2}\tau_4 \otimes (\mathbf{n}(x) \cdot \mathbf{s}) \otimes (\sigma_0 + \sigma_z)\right]\psi(x_0) \tag{10}$$

where we introduced the Pauli matrices for charge degrees of freedom (electron/hole) $\boldsymbol{\tau}$ and the matrix $\tau_4 = \mathrm{diag}\,(1, -T)$, where T represents the transpose operator.

To quantitatively investigate the effect of imperfect or uncompensated interfaces, we introduce the dimensionless barrier strength $Z_V = V/\hbar v_\mathrm{F}$ and the dimensionless uncompensated magnetic moment $Z_h = h/\hbar v_\mathrm{F}$ respectively. In Fig. 6, we demonstrate how the interface effects changes the non–local conductance.

An imperfect interface, modelled by spin-independent potential, does not suppress or qualitatively change the non–local conductance, only a shift in the position of the conductance peak is observed. We attribute this behaviour to the "relativistic" effects associated with Klein-like tunnelling, masking the potential barrier for hexagonal lattices. In non-relativistic Hamiltonians, like a square lattice AF system, we expect that the non–local conductance decreases with increasing the barrier strength.

The effect of an uncompensated interface that leads to a net interface magnetization can be more dramatic. For moderate net magnetizations at the interface, the amplitude of the non–local conductance is slightly reduced. For larger net magnetizations at the interface, the conductance gradually decreases and vanishes completely in the limit of very strong net magnetization. This occurs because a strong fixed-direction magnetization closes the spin-flip process channels in the system. Since finite local and non–local ARs need a spin-flip channel, both are suppressed in the strong magnetization regime. This leaves NR as the dominant scattering process and thus, both local and non–local conductances are suppressed.
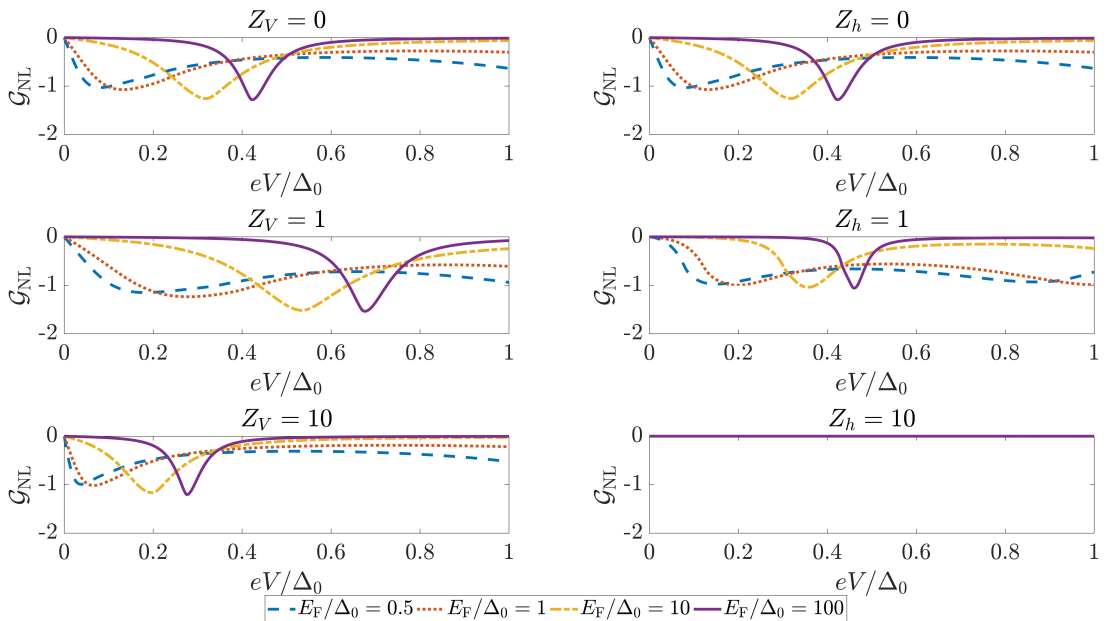

FIG. 6. Normalized nonlocal conductance $\mathcal{G}_\mathrm{NL}$ as a function of the potential barriers Z_V and Z_h parameterizing the transparency of the interface and degree of uncompensated magnetic moments respectively.

NTNU
Norwegian University of
Science and Technology